Design, Implementation and Validation of a New Neutron Spectral Code for High Temperature Gas Reactors

Auslegung, Implementierung und Validierung eines neuen Neutronen-Spektralprogramms für gasgekühlte Hochtemperaturreaktoren

Von der Fakultät für Maschinenwesen der Rheinisch-Westfälischen Technischen Hochschule Aachen zur Erlangung des akademischen Grades eines Doktors der Ingenieurwissenschaften genehmigte Dissertation

vorgelegt von

Francesco Tantillo

Berichter: Univ.-Prof. Dr. rer. nat. Hans-Josef Allelein
Univ.-Prof. Dr.-Ing. Rafael Macián-Juan
Univ.-Prof. Dr.-Ing. André Bardow

Tag der mündlichen Prüfung: 28.11.2018

Abstract

Die Forschungs- und Entwicklungsaktivitäten rund um Generation-IV-Reaktorkonzepte wie den Hochtemperaturreaktor (HTR) fordern heutzutage die Entwicklung und den Einsatz von immer anspruchsvolleren, multiphysikalischen, numerischen Simulationswerkzeugen. Das Ziel dieser Systemcodes ist es, alle sicherheitsrelevanten Aspekte eines hypothetischen Unfallszenarios in einer integrierten und möglichst exakten Weise zu simulieren.
Das HTR Code Package (HCP), das am Forschungszentrum Jülich (FZJ) und an der RWTH Aachen entwickelt wurde, soll die genannten Ziele erfüllen. Schwerpunkt dieser Arbeit ist die Ertüchtigung des HCP im Bereich der Neutronik. Im Fokus stand dabei der Entwurf, die Implementierung und Validierung eines neuen Codes zur Berechnung des Neutronenspektrums, welcher die Vorteile einer Multi-Physik-Plattform voll ausschöpft und dabei einen guten Kompromiss zwischen Genauigkeit und benötigter Rechenleistung gewährleistet sowie darüber hinaus eine hohe Benutzerfreundlichkeit aufweist.
Die Notwendigkeit eines neuen Spektrum-Codes entstand aufgrund der Tatsache, dass bestehende Codes des FZJ aufgegeben wurden, technisch veraltet sind oder eine entsprechende Dokumentation und Validierung vermissen lassen. Insbesondere waren sie nicht dazu bestimmt, in eine moderne Multi-Physik-Plattform integriert zu werden bzw. in einer objektorientierten Code-Umgebung zu arbeiten. Darüber hinaus besitzen diese Spektrums-Codes wechselseitige Abhängigkeiten mit anderen Codes. Die Auflösung dieser Abhängigkeiten wurde zu einer der Hauptaufgaben der Arbeit und führte zu einer Überprüfung neuester Methoden und Ansätze für die Generierung von Wirkungsquerschnitten im HTGR-Bereich.
Der neu entwickelte Code TRISHA (TRansport Integral Spectrum Code und Homogenization Application) enthält zwei Löser: Der eine basiert auf der Neutronendiffusionstheorie, der andere auf der Neutronentransporttheorie. Darüber hinaus ermöglicht der Code in Bezug auf die doppelte Heterogenität des Brennstoffs und der Neutronen-Resonanz-Behandlung, eine Wahl zwischen zwei verschiedenen Dancoff-Faktor-Berechnungsansätzen. Diese analytischen Methoden erweisen sich als sehr präzise und schnell im Vergleich zu traditionellen semi-empirischen, deterministischen Monte-Carlo-Ansätzen.
Umfangreiche Rechnungen wurden durchgeführt, um die Gültigkeit und die Genauigkeit von TRISHA nachzuweisen. Konkret wurde der Code parallel zu einer Validierungs- und Verifizierungskampagne mit dem Monte-Carlo-Code Serpent entwickelt. Die Zunahme der Komplexität der Benchmarks spiegelt die Hauptschritte der Entwicklung des Codes wider - von einfach beschichteten Partikeln bis hin zu ersten Kritikalitäts-Validierungs-Benchmarks für den HTR-10. Der Spektralcode wurde auch gegen verschiedene Arten von Brennstoffkonfigurationen getestet, wobei auch Thorium-basierte Brennstoffkreislauf-entwürfe berücksichtigt wurden.
Besondere Anstrengungen wurden auch in das Design und die Validierung des HCP Datenbibliothekgenerators LibGen gesteckt. Die guten Leistungen des Spektrums-Codes sind daher auch ein Spiegelbild der umfangreichen Arbeiten im Bereich des Erzeugungsprozesses von Neutronendaten. Schließlich sorgen die MGT-3D / MGT-N-Vergleiche dafür, dass die Gültigkeit der Reimplementierung und Refactoring-Arbeit des alten Diffusionscodes MGT-3D hin zu MGT-N als Teil von HCP verifiziert ist.

Abstract

The research and development activities around the generation IV High Temperature Gas Reactor (HTGR) concept currently demand the development and the usage of increasingly sophisticated multi-physics numerical simulation tools. The goal of these system codes is to simulate in an integrated and accurate manner all the safety relevant aspects of a hypothetical accident scenario.
The HTGR Code Package (HCP) project was developed as a joint effort from Forschungszentrum Jülich (FZJ) and RWTH Aachen University, and aims to achieve the abovementioned goals. The focus of this thesis is the neutronics of HCP, and in particular the design, the implementation and the validation a new neutron spectrum code able to exploit the benefits of a multi-physics platform, keeping a well-balanced trade-off between accuracy and computational burden, and being user-friendly at the same time.
The need for a new spectrum code arose from the fact that all similar codes, previously developed in FZJ, were limited by dependencies towards other codes, they were not designed to be integrated in modern multi-physics platforms or suited to work in an object-oriented environment. Remove those dependencies became one of the major tasks of the thesis, leading to a review of the latest methods and approaches for data group constants generation in the HTGR field.
The newly developed code TRISHA, TRansport Integral Spectrum code and Homogenization Application, contains two different solvers: one based on the neutron diffusion theory and the other one based on the neutron transport theory. Additionally, with respect to the fuel double heterogeneity and neutron resonance treatment, the code allows the user to choose between two different Dancoff factor calculation approaches. These analytical methods proved to be very accurate and fast compared to traditional semi-empirical deterministic and Monte Carlo approaches.
Extensive work was done to prove the validity and the accuracy on each part of the TRISHA. In order to achieve that, the code was built in parallel with a validation and verification campaign, considering the Monte Carlo code Serpent as reference code. The increase in complexity of the benchmarks mirrors the major steps of the development of the code. The development started with the simulation of simple coated particles up to the HTR-10 first criticality validation benchmark. The spectrum code was also tested against different kind of fuel designs taking also into consideration thorium-based fuel cycle designs.
Particular effort was also put into the design and the validation of the HCP library generator LibGen. The overall good performances of the spectrum code are therefore a reflection of the good level of accuracy reached in the neutron data library generation process.
Finally, the MGT-3D / MGT-N comparisons ensure that validity of the re-implementation and refactoring work done on the old diffusion code MGT-3D now part of HCP as MGT-N.

Educational Background

Personal Details	
Name	Francesco Tantillo
Date of birth	21-05-1987
Email	tantillofrancesco87@gmail.com
Nationality	Italian

Educational	**Background**
2013-2016	**PhD Research Assistant** at Forschungszentrum Juelich Duties: - Design, implementation and validation of reactor physics codes - Nuclear reactor modelling with deterministic and Monte Carlo codes - Neutron cross section data library generation - Maintenance and refactoring of legacy codes
2010-2013	**Master Degree in Nuclear and Energy Engineering**, Universita' di Palermo (IT) Master's thesis: Bidimensional extension of the neutron integral transport code TOTMOS
2006-2010	**Bachelor Degree in Energy Engineering**, Universita' di Palermo (IT) Master's thesis: Neutron activation analysis of fusion reactor structural materials

Abbreviation list

AVR	Arbeitsgemeinschaft VersuchsReaktor
BISO	BIstructural-ISOtropic (coated fuel particle)
FZJ	Forschungszentrum Jülich
GT-MHR	Gas Turbine Modular Helium Reactor
HEU	Highly Enriched Uranium
HCP	High temperature gas reactor Code Package
HTR	High Temperature Reactor
HTGR	High Temperature Gas Reactor
HTR-10	High temperature Gas cooled Test Reactor
HTR-PM	High Temperature Reactor Pebble bed Modules
HTTR	High Temperature Test Reactor
INL	Idaho National Laboratory
INET	Institute of Nuclear and New Energy Technology
JAEC	Japan Atomic Energy Commission
KFA	Kernforschungsanlage (Jülich)
KLAK	Kleine AbsorberKugeln
LEU	Low Enriched Uranium
MCNP	Monte Carlo N-Particle Code
MEDUL	MEherfachDUrchLauf
MGT-3D	MultiGroup Tinte-3D
MGT-FD	MultiGroup Tinte-Fluid dynamics
MGT-N	MultiGroup Tinte-Neutronics
OECD	Economic Co-operation and Development
OTTO	Once Through Then Out
PBMR	Pebble Bed Modular Reactor
RWTH	Rheinisch-Westfälische Technische Hochschule
SHUFLE	Software for Handling Universal Fuel Elements
STACY	Source Term Analysis Code System
STAR	Source Term due to Aerosol Re-suspension
THTR	Thorium High Temperature Reactor
TINTE	Time dependent Neutronics and Temperatures
TNT	Topological Nuclide Transmutation
TRISHA	TRansport Integral Spectrum and Homogenization Applications
TRISO	TRistructural-ISOtropic (coated fuel particle)
TTA	Transmutation Trajectory Analysis
VHTGR	Very High Temperature Reactor
VSOP	Very Superior Old Program

Variable list

A	Atomic mass number
a	Bell factor
b	Levine factor
B	Neutron buckling
C	Dancoff factor
D	Diffusion constant
E	Energy
F	Pebble packing fraction
$H()$	Chord length probability density function
$\mathbf{J}$	Neutron current
k	Multiplication factor
l	Chord length
L_i	Neutron leakage in the i-direction
N	Neutron density
$\mathbf{n}$	Normal
N_i	Nuclear density of the i-isotope
P	Neutron escape probability
r and R	Radii
N_{gr}	Number of grains
$\boldsymbol{M}$	Multiplying matrix
Q	Geometrical factor
$\mathbf{r}$	Space coordinate
s	Distance
$\boldsymbol{S}$	Fission-source matrix
S	Space
t_{ii} and T_{ii}	First flight collision probabilities
T	Temperature
t	Time
$\mathbf{v}$	Velocity
V	Volume
Γ_p	Practical width of the resonance
γ	Ratio between the void and the material volumes of the mesh
δ_{ii}	Kronecker delta
Δ	Mesh width
η	Efficiency of a reversible thermodynamic system
$\Theta()$	Computational complexity
θ	Neutron source
λ	Mean free path
ξ	Average increase in lethargy per collision
μ	Scattering angle
ν	Number of neutrons per fission
Σ_a	Macroscopic absorption neutron cross section
Σ_b	Macroscopic bound neutron cross section

Σ_s	Macroscopic scattering neutron cross section
Σ_t	Macroscopic total neutron cross section
Σ_{tr}	Macroscopic transport neutron cross section
σ_0	Microscopic background neutron cross section
σ_e	Microscopic escape neutron cross section
Σ_f	Macroscopic fission neutron cross section
σ_p	Microscopic potential neutron cross section
σ_t	Microscopic total neutron cross section
Σ^*	Pseudo neutron cross section
ϕ	Neutron angular density
χ	Fission neutron spectrum
ψ	Neutron flux
$\hat{\mathbf{\Omega}}$	Velocity direction vector
ξ	Disadvantage factor

Contents

1 Introduction

"With the United Nations predicting world population growth from 6.7 billion in 2011 to 8.7 billion by 2035, demand for energy must increase substantially to meet such expansion. Indeed, it has been seen often how both population growth and increasing standards of living for many people in developing countries cause a strong growth in energy demand." [1]
More than 70% of the increased energy demand is coming from developing countries, especially China and India. Additionally, China overtook US as top CO_2 producer in 2007. On top of this, the UN Population Division foresees an increase of urbanisation, from 52% in 2011 to 62% in 2035 and reaching 70% worldwide by 2050, allowing the world population to stabilize at about 9 billion with better food supply, clean water, health systems, education and communication facilities.
In the *World Energy Outlook 2016 New Policies Scenario*, coal demand increases 0.2% p.a. from 2014 to 2040, gas increases 1.5% p.a. and oil increases 0.5% p.a. for the same period. For electricity, coal use increases 35% by 2040 thus reducing its share of generation from 40% to 28%. Nuclear output is expected to grow almost 80% by 2040, largely due to a wave of new power stations in China while renewables other than hydro are expected to increase nearly five-fold [2].

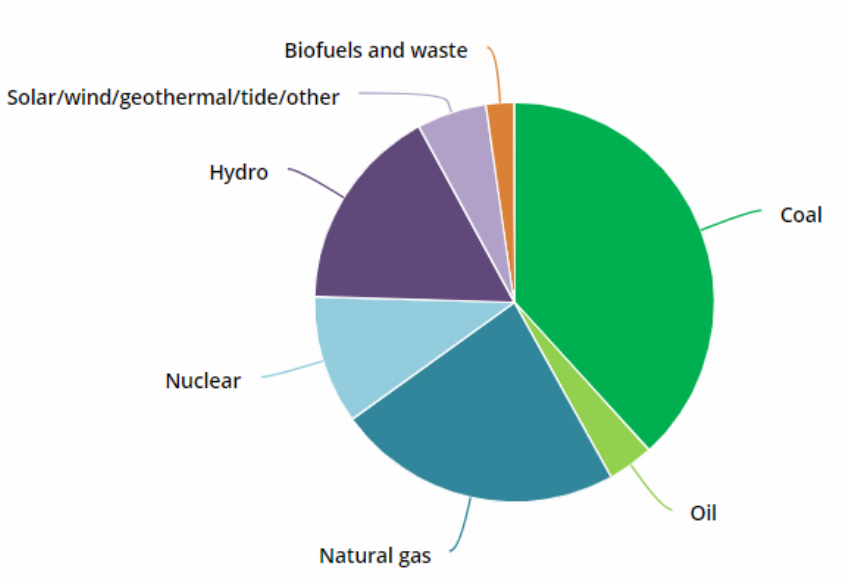

Figure 1.1: World electricity production 2016 [2]

Nuclear power generation is an established part of the world's electricity mix providing in 2016 about 10.4% of the world electricity, coal 38.3%, oil 3.7%, natural gas 23.1%, hydro 16.6% and other 8%; figure 1.1. It is especially suitable for large-scale, continuous electricity demand which requires reliability (i.e. base-load), and hence ideally matched to increasing urbanisation worldwide.

Despite the challenges it currently faces, nuclear power has specific characteristics that underpin the commitment of some countries to maintain it as a future option. Nuclear plants can contribute to the reliability of the power system where they increase the diversity of power generation technologies in the system. For countries that import energy, it can reduce their dependence on foreign supplies and limit their exposure to fuel price movements in international markets [1].
Moreover, the great danger coming from the continuous increase of the greenhouse gas emissions seems now universally recognized, and numerous strategies and scenarios are being proposed in order to attain more sustainable future energy supplies. In most of the scenarios, the prospects for growth of nuclear energy seems favorable. For instance, the *World Energy Outlook 2016 450 scenario* forecasts an additional 820 GW of nuclear capacity by 2040 in a scenario that would stabilize the atmosphere at 450 *ppm* CO_2 and therefore limit global warming effects to 2 $°C$ above pre-industrial levels [2]. Of course, if other clean energy technologies cannot be deployed in sufficient amounts, nuclear energy must be ready to scale up to complement them well in the future [4].

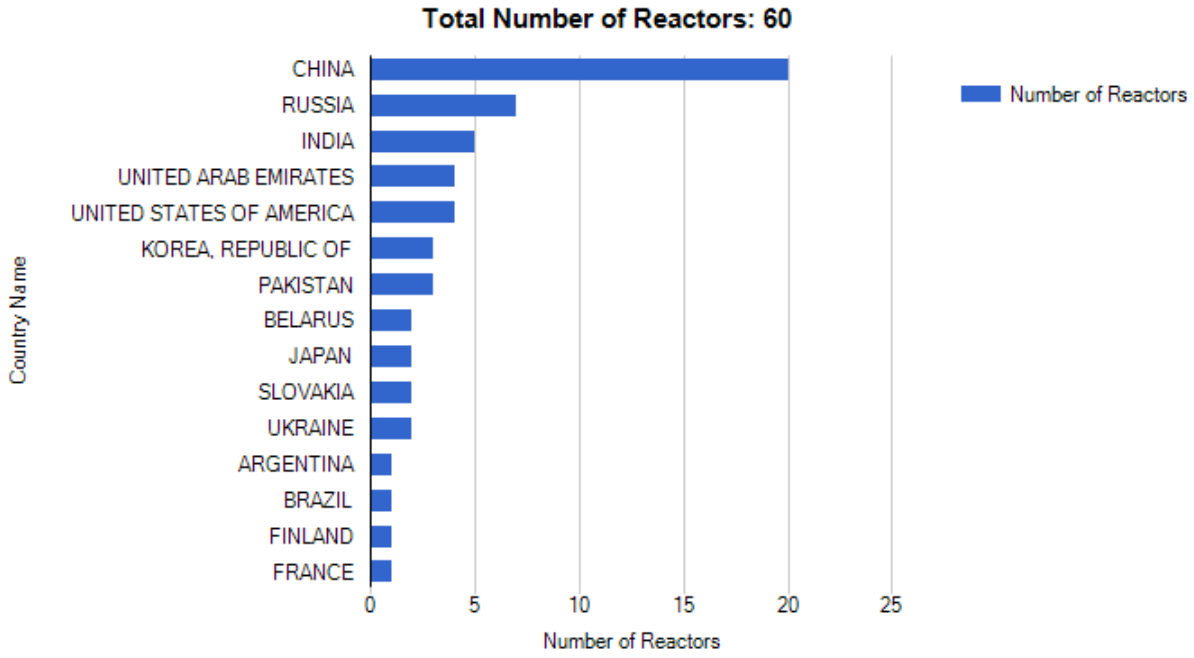

Figure 1.2: Nuclear reactor under construction 2016 [5]

Many countries in the world, both industrialized and developing, are leading the growth of nuclear energy. 60 new units are under construction in 15 countries, and more are preparing to move forward, figure 1.2. They are confident that nuclear energy is a favorable option in order to guarantee their energy security in the future. However, challenges still exist to further large-scale use of nuclear energy [4]:

1. Nuclear energy must be sustainable from the standpoint of its utilization of nuclear fuel resources as well as the management and disposal of nuclear waste
2. The units must operate reliably
3. Safety must remain of paramount importance
4. The units must be economically competitive
5. Deployment must be undertaken in a manner that will reduce the risk nuclear weapons proliferation
6. New technologies should help to meet anticipated future needs for a broader range of energy products beyond electricity
7. Governments need to support the revitalization of their nuclear R&D infrastructures

While the first four are the major goals of Generation IV; the latter two have become increasingly important in recent years.
The very high temperature reactor (VHTR), or high temperature gas-cooled reactor (HTGR), is a Generation IV reactor concept that uses graphite as a moderator with a once-through uranium fuel cycle. The reactor core can be either a "prismatic block" or a "pebble-bed" core [6].
Among the most important features of HTGRs there are enhanced safety, high thermal efficiency, economic competitiveness, and proliferation resistance. These very favorable characteristics make this technology a potential candidate for the advanced nuclear power plant deployment. Furthermore, net thermal efficiencies greater than 45 % seems to be possible in most of the newest designs of HTGRs.
One of the strongest argument in favor of this technology lies in its utilization as a source of process heat. The high outlet gas temperatures make possible to utilize these reactors as thermal heat sources in endothermic chemical processes. Possible applications are in coal chemistry and upgrading of hydrocarbons. Hydrogen production is another very promising field for deployment of the HTGRs. The short construction period, modularity and low capital cost are also attractive characteristics of HTGRs.
Above all, the foremost motivation for the development of HTGR technology is its enhanced safety features along with its high temperature capabilities. The enhanced safety of the HTGR fuel is based on its coated particle fuel design consisting of uranium oxide particles coated with layers of pyrolytic carbon and silicon carbide. Coated particles are designed in order to withstand high internal gas pressure limiting the release of fission products to the environment to a very low level [7].

1.1 General description of the HTGR

1.1.1 Basic concepts

The thermodynamic and temperature limitations of conventional light water reactors always result in low thermal efficiency, use of special low-density turbines and consequently cause low fuel efficiency and thermal pollution of the environment. Furthermore, the low outlet temperature shrinks the possibilities of using nuclear power as an industrial source of heat.
High temperature gas reactors have been investigated and developed in order to overcome these limitations using a core composed exclusively of ceramic materials and employing an inert coolant. This limits the choice of the neutron moderator to graphite or beryllium. Beryllium is an excellent moderator, although its use is limited by technical and economic difficulties, therefore, graphite seems to be the only viable moderator for HTGRs [8].
The physical properties of carbon are of interest for nuclear reactors: its atomic mass and very low neutron capture cross section makes it a fairly good candidate for moderation. In addition, its very high temperature behavior (sublimation temperature about 2500 K and melting around 4700 K) allows the use of graphite for high temperature applications. Therefore, graphite has been used in many thermal neutron reactors as moderators or structural components [9].
The use of a gas coolant to transport heat from the reactor core to the boilers enables the choice of the operating temperature of the reactor independently from its pressure. Therefore, the reach of good steaming conditions in the boilers is only limited by the core and circuit material performances. The optimum pressure can be evaluated based on safety and economic considerations, taking into account the blower power and the pressure circuit costs [9].

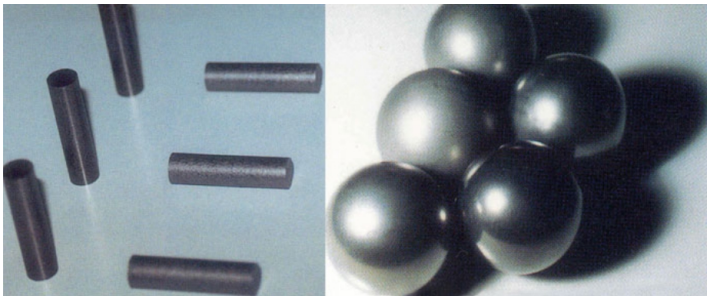

Figure 1.3: The two families of fuel elements, compacts and pebbles [9]

The coolant must be chemically inert, not undergo any phase change, not able to be activated by neutrons and have good heat-exchange properties. Helium, so far, is the only coolant able to meet the aforementioned conditions and that is naturally available in sufficient quantity. Based on the previous and newer design experiences,

the coolant outlet temperature of the HTGRs lies between 750 and 950 $°C$, with an inlet temperature of about 250 $°C$. This lower limit is imposed by the Wigner effect [10]. Since the high temperature excludes the use of metallic fuel coatings, the fission product retention has to take place at microscopical level making use of ceramic coated fuel particles.
In order to limit corrosion due to impurities present in the coolant and to further enhance the fission product retention, the part of the fuel element which contains the coated particles are separated from the coolant by means of an additional graphite layer. This basic concept allows different types of fuel geometries. In the first experimental reactors the fuel element had the form of hexagonal prismatic or cylindrical rods, with the coolant passing between these rods [8].
The fuel element design has departed from these early configurations to more robust and efficient fuel geometry arrangements. The fuel consists of large hexagonal blocks containing regular patterns of coolant and fuel holes. Two different fuel coolant arrangements rose in the 1970s. In the first case, called pin-block design, the fuel pins consist of a carbon matrix containing the coated particles, isolated from the coolant by a layer of unfueled carbon. In the second case, known as General Atomic design, the heat from the fuel rod has to flow across the bulk moderator before reaching the coolant hole. Both designs are shown in fig 1.4.

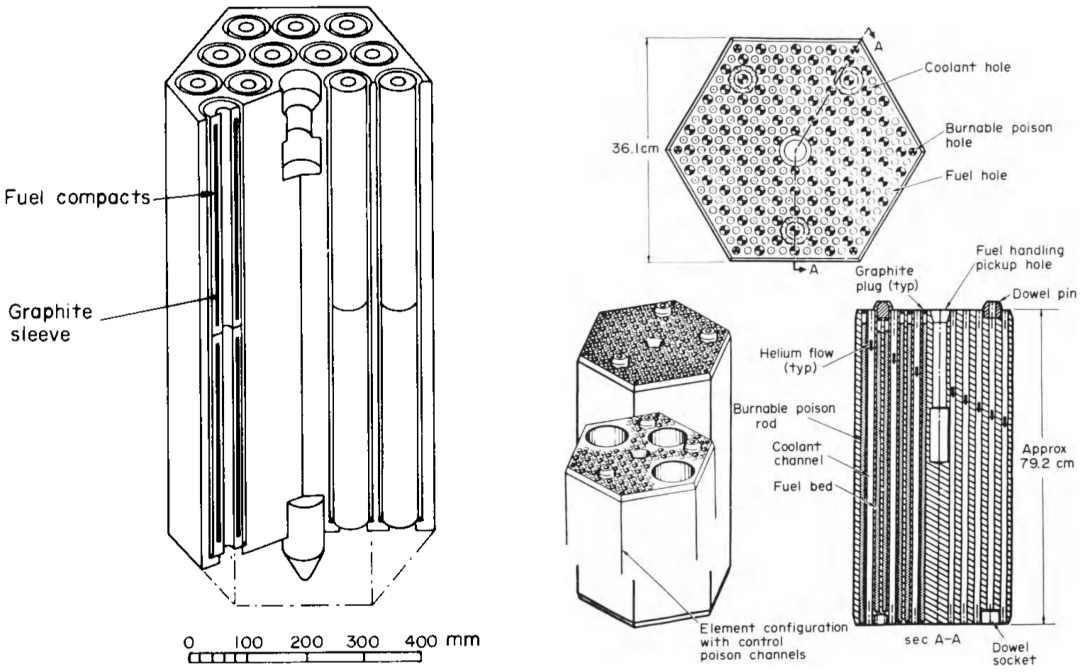

(a) *block-pin design.* (b) *General Atomic design.*

Figure 1.4: HTGR block type fuel arrangements [8]

In parallel to the HTGR with block type fuel, a version with spherical fuel elements

has been developed and investigated in Germany, the so called pebble bed reactor. The fuel elements have the form of graphite spheres and they are contained in a reflector of graphite blocks. One of the main advantages is the possibility to have online refueling. Replacement of a burnt pebble by a feed pebble is done when the burnt pebble reaches a desired level of burnup.
The pebbles are continuously extracted from the bottom of the core, and tested for physical integrity and burnup. They are continuously loaded pneumatically by means of tubes from the reactor top cavity and extracted from one or more tubes located in the bottom reflector [9].

1.1.2 Fuels for HTGRs

The original idea of coated fuel particles was suggested by R. Huddle in 1957 [7]. Since then, different kind of coated particles have been developed, manufactured and utilized worldwide. One of the main advantages of the HTGR is the great deal of flexibility allowed in using different fuel cycles. Therefore, High Enriched Uranium (HEU) and Low Enriched Uranium (LEU), Uranium-Thorium (U, Th), Uranium-Plutonium (U-Pu), and Plutonium (Pu) fuel cycles have been tested and employed in various HTGR reactors. Two types of coated particle fuel designs were used extensively, that is, bi-isotropic (BISO) and tri-isotropic (TRISO) particles, figure 1.5. Starting from the 1980s, only the TRISO coated particle has been allowed to be used due to new fuel quality and performance criteria [7].

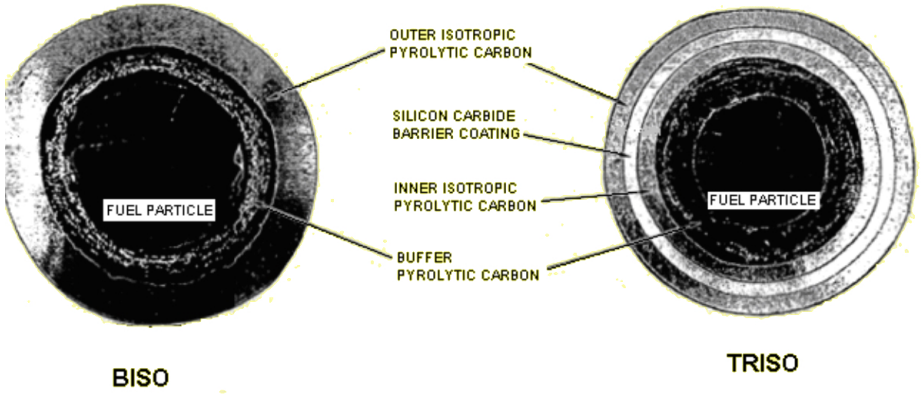

Figure 1.5: BISO and TRISO coated fuel particles [7]

Coated fuel particles are tiny fuel elements of less than one millimeter in diameter. The fundamental reason behind the research and development of this technology is preserving the integrity of the coated particles and their fission product retention capability. The oldest design, the BISO-coated particle, consisted of two layers of pyrocarbon surrounding a spherical fuel kernel. The first layer was a porous buffer layer and it was surrounded by a dense pyrocarbon layer, known pyrolytic

carbon or PyC. In the TRISO-coated particle design there are four layers consisting of the following sequence: a porous buffer layer, an inner PyC layer, a SiC layer, and another outer PyC layer. Both BISO- and TRISO-coated particles show good gaseous fission product retention capabilities.

However, the BISO particles usage is limited to low temperature and low burnup operations. The TRISO-coated particle shows to be superior in retaining metallic fission products at HTGR operational, transient, and design accident temperatures. Therefore, the TRISO-coated particle has become the only choice for reduced fission product release when extended burnups and higher fuel temperatures are required.

Every coating layer of TRISO fuel is designed for particular function related to fission product retention, creep strength, shrinkage under irradiation, and irradiation performance. Although almost all fission products are produced and retained inside the fuel kernel itself, the porous buffer layer is needed as a sacrificial layer to stop energetic fission products. This is done in order to protect the inner PyC from radiation damage and provides sufficient void volume to accommodate fission gases and kernel swelling. The inner PyC layer is a barrier against the diffusion of gaseous fission product and the chlorine gas generated during the SiC deposition process and helps to keep the SiC layer under compression. The main goals of the SiC layer is to retain metallic fission products and provide strength. The outer PyC serves as last gaseous fission product barrier limiting the tensile stress on SiC layer. Furthermore, it forms a bonding surface for the graphite matrix material.

The TRISO particle should be able to preserve its containment functions up to approximately 1800 $^{\circ}C$. However, transient and accident temperatures in HTGR designs are typically limited to 1600 $^{\circ}C$ for safety reasons. It should be also noted that a very small fraction of uranium may get trapped inside the coating layers during coating processes. This eventually may lead to fission product releases in the primary circuit. Furthermore, a very small amount of uranium might be present in the graphite matrix material as an impurity.

The Very High Temperature Reactor (VHTR) or the Next Generation Nuclear Plant (NGNP) concept has been introduced as an enhanced HTGR for the future nuclear power plant deployment. Such VHTR concepts should be able to operate at increased temperatures in order to produce outlet temperatures of 950 $^{\circ}C$ for hydrogen production, process heat applications, and Brayton cycle electricity production, while increasing fuel discharge burnup for better uranium utilization.

A viable method to achieve higher operating temperature conditions and an increased burnup is to replace the usual UO_2 fuel kernel with a stoichiometric two-phase mixture of UO_2 and UC_2, namely UCO. The UCO fuel kernel should provide resistance against fuel kernel migration and internal pressure build-up caused by excessive CO formation.

Another TRISO particle design, known as UO_2*, consists of a dense pyrocarbon seal coat and thin ZrC coating applied directly onto a UO_2 kernel followed by the conventional TRISO coatings. This thin ZrC layer should act as an oxygen getter to limit CO production and limits the kernel migration.

The last possible TRISO-coating design improvement, to be employed for mixed oxide Pu and minor actinide fuels, is to replace the SiC layer with a ZrC layer in order to minimize Pd attack in SiC. Furthermore, the ZrC layer has higher refractory material properties so that fuel temperature limits may be increased by 200 $°C$. Although it clearly sounds promising, this last design improvement still requires a great deal of development followed by extensive irradiation campaign [7].

1.2 HTGR applications

1.2.1 Electricity production

Years after start-up of the first gas cooled nuclear reactor, Calder Hall in 1956, nuclear energy has gained an important place in the world's electricity generation [7]. Since then, extensive research has led to safer and more efficient systems. This pursuit of increased system performance brought up the idea to increase the reactor operating temperature.

From the Carnot principle, the efficiency of a reversible thermodynamic system increases with temperature as follows:

$$\eta = 1 - \frac{T_1}{T_2} \tag{1.1}$$

where T_2 and T_1 are the absolute temperatures of the hot and cold source, respectively. As it can be easily seen, even an increase of the core outlet temperature of about hundred degrees, in the thermal power plant range, yields an improvement on the efficiency of the system by several points.

Furthermore, increasing the efficiency without modifying the fuel quantity used, leads to a proportional decrease in the quantity of radioactive waste created per kilowatt-hour produced [9].

However, the thermo-mechanical constraints associated with the performance of the reactor vessel steel limit the achievable outlet temperature increase. An increase in core outlet temperature is generally accompanied by an increase in helium return temperature near the reactor vessel. At this point, it is worth considering that the best reactor vessel material currently being developed (chrome steel) does not withstand temperatures above 490 $°C$ [7].

1.2.2 Space exploration

Almost parallel to the conventional program of chemical rockets development, the US labs developed and tested a very ambitious program of nuclear propulsion rockets. The goal was to heat up liquid hydrogen, above 2000 $°C$, for several tens of minutes, making use of the heat generated by a nuclear reactor. At that time, the most powerful conventional rocket was the Vulcain motor powering the Ariane V rocket. It was qualified to operate no more than 10 min.
From the aforementioned task, it is clear that only a ceramic coated particle-based HTGR fuel could be able to attain such performances. Surprisingly and against all the odds the project was an incredible success. From 1959 to 1972, all records were consistently broken. The project was then completely abandoned, as NASA never launched the APOLLO XVIII to XX though completely built: three years after the first Moon landing, space was no longer a US national priority [9].

1.2.3 Hydrogen production

As previously mentioned, the high gas outlet temperatures reached in HTGRs allow the possibility of producing hydrogen directly via thermochemical cycles, without transforming heat into electricity, with the subsequent loss in efficiency. Hydrogen is a good substitute for hydrocarbon fuels because its combustion in air results in only water. The deployment of HTGRs as a source of process heat might become more interesting if it is used as feedstock for synthetic liquid fuels, associated with coal or biomass. Dissociating a water molecule might seem as an attractive solution, as the water cycle constitutes a closed and clean cycle, but it has proved to be energetically costly. Indeed, most of the industrial production of hydrogen is achieved only making light hydrocarbons react with high-temperature steam. As an example, methane reformation with steam consists of the following reaction:

$$CH_4 + 2H_2O \rightarrow CO_2 + 4H_2 \tag{1.2}$$

The reformation is obtained at over 700 $°C$, burning the methane itself to produce the heat required. This chemical process consumes hydrocarbons and produces carbon dioxide contributing to the greenhouse effect.
In the past, several methods were considered in order to chemically dissociate a water molecule. They all involve intermediate steps with additional products that are recycled in the process, therefore acting as chemical catalysts. However, the most used processes operate at very high temperatures, typically above 900 $°C$, hence the interest of a heat source exceeding 950 $°C$. For example, sulphur-based cycles use a sulfuric acid dissociation reaction that can work only above 870 $°C$ and whose

efficiency increases with temperature. The possibility of using nuclear heat as an energy source and water as a resource could allow, in turn, the attainment of an efficient industrial production without the emission of greenhouse gases.

An alternative method consists of decomposing the water molecule by steam electrolysis. In this case, the water is vaporized and superheated, leading to a decrease of the electrical energy required for its dissociation. Of course, the direct use of heat limits the losses associated with the transformation of heat into electricity [9].

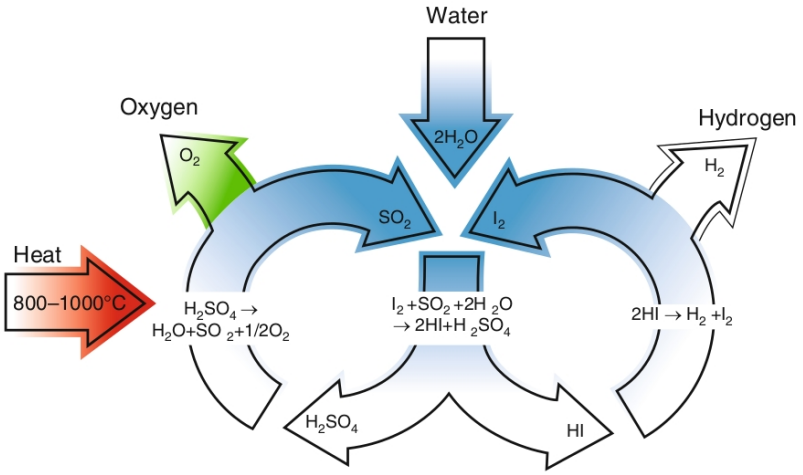

Figure 1.6: Hydrogen production by iodine-sulfur thermochemical cycle [9]

1.2.4 Water desalination

Low cost saltwater desalination is another promising application for HTGRs. The production of freshwater represents a great issue for numerous countries nowadays and in the near future. Of course, seawater desalination technologies are already available and used around the world, but their cost is often very high.

Water desalination processes usually require a mechanical or thermal source of energy, depending on the method used. For instance, saltwater can be vaporized and successively condensed obtaining fresh water that no longer contains salt. This process becomes efficient at temperatures above 120 $°C$. HTR thermodynamic cycle optimization processes could produce waste heat at temperatures of 120-130 $°C$. In this case, it is perfectly possible to install a desalination circuit considering that only the cost of the desalination circuit needs to be accounted for. This waste heat is normally unused, hence it could help to reduce desalination costs. Furthermore, the desalination process can be made even more efficient increasing the outlet reactor temperature. This usually leads to an increase of the waste heat temperature [9].

1.3 History of HTGRs

The fundamental concept of high temperature gas cooled reactors featuring a prismatic core construction was firstly investigated at the Atomic Energy Research Establishment, Harwell, early in 1966. Simultaneously, work started in Western Germany on the so called pebble bed design in which the core is filled with a randomly packed bed of spherical fuel elements. The Harwell work led eventually to the construction of the 20 MW reactor experiment of the OECD High Temperature Reactor Project (DRAGON) at Winfrith, England. The reactor attained its nominal power in April 1966. The Harwell design concept was then further improved with the Peach Bottom Reactor of the Philadelphia Company, developed and designed General Atomic of San Diego, achieving full power in May 1967.
These two prototypical high temperature gas reactors were soon followed by a third one when in February 1968 the pebble-bed AVR reactor, built by Brown Boveri/Krupp Reaktorbau GmbH, for Arbeitsgemeinschaft Versuchsreaktor (AVR) utiliy group, came into operation at the KernForschungsAnlage (KFA), now Forschungszentrum Juelich. One of the main innovations of AVR was its spherical fuel element, a 6 cm diameter graphite "pebble" inside which coated particles are agglomerated. A Hundred thousand pebbles are piled up inside a funnel-shaped graphite cavity while the control rods move in bore holes within the graphite reflector [8].

Characteristics	Dragon	Peach bottom	AVR
Criticality/shutdown	1964/1975	1966/1974	1966/1988
Thermal power (MWt)	20	115	46
Net electrical power (MWe)	–	40	15
Helium pressure (absolute bars)	20	24	11
Core inlet temperature (°C)	350	340	260
Core outlet temperature (°C)	750	715	950
Core diameter (m)	1,1	2,8	3
Core height (m)	1,6	2,3	3
Power density (MW/m^3)	14	8,3	2,2
Fuel element	Prismatic	Prismatic	Pebble
Fuel cycle	Various	$^{235}U/Th$	$^{235}U/Th$

Figure 1.7: Characteristics of some HTGRs [9]

In 1968, following the start-up of Peach Bottom, General Atomic started the construction on the Fort St. Vrain site of a 300 MWe HTGR prototype. The designated operator was the Public Service of Colorado, a small utility without previous nuclear experience. The general design of the reactor was strongly inspired by the 500 MWe

French St. Laurent Natural Uranium Graphite Gas reactor (NUGG) but with a six times smaller reactor cavity.

The core consisted of 1483 prismatic fuel elements stacked in six layers. Each fuel element was a hexagonal graphite prism in which the bored cylindrical blind channels are filled with fuel compacts. These fuel channels are then surrounded by coolant channels, in which the helium flows in downward direction. Criticality was attained in 1974 and Fort St. Vrain was connected to the grid in 1976, to be decommissioned in 1989 with a cumulative load factor of 30%. The fuel behaved successfully, but the reactor's overall design was rather a failure. Being one of the first commercial HTGR designs, the plant was a proof-of-concept where several new features were tested. This led to a number of early adopter problems that required expensive corrections.

In 1970, the German industry embarked in a 300 MWe prototype project developed from AVR, later known as THTR. The construction of THTR lasted 14 years, but the plant was operated only for four years before definitive shutdown. A number of technical difficulties, mostly due to the increase in size were met. The reactor was a thorium high temperature gas reactor rated at 300 MW electric (THTR-300). Operations started on the plant in Hamm-Uentrop, Germany in 1983, and it was shut down September 1, 1989.

The THTR was synchronized to the grid for the first time in 1985 and started full power operation in February 1987. Whereas the AVR was an experimental pebble bed high-temperature reactor (HTR) used to develop the pebble fuel, the THTR-300 served as a prototype HTR to research and test the TRISO thorium pebble fuel design [9].

In June 1987, the Japanese Atomic Energy Commission (JAEC) issued a revised "Long Term Program for Development and Utilization of Nuclear Energy" stressing that Japan should pursue the development of more advanced reactor technologies in parallel with the upgrading of existing nuclear reactors. It was highlighted that the HTGR was not to be incorporated into the present existing power plant system, but the benefits that could be derived, such as its inherent safety and production of high temperature heat, are remarkable and should be pursued [11].

The High Temperature engineering Test Reactor (HTTR) is a graphite-moderated and helium gas cooled reactor with an outlet temperature of 950 $^{\circ}C$ and a thermal output of 30 MW. The major objectives of the HTTR are to establish and upgrade the technological basis for advanced high temperature gas cooled reactors and to conduct various irradiation tests for innovative high temperature basic research.

The construction began in March 1991 and was completed on May 1996. The fuel loading was started on July 1, 1998 from core periphery. The first criticality was attained in annular type core of 19 columns on November 10, 1998. The first full power operation with an average core outlet temperature of 850 $^{\circ}C$ was completed on December, 7

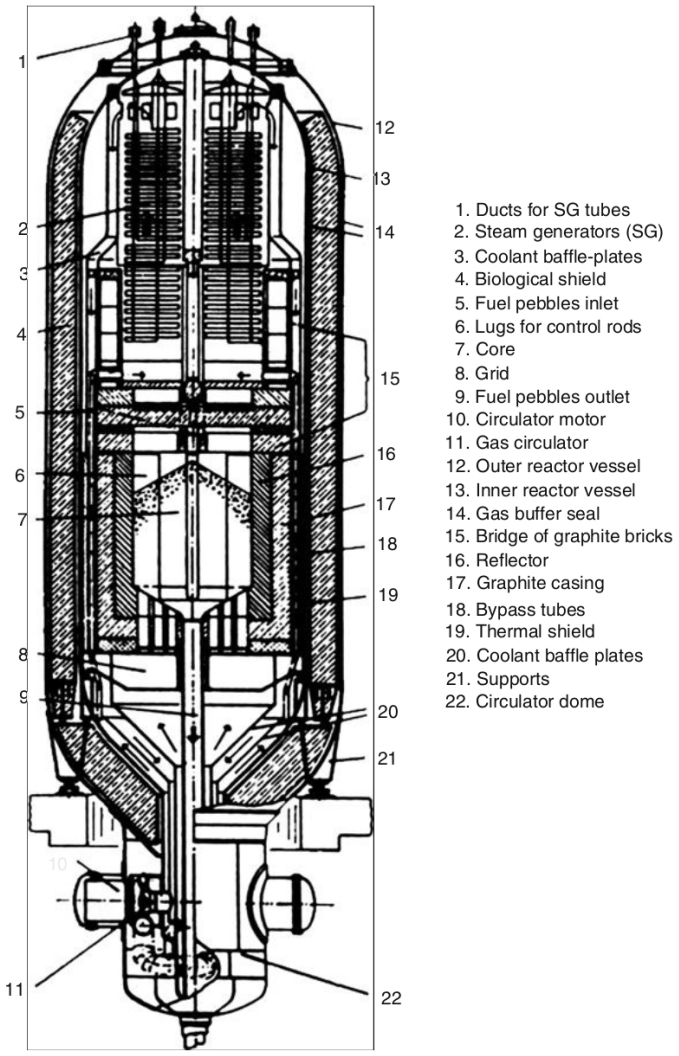

Figure 1.8: The Juelich AVR reactor [9]

2001, and operational licensing of the HTTR was approved on March 6, 2002 [12]. At the beginning of the year 2006, China released the guidelines on a national medium- and long-term program for science and technology development (2006-2020), announcing that it planned to accelerate the research on 16 key technologies including the HTGR reactors. After an initial fundamental study, the 10 MW High temperature Gas cooled Test Reactor (HTR-10) project was initiated in 1992.
The HTR-10 is a graphite-moderated helium gas cooled reactor. The completion of basic design and safety review was followed by construction of HTR-10 that started in 1995. It reached its first criticality in December 2000 and was operated at full power condition in January 2003. So far more than 100 commissioning tests have been completed and six safety demonstration experiments have been carried out.
In the design of HTR-10, the advanced concepts of newly investigated modular high temperature reactors are assimilated. Its design features a compact side-by-side

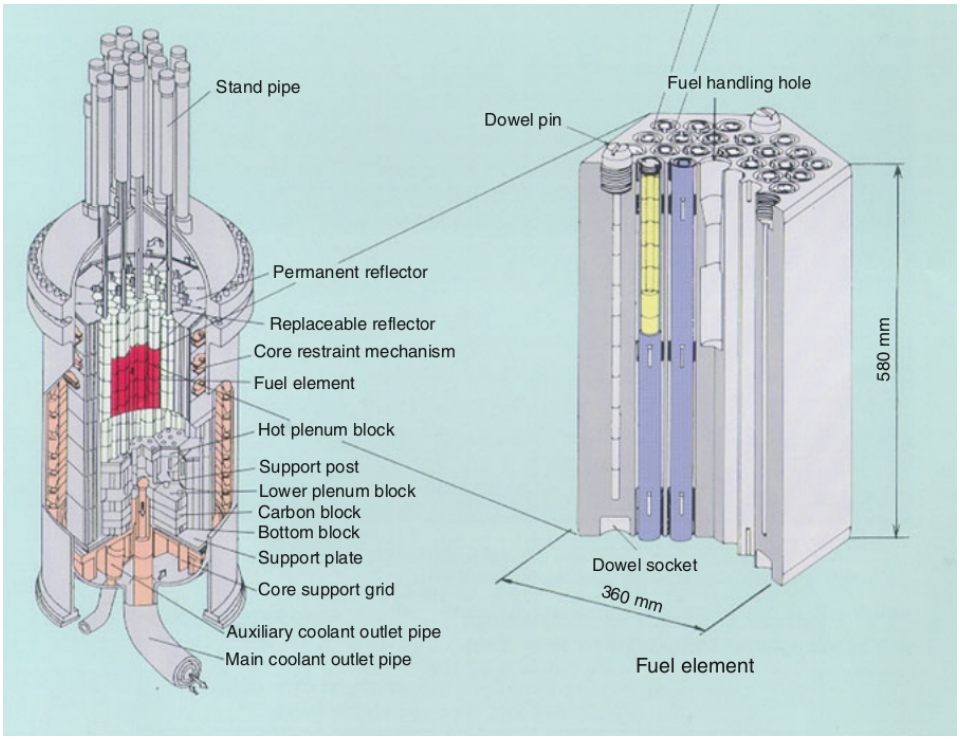

Figure 1.9: HTTR core and fuel element [9]

arrangement of the reactor core and the steam generator, spherical fuel elements with TRISO coated particles and continuous fuel refueling. A completely passive decay heat removal system and a surface cooling system are designed and implemented in HTR-10. Two reactor shutdown systems, the control rod system and the small absorber ball system, which enable the automatic shutdown of the reactor under every postulated emergency scenario, are located in the reactor side reflector.

Based on the success of the HTR-10, long-time operation test and safety demonstration tests have been carried out. The long-time operation tests verified that the operation procedures and control methods were appropriate for the HTR-10 and the safety demonstration test showed that the HTR-10 possesses inherent robust safety features.

Following these accomplishments, two new projects have been recently launched to further develop the HTGR technology in China. The first one is a prototype modular plant, denoted as HTR-PM, designated to demonstrate the commercial capability of the HTGR power plant. HTR-PM is designed as 2 x 250 MWt, pebble bed core with a conventional steam turbine generator that serves as energy conversion system. The second is a gas turbine generator system coupled with the HTR-10, denoted as HTR-10GT, built in order to demonstrate the feasibility of the HTGR gas turbine technology [13].

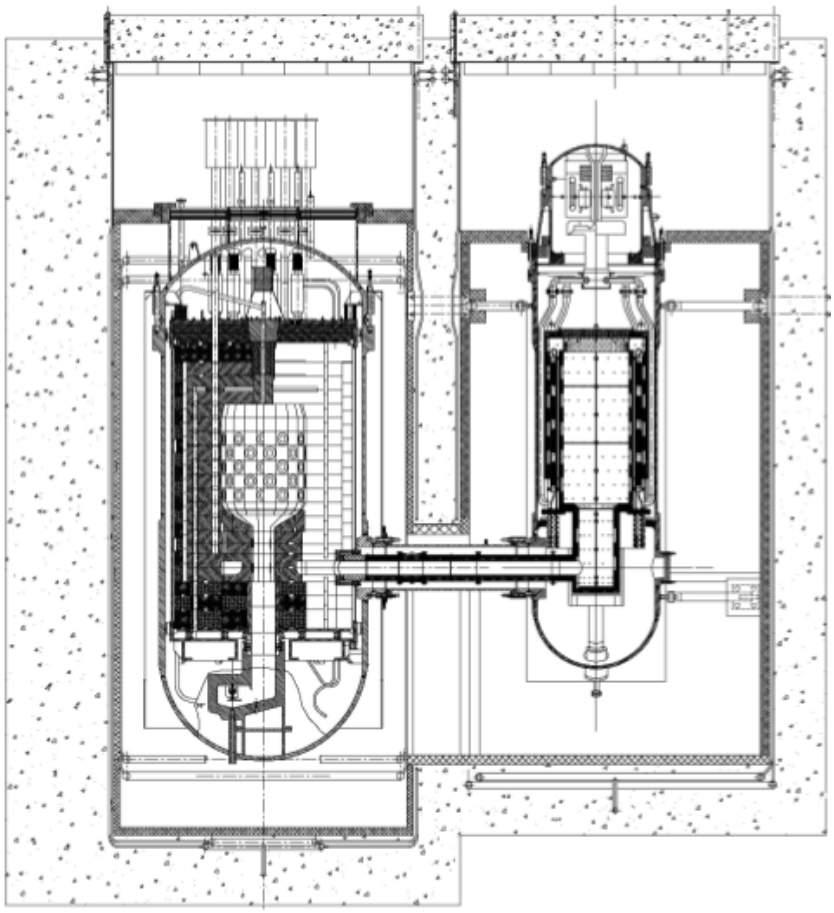

Figure 1.10: Layout of HTR-10 Primary System [13]

1.4 History of HTGR codes

The main goal for the design of a nuclear reactor system is the determination of a set of parameters which ensure the safety, the reliability and the economics of the reactor operations during the desired core lifetime. The principal tools to be used in this task, consist of a set of physics models and theories able to reproduce, up to a certain level of accuracy, the dynamic behavior of the primary circuit of a HTGR. These methods are usually implemented by a multiplicity of codes used to simulate and predict the overall response of the nuclear system. The codes can be coupled together in what is called a system code.

The basic structure of system code consists of several modules which exchange data according to the specific calculation route. The simulation usually starts with a module in charge of generating macroscopic group constants (spectrum code) followed by a module that makes use of the previously evaluated group constants in order to calculate the core multiplication factor, the neutron and the power distributions (diffusion code). The power distribution can then be used by the fluid dynamic module, which solves the heat transfer and the fluid flow to determine the temperature

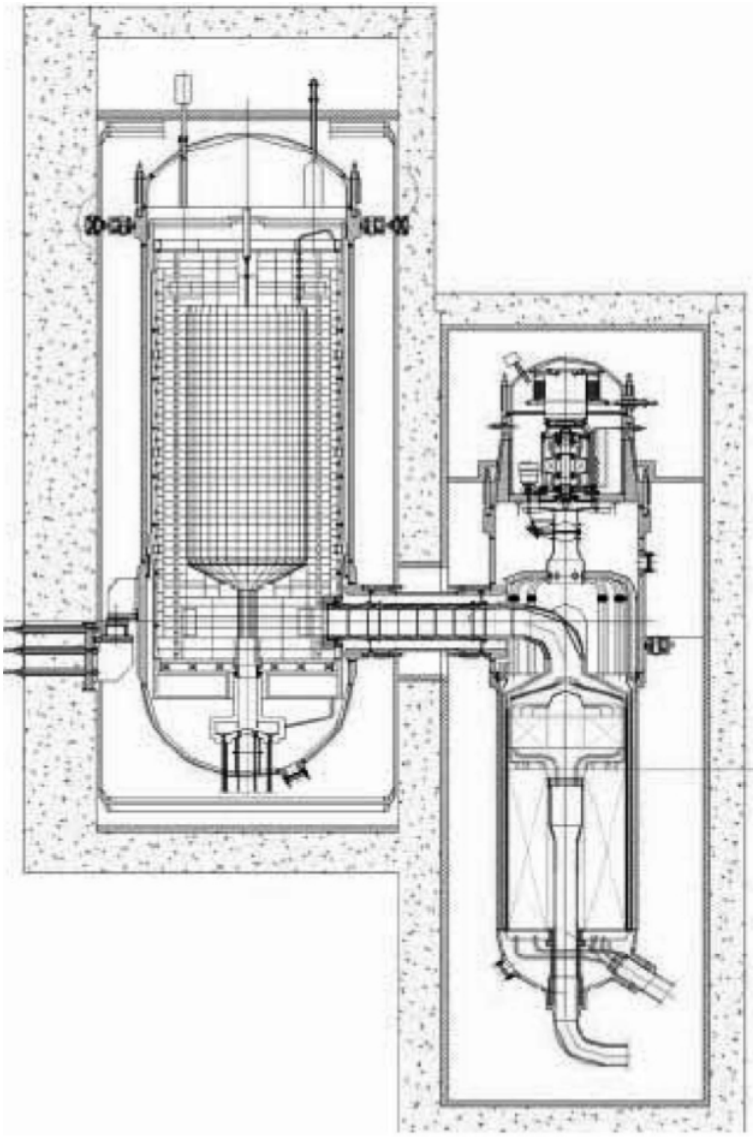

Figure 1.11: Primary System of the HTR-PM [13]

distribution within the core. It is also worth noting that temperatures have a strong influence on the neutron cross sections, so that an iterative process is needed between the two modules.

Additionally, pebble bed HTGRs are characterized by continuous shuffling of fuel elements. Typically, there are two principal shuffling schemes. A Once Through Then Out (OTTO) scheme where the pebbles are loaded from the top of the pebble bed and then discharged from the bottom, and a MEhrfachDUrchLauf (MEDUL) scheme, multi-pass in German, where the pebbles are actually recycled several times. The movement of the pebbles can be modelled as a laminar flow and it requires a specific code module in order to simulate it with the appropriate accuracy.

Another feedback is due to the movement of the control rods, needed in order to

balance the xenon effects, to maintain the reactor critical and to shutdown safely the reactor during abnormal or accident scenarios. Finally, the depletion module starting from the neutron flux distribution, calculates the fuel isotope depletion, the fertile isotope transmutation and the reactor poisoning due to the build-up of the fission products. Also the latter triggers an iterative process inasmuch the neutron cross sections are now affected by the new material concentrations.
The general approach, for the reactor physics calculation, is to model the reactor core as a multiplicity of different unit cells, one for each spectrum code mesh. Then a detailed analysis is performed, usually applying neutron transport theories, in order to account for the strong spatial flux distribution within the cell to obtain cell-averaged or so called self-shielded group constants to be used in the subsequent diffusion analysis of the entire reactor system [14].

1.4.1 Early developments

In the early days (1950s), the method for analysing a reactor core consisted of a series of simplified calculations performed using separate pieces of code that formed a calculational chain. Each piece of code in the chain served a specific purpose and results from one piece of software were used to feed the next piece of software in the calculation scheme.
The process began by calculating a spatially independent fast flux spectrum above 0.625 eV, such as the one generated on a grid of 54 energy groups using the MUFT code [15]. The companion thermal flux spectrum below 0.625 eV was generated on a grid of 172 energy groups using the SOFOCATE code [16]. The 0.625 eV energy was used as the thermal cut-off, above which up-scattering effects were neglected. Both MUFT and SOFOCATE were dimensionless codes, where all the isotopes were volume-weighted regardless of the spatial effects; that simply supplied a general flux spectrum for a given material.
The spectrum obtained from the MUFT-SOFOCATE analysis was used to collapse cross sections to a very small number of groups, usually four. Using the four-group energy structure, a one-dimensional cylindrical unit cell calculation was performed using the THERMOS code [17]. The unit cell calculation provided representative flux spectrums for the fuel, coatings, and coolant regions of the reactor. The flux in the fuel region from the THERMOS unit cell calculation was passed to a burnup code, such as LEOPARD, which performed the depletion analysis on selected isotopes [18]. The whole process was very crude by today's standards and offered little in terms of accuracy.
The development of lattice physics codes for reactor analysis began in the mid-1960s with the introduction of WIMS (Winfrith Improved Multigroup Scheme) at Winfrith in the UK [19]. The concept gathered all the processes for generating few-group

cross section data into a modular collection of software that automated many of the tasks in a systematic fashion, thereby relieving the engineer of a great deal of tedious data transfer and manipulation.
The original WIMS code provided a framework for research in reactor analysis and could be applied to a very wide range of problems, such as gas-cooled reactors of the Magnox and AGR types that are prevalent in the UK. These first versions of WIMS made use of gross approximations at all stages of the calculational scheme in order to reduce execution time and memory requirements to a manageable level [9].

1.4.2 VSOP

The Very Superior Old Programs (VSOP) is a system code, developed at Forschungszentrum Juelich, designed for reactor physics and fuel cycle simulations [20]. The code is based on the MAFIA-II code assembled by L. Massimo [21]. As its predecessor, it is subdivided in seven different chain links and the sequence of their loading is chosen by the code itself. Although VSOP maintains the same structure, all its subroutines have been either rewritten or replaced.
The code is suited for all types of thermal reactors. However, it has been heavily improved and extended in order to cope with pebble bed HTGR simulations. In figure 1.12 is possible to see which codes are employed for a particular task.
Following such scheme, the calculation starts from the DATA-2 and DATA-3 modules, specifically designed for HTGRs [22]. They allow to prepare the input data for the nuclear part of the code, from the basic geometry design features for the fuel elements and the reactor core, respectively.
The calculation then continues with the spectrum code module that makes use of THERMOS and GAM [23]. The thermal cell code THERMOS has been extended to treat grain structures and employs a 30-group energy structure derived from the GATHER library [24]. The epithermal code GAM uses modified cross sections for the resonance absorbers prepared from the double heterogeneous resonance ZUT-DGL code [25].
The nuclear cross section previously calculated are then used in the 3D finite difference diffusion code CITATION [26], coupled with the 2D fluid dynamic code THERMIX, in order to calculate the neutron and the temperatures distributions [27]. The diffusion code is embedded with the burn-up code FEVER, able to treat up to 200 different burn-up zones [28].
The diffusion part of the code is repeated along with the spectrum code calculations when significant changes in the spectrum indexes are found.
Finally, the fuel management and the cost modules will perform the fuel shuffling and the general evaluation of the reactor and fuel element life history.
Although, the code is still used for generic HTGR design, from nowadays point of view

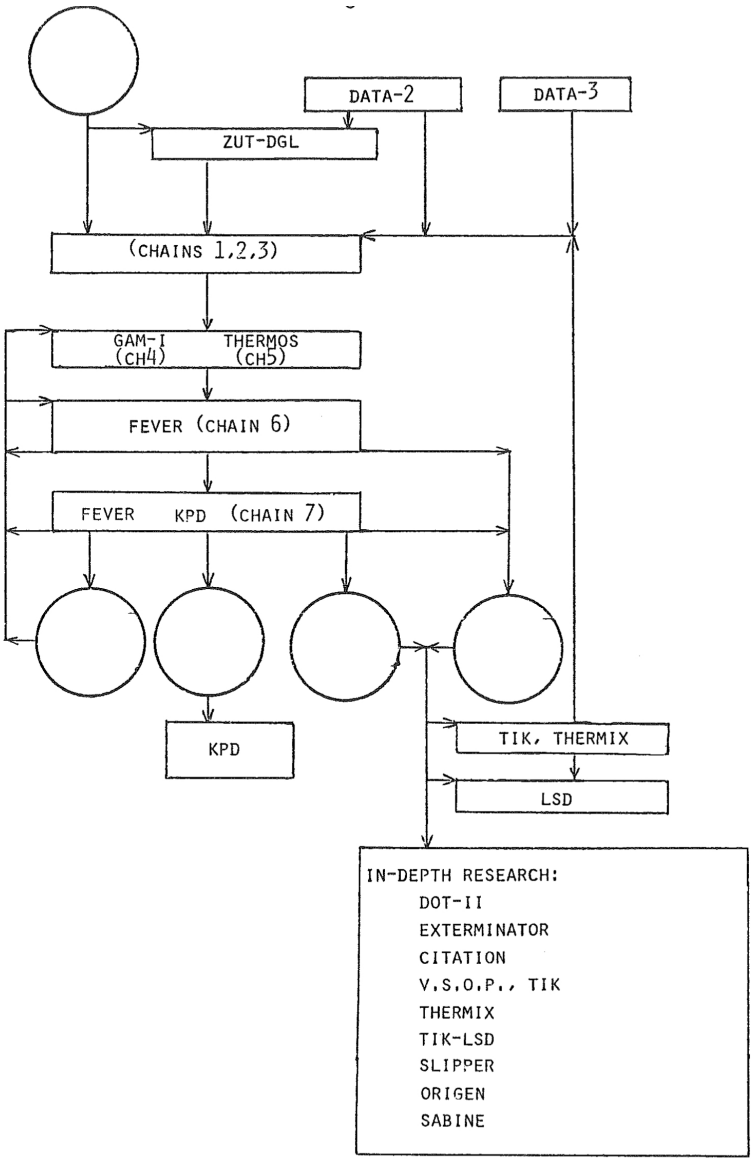

Figure 1.12: VSOP module scheme [20]

it suffers from its outdated programming style and the lack of proper documentation.

1.5 HTGR simulations with MGT-3D and VSOP

Since its early developments, MGT-3D was the code designated to handle HTGR transient and accident simulations. However, MGT-3D is not able to perform long term operations like fuel shuffling or burn-up [29]; it is therefore unable to bring a reactor to equilibrium. The code is supposed to work as part of a tool chain that involves necessarily VSOP, the interface code that "translates" VSOP output for MGT-3D, and a code like MCNP [30] or ZUT [25] to handle the double heterogeneity issues.

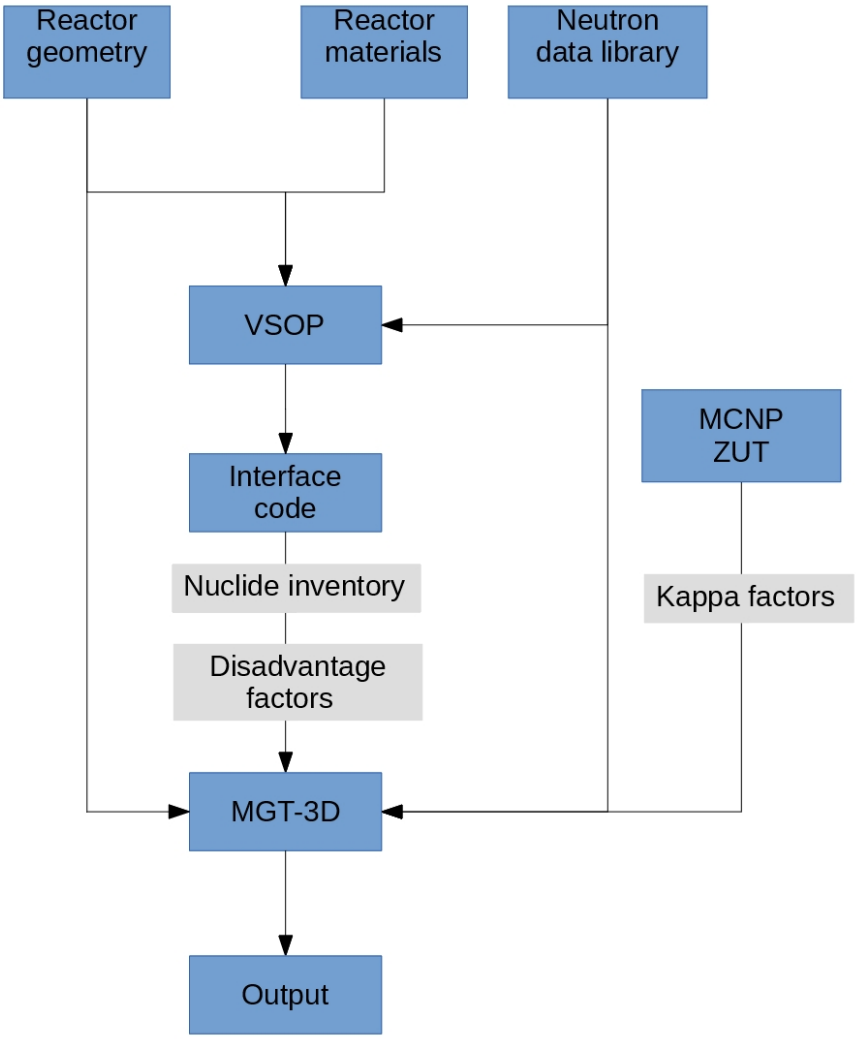

Figure 1.13: MGT-3D / VSOP tool chain

Following figure 1.13, the reactor geometry and material data, along with the necessary neutron cross section data library, are used in VSOP to bring the reactor to an equilibrium state. Subsequently, from the VSOP output, the interface code generates the nuclear inventory file for MGT-3D along with thermal disadvantage factors, to be used in the MGT-3D spectrum code TISPEC. However, the geometry data need to be inputted into MGT-3D in a different file. In addition, it is worth noting that the neutron cross section data libraries employed by the two codes are different.

Finally, in order to treat HTGR double heterogeneity, the so called *kappa factor* is used. The idea of using an empirical factor to alter the homogeneous resonance integrals in order to represent heterogeneous cases was first introduced with the code MUPO [32]; this kappa factor is defined as the value that best matches the homogeneous curve to the heterogeneous one for the particular reactor design and operating conditions. In the past, codes like MCNP or ZUT where used to generate the heterogeneous resonance integrals.

1.6 Thesis motivation

Many different nuclear and spectrum codes were developed during the past 40 years at Forschungszentrum Jülich (FZJ). Sadly, many of those codes are today abandoned, suffer from outdated coding style or lack proper documentation.
During the past six years, a new innovative system code has been under development at FZJ, in close collaboration with the RWTH University Institute of Reactor Safety and Reactor Technology, under the name of High temperature gas reactor Code Package (HCP). The aim of this code is to allow fully integrated HTGR safety simulations, exploiting the latest object oriented capabilities in a user-friendly environment.
The system code is a collection of modules, all linked and controlled by the so-called backbone. Most of these modules are newly implemented with the exception of MGT-FD and MGT-N, respectively in charge of the fluid dynamic and neutronics calculations.
At the beginning of this work, it was decided that the focus of the thesis should have been the analysis and the re-implementation of the neutronics part of MGT-3D. That is MGT-N. However, it became gradually clear that more pressing and important work was needed at a more fundamental level, namely the spectrum code and the library generator.
The spectrum code TISPEC is derived from the 0D MUPO code based on neutron diffusion theory [31]. The energy domain is discretized in 43 energy groups (MUPO energy structure [32]) and the system is solved numerically using the Gauss-Seidel method [33].
TISPEC, as other previously developed codes like TOTMOS [34], has its own neutron cross section data library format and different library versions contain different numbers of resonant isotopes and scattering matrices and use different versions of the ENDF raw data [35], sometimes they are even mixed. Moreover, for some of these libraries it is not fully clear how they were generated and who the author was. This, of course, was far from the HCP's goal of having a unique and consistent shared data library among the different modules of the code package.
Furthermore, the MUPO library adopts a generic fission neutron energy distribution

for every fissionable isotope and it has to be limited to the highest nine energy groups.

The method chosen to deal with the double heterogeneity neutron resonance calculations, that is the *kappa factor*, proved to be neither flexible nor very accurate. As reported in [36], a difference of 10 %, with respect to the more accurate heterogeneous resonance integral ZUT calculation, is found for background cross sections above 800 barn and between 10 and 20 % below 800 barn.

In addition, a different kappa factor is required for each reactor design and operating condition, leading to external code dependencies, doubling of inputs and use of different libraries. However, in TISPEC, a kappa value of 0.4 is always used for ^{238}U regardless of the fuel geometry, the heavy metal content or the coolant, adding another source of error.

Getting rid of the kappa factor the thermal disadvantage factor dependencies and finding an accurate, fast and robust way to deal with the double heterogeneity issue, avoiding the usage of semi-empirical approaches or external codes became one of the main focuses of this thesis.

The old spectrum code was found difficult to maintain or integrate with the new library generator or the new HCP framework, due to its outdated code style. Additionally, the code lacks proper physics and technical documentation. For all these reasons, it was decided to discard TISPEC and to move forward with a new spectrum code.

TRISHA (TRansport Integral Spectrum and Homogenization Application) was developed to be a flexible and fully automated neutron broad cross sections generator that makes use of latest C++ object oriented features, fully integrated with HCP data model and able to be used for stationary and transient calculations.

In contrast to what was happening in the past decades with modular system codes like VSOP, where each module's input needed to be supplied with information already given or calculated in some other module, in HCP the approach is radically different. Every module in HCP is designed to work only with minimal information from the user. In several cases, Once the data on the reactor's geometry, materials and the scenario are provided, only few additional parameters are needed for every module; mostly concerning which method to be used by the module or a convergence criteria. This is part of HCP strategy to increase the user-friendliness of the system code and it is particularly evident in the spectrum code TRISHA where no information on the unit cell needs to be provided; everything is handled internally.

An significant part of this thesis was devoted to design and implement a new library generator, able to treat with a sufficient degree of accuracy the double heterogeneity issues typical of the HTGR fuel designs. The library generator needed to be accurate, fast, user-friendly and integrated in the HCP data model to fully exploit the HCP modular capabilities.

Finally, the re-implementation and the refactoring, within the HCP framework, of the neutronics part of MGT-3D (now called MGT-N) needed to be consistent and in line with the results given by the original MGT-3D code.

2 Neutron transport theory

2.1 Introduction

My thesis is based on reactor physics theories described in [37, 38, 39]. For ease of reference, in this section I discuss the key concepts which my work is based upon. The most important factors characterizing the behavior of a nuclear reactor are the spatial and energetic distributions of neutrons that determine the rate of various nuclear reactions inside the core. In principle, an exact solution to this problem can be found applying the Boltzmann equation, originally developed by Ludwig Boltzmann to describe the kinetics of gases more than a century ago [37].
This equation was applied in the 1930s and 1940s in a limited number of fields, like the study of radiation transport in stellar atmospheres. Those studies led to the development of analytical tools and solutions, like the Weiner-Hopf technique, that are part of every reactor physics textbook but nowadays they have little practical applications. The field bloomed with the rise of the nuclear reactor technology, neutron transport methods were then used in a broader range of geometrical and physical configurations found in nuclear reactors and radiation shielding applications. With the rapid evolution and advance of digital computers, increasingly sophisticated numerical methods have been developed over the last sixty years, allowing us to use multiregion and multidimension transport codes in the design and the safety analysis of nuclear reactors and other applications [37].

2.2 Assumptions

The following assumptions need to be met in order to derive the neutron transport equation [37]:

1. *Particles may be considered as points.* The quantum mechanical wave length of the neutron is small compared to the atomic diameter.

2. *Particles travel in straight lines between point collisions.* The path followed by neutrons, since they have no charge, is not altered by long-range electrical or magnetic forces. Only short-range forces acting in the event of a collision with nucleus are considered.

3. *Particle-particle interactions may be neglected.* Neutron densities in nuclear reactors are always small compared to atomic densities.

4. *Collisions may be considered instantaneous.* After a collision, the emerging particles are emitted immediately for all practical purpose. The only exception

of any practical significance is in the fission reaction in which a small fraction of the fission products decay by neutron emission after some delay.

5. *The material properties are assumed to be isotropic.* This assumption can be considered valid for the reactor materials, with only one exception. The interactions of neutrons at very low energies with the reactor media can result in directionally dependent trajectories if the media consists of crystals preferentially aligned in one direction, as in the case of graphite.

6. *The composition of the materials under consideration is assumed to be time-dependent.* This is achieved through an iterative procedure. As a first step the particle density distribution is calculated for a fixed temperature and composition, and the material property changes are estimated. The modified compositions are then employed in a second transport calculation in order to evaluate the new particle density distribution. The procedure continues until the iterative process converges.

7. *Only the expected or mean value of the particle density distribution is considered.* Fluctuations about the mean value due to low particle density distribution must be integrated over a large enough region of space-energy-angle phase space or over a large enough time span for the mean value to have meaning.

2.3 Neutron transport equation derivation

Consider the change dN in time dt of the number of neutrons with velocity d^3v about $\mathbf{v}$ which are located in a small volume V with surface S about the point $\mathbf{r}$. We have [38]:

$$dN = d^3v dt \int_V \frac{\partial \psi(\mathbf{r}, \mathbf{v}, t)}{\partial t} d^3r \tag{2.1}$$

$\psi(\mathbf{r}, \mathbf{v}, t)$ is called neutron angular density and $\psi(\mathbf{r}, \mathbf{v}, t)d^3r d^3v$ is the expected number of neutrons in the volume element d^3r about the point $\mathbf{r}$, whose velocities lie in the element of velocity space d^3v about $\mathbf{v}$ at time t. The number of neutrons in the volume V is the result of a balance relation:

$$\begin{aligned} dN = &- (a) \text{ net number of neutrons flowing out of } S \text{ during } dt \\ &- (b) \text{ number of neutrons suffering collisions } V \text{ during } dt \\ &+ (c) \text{ number of neutrons of velocity } \mathbf{v} \text{ produced in } V \text{ during } dt \text{ by collisions} \\ &+ (d) \text{ number of neutrons of velocity } \mathbf{v} \text{ produced in } V \text{ during } dt \text{ by sources} \end{aligned} \tag{2.2}$$

Term (a) is the so-called streaming term accounting for the neutrons which leave or enter without changing the velocity:

$$(a) = d^3v dt \int_S \mathbf{j}(\mathbf{r}, \mathbf{v}, t) \cdot \mathbf{n}_0 dS \tag{2.3}$$

$\mathbf{n}_0$ is the outward normal to dS, $\mathbf{j}(\mathbf{r}, \mathbf{v}, t)$ is the neutron angular current and $\mathbf{j}(\mathbf{r}, \mathbf{v}, t) \cdot \mathbf{n} dS d^3v dt$ is equal to the number of neutrons in d^3v about $\mathbf{v}$ which cross a small area dS with unit normal $\mathbf{n}$ in a time dt. Applying the Gauss's theorem we derive:

$$(a) = d^3v dt \int_V \nabla \cdot \mathbf{j}(\mathbf{r}, \mathbf{v}, t) dV. \tag{2.4}$$

Terms (b) and (c) account for those neutrons leaving and entering element d^3v with no change in position:

$$\begin{aligned} (b) &= d^3v dt \int_V v\psi(\mathbf{r}, \mathbf{v}, t) \Sigma_t(\mathbf{r}, \mathbf{v}) d^3r \\ (c) &= d^3v dt \int \int_V v' \psi(\mathbf{r}, \mathbf{v}', t) \Sigma_s(\mathbf{v}' \to \mathbf{v}, \mathbf{r}) d^3v' d^3r \end{aligned} \tag{2.5}$$

where v and $\mathbf{v}$ are respectively the speed and the velocity, $\Sigma_t(\mathbf{r}, \mathbf{v})$ is the total cross section and $\Sigma_s(\mathbf{v}' \to \mathbf{v}, \mathbf{r})$ is the scattering cross section. Finally

$$(d) = d^3v dt \int_V \theta(\mathbf{r}, \mathbf{v}, t) d^3r. \tag{2.6}$$

In this case $\theta(\mathbf{r}, \mathbf{v}, t) d^3r d^3v dt$ is the number of neutrons inserted into d^3r at $\mathbf{r}$ and d^3v at $\mathbf{v}$ during dt. The definition of the source term density $\theta(\mathbf{r}, \mathbf{v}, t)$ can be further expanded yielding:

$$\theta(\mathbf{r},\mathbf{v},t) = \chi(v)\int \nu\Sigma_f(\mathbf{r},\mathbf{v})\psi(\mathbf{r},\mathbf{v},t)d^3v + \theta_{ex}(\mathbf{r},\mathbf{v},t). \tag{2.7}$$

Where ν is the number of neutrons per fission, χ is the fission neutron spectrum, Σ_f is the fission cross section and θ_{ex} is the external source. From equation 2.1 and 2.2 noticing that the volume V is arbitrarily chosen, after some manipulation and using the identity $\nabla \cdot v\psi = v \cdot \nabla\psi$, we derive:

$$\frac{\partial\psi(\mathbf{r},\mathbf{v},t)}{\partial t} + v\cdot\nabla\psi(\mathbf{r},\mathbf{v},t) + v\Sigma_t(\mathbf{r},\mathbf{v}) = \theta(\mathbf{r},\mathbf{v},t) + \int v'\psi(\mathbf{r},\mathbf{v}',t)\Sigma_s(\mathbf{v}'\to\mathbf{v},\mathbf{r})d^3v'. \tag{2.8}$$

This equation is a hyperbolic equation in both the steady-state and time-dependent forms. The time-dependent solution is unique and non-negative provided all cross sections, sources, and initial boundary flux data are known and non-negative.
A more customary form of equation 2.8 is obtained writing $\mathbf{v}$ as $v\hat{\mathbf{\Omega}}$ and switching for velocity dependent variables to energy dependent variables:

$$\begin{aligned}\frac{1}{v}\frac{\partial\psi(\mathbf{r},E,\hat{\mathbf{\Omega}},t)}{\partial t} + \hat{\mathbf{\Omega}}\cdot\nabla\psi(\mathbf{r},E,\hat{\mathbf{\Omega}},t) + \Sigma_t(\mathbf{r},E,\hat{\mathbf{\Omega}}) = \\ \int_{4\pi}\int_0^{+\infty}\Sigma_s(\mathbf{r},E'\to E,\hat{\mathbf{\Omega}}'\to\hat{\mathbf{\Omega}})\psi(\mathbf{r},E',\hat{\mathbf{\Omega}}',t)d\hat{\mathbf{\Omega}}'dE' + \theta(\mathbf{r},E,\hat{\mathbf{\Omega}},t).\end{aligned} \tag{2.9}$$

2.4 Neutron diffusion equation

The neutron transport equation can be brought to a more manageable form reducing it in a second-order ordinary differential equation. This is accomplished assuming three valid fundamental approximations. Although some of these assumptions make its use questionable, the neutron diffusion equation is still widely applied in routine reactor physics calculations due to the great simplicity of its numerical form. The starting point is the angular integrated form of the equation 2.9:

$$\begin{aligned}\frac{1}{v}\frac{\partial\phi(\mathbf{r},E,t)}{\partial t} + \nabla\cdot\mathbf{J}(\mathbf{r},E,t) + \Sigma_t(\mathbf{r},E) = \\ \int_0^{+\infty}\Sigma_s(\mathbf{r},E'\to E)\phi(\mathbf{r},E',t)dE' + \theta(\mathbf{r},E,t).\end{aligned} \tag{2.10}$$

where $\phi(\mathbf{r},E,t)$ is equal to $\int_{4\pi}\psi(\mathbf{r},E,\hat{\mathbf{\Omega}},t)d\hat{\mathbf{\Omega}}$ and $\mathbf{J}(\mathbf{r},E,t)$, equal to $\int_{4\pi}\hat{\mathbf{\Omega}}\cdot\mathbf{j}(\mathbf{r},E,\hat{\mathbf{\Omega}},t)d\hat{\mathbf{\Omega}}$, is the so called neutron current density.

As it can be easily seen, in order to find the flux distribution from equation 2.10, a second equation is needed for the unknown variable $\mathbf{J}(\mathbf{r}, E, t)$. This is accomplished multiplying equation 2.10 by $\hat{\mathbf{\Omega}}$ and integrating it again,

$$\begin{aligned}\frac{1}{v}\frac{\partial \mathbf{J}(\mathbf{r}, E, t)}{\partial t} + \nabla \cdot \int_{4\pi} \hat{\mathbf{\Omega}}\hat{\mathbf{\Omega}}\psi(\mathbf{r}, E, \hat{\mathbf{\Omega}}, t)d\hat{\mathbf{\Omega}} + \Sigma_t(\mathbf{r}, E) = \\ \int_0^{+\infty} \Sigma_s(\mathbf{r}, E' \to E)\phi(\mathbf{r}, E', t)dE' + \int_{4\pi} \theta(\mathbf{r}, E, \hat{\mathbf{\Omega}}, t)d\hat{\mathbf{\Omega}}.\end{aligned} \tag{2.11}$$

Assuming that the angular dependency can be adequately approximated by only a linearly anisotropic angular dependency [14]:

$$\psi(\mathbf{r}, E, \hat{\mathbf{\Omega}}, t) \cong \frac{1}{4\pi}\phi(\mathbf{r}, E, t) + \frac{3}{4\pi}\mathbf{J}(\mathbf{r}, E, t) \cdot \hat{\mathbf{\Omega}}, \tag{2.12}$$

that the source (fission) can be considered an isotropic source:

$$\theta(\mathbf{r}, E, \hat{\mathbf{\Omega}}, t) \cong \frac{1}{4\pi}\theta(\mathbf{r}, E, t), \tag{2.13}$$

a simpler version of the previous system can be derived:

$$\begin{aligned}\frac{1}{v}\frac{\partial \phi}{\partial t} + \nabla \cdot \mathbf{J} + \Sigma_a \phi = \theta \\ \frac{1}{v}\frac{\partial \mathbf{J}}{\partial t} + \nabla \cdot \phi + \Sigma_{tr}\mathbf{J} = 0\end{aligned} \tag{2.14}$$

Furthermore, assuming that the neutron current density changes can be considered slow compared to the mean collision time:

$$\frac{\partial |\mathbf{J}|}{\partial t} \approx 0; \tag{2.15}$$

from the second equation of the system 2.14, we can obtain the neutron current $\mathbf{J}$ as a function of the neutron flux and it can be inserted in the first equation of the system finally yielding:

$$\frac{1}{v}\frac{\partial\phi(\mathbf{r},E,t)}{\partial t} + \nabla\cdot D(\mathbf{r},E)\nabla\phi(\mathbf{r},E,t) + \Sigma_t(\mathbf{r},E) = \int_0^{+\infty}\Sigma_s(\mathbf{r},E'\to E)\phi(\mathbf{r},E',t)dE' + \theta(\mathbf{r},E,t). \tag{2.16}$$

It is notable how the weak angular dependence assumption is responsible for the simplification of the neutron current variable, allowing it to be written as a function of the neutron flux.

If we define the neutron diffusion constant as $D(\mathbf{r},E) = [3(\Sigma_t - \bar{\mu}\Sigma_s)]^{-1}$ where $\bar{\mu}_0$, the average scattering angle cosine, is equal to $\frac{2}{3A}$ and A is the atomic mass number we arrive to Fick's law:

$$\mathbf{J}(\mathbf{r},E,t) = -D(\mathbf{r},E)\nabla\phi(\mathbf{r},E,t). \tag{2.17}$$

Detailed studies and comparisons indicate how poorly the diffusion approximation performs close to the boundaries of the system or where the properties of the media show great changes, for instance, near localized sources or close to strong absorbing materials. This seems to be a consequence of the weak angle dependence approximation 2.12 and in these cases neutron transport theories need to be applied.

2.5 B_1 neutron transport equation

While the derivation of the neutron diffusion equation relies upon a neutron flux series expansion, a different path can be followed in the derivation of the B_n transport equations [40]. Assuming that the angular variation of the scattering cross section depends only on the scattering angle $\mu = \hat{\Omega}\cdot\hat{\Omega}'$ we can expand the cross section in a set of Legendre polynomials of μ [41]:

$$\Sigma_s(\mathbf{r},E'\to E,\hat{\mathbf{\Omega}}'\to\hat{\mathbf{\Omega}}) = \sum_{l=0}^{\infty}\frac{2l+1}{4\pi}\Sigma_{sl}(\mathbf{r},E'\to E)P_l(\mu). \tag{2.18}$$

For sake of simplification, let us consider a homogeneous medium and a time-independent one-dimensional planar geometry:

$$\begin{aligned} \mu\frac{\partial\psi(x,E,\mu)}{\partial x} + \Sigma_t(x,E,\mu) = \\ \int_{4\pi}\int_0^{+\infty} \Sigma_s(x,E'\to E,\hat{\mathbf{\Omega}}'\to\hat{\mathbf{\Omega}})\psi(x,E,\mu)dE'd\hat{\mathbf{\Omega}}' \\ +\theta(x,E,\mu). \end{aligned} \tag{2.19}$$

The central approximation of this method concerns the spatial distribution and its independence from the neutron energy within the medium considered. It is indeed assumed that spatial dependence of the neutron flux and the current can be both represented making use of the buckling, B, as it follows:

$$\psi(x,E,\mu) = e^{-iBx}\Psi(B,\mu,E). \tag{2.20}$$

A sine wave dependency or exponential dependency with an imaginary exponential is reasonably expected for multiplying systems [42]. Inserting equation 2.18 into 2.19, assuming a linear anisotropic dependence of the scattering ($l \leq 1$ in equation 2.18), assuming that the fission source is isotropic and integrating over the angular variable, after lengthy algebraic manipulations we arrive to the following B_1 system [39]:

$$\begin{aligned} \Sigma_t(E)\Psi(E) + iBJ(E) = \int \Sigma_{s0}(E'\to E)\Psi(E')dE' + \theta(E) \\ -iB\Psi(E) + 3\alpha(B,E)\Sigma_t(E)J(E) = 3\int \Sigma_{s1}(E'\to E)J(E')dE' \end{aligned} \tag{2.21}$$

The B_1 equations are almost identical to the P_1 ones, the only difference lies in the α parameter. In the case of the P_1 equations α is considered to be one. The B_1 equations seem to perform slightly better than P_1 ones and nowadays they are widely used in deterministic as well as Monte Carlo codes for generating broad energy group cross sections. An approximated expression for α, when the neutron leakage is considered negligible with respect to the neutron total cross section $|y| = |B/\Sigma_t| \leq 0.1$, can be obtained yielding

$$\alpha(B,E) \cong \frac{1}{3}y\Big[\frac{1-(y/3-y^2/5+y^3/7)}{y/3-y^2/5+y^3/7}\Big]. \tag{2.22}$$

3 Neutron resonance theory

3.1 Introduction

The success and the applicability of the neutron diffusion equation for standard reactor physics calculations relies upon the correct determination of the intra-group fluxes $\phi(\mathbf{r}, E)$ in order to define multigroup diffusion constants like [9]:

$$\Sigma_a^g(\mathbf{r}) = \frac{\int_{g-1}^{g} \Sigma_a(\mathbf{r}, E)\phi(\mathbf{r}, E)dE}{\int_{g-1}^{g} \phi(\mathbf{r}, E)dE}. \tag{3.1}$$

Due to the complicated nature of the resonance energy dependency, the actual cross section data, coming from neutron cross data libraries like ENDF/B [35] or JEFF [43], contain hundreds of thousands of energy points for the most important resonance isotopes [14]. Direct simulations of such ultrafine energy groups with neutron transport codes become practically impossible so that a careful treatment and condensation of such energy dependency needs to be carried out, see fig. 3.1.
The contribution of the resonance absorptions from ^{238}U or ^{232}Th in high temperature gas reactors is of the utmost importance for the control of the reactor. The amount of fertile materials together with the Doppler effect have a strong impact on the reactivity of the system, determining the temperature coefficients, the dynamic behavior and ultimately the safety of the reactor. It is also worth mentioning that although resonances involve all sorts of processes like scattering, fission and absorption, only the latter ones are of primary importance for thermal reactors. The same conclusions apply for fission products or structural materials resonances, which are only important for fast reactors [8].
The rather complicated energy dependent cross sections coupled with double heterogeneity of the fuel make these calculations very difficult and they can be carried out only applying transport or Monte Carlo methods.

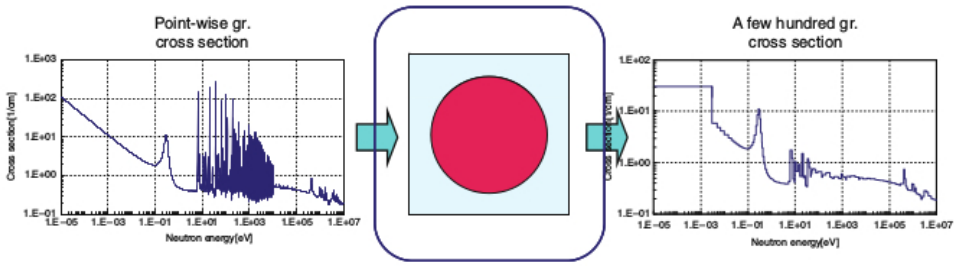

Figure 3.1: Resonance calculation diagram [9]

3.2 Resonance theory in homogeneous media

The Boltzmann transport equation in a homogeneous infinite system, considering the scattering isotropic, can be brought to the following form [9]:

$$\Sigma_t(E)\phi(E) = \int_0^\infty \Sigma_s(E' \to E)\phi(E')dE' + \frac{\chi(E)}{k_{eff}} \int_0^\infty \nu\Sigma_f(E')\phi(E')dE'. \tag{3.2}$$

Under the assumptions that the elastic scattering is the prevailing process and the energy range considered is far from fission neutron energies it can be simplified to

$$\Sigma_t(E)\phi(E) = \frac{1}{1-\alpha}\int_E^{E/\alpha} \Sigma_s\phi(E)'\frac{dE'}{E'} \tag{3.3}$$

where α is equal to $\left(\frac{A-1}{A+1}\right)$, with A being the atomic mass. If the medium containing only one isotope can be considered as a pure scatterer, like in the case of water due to the weak hydrogen absorption ($A = 1$), then the previous expression can be further simplified and the analytical solution for the neutron flux is found to be

$$\phi(E) = \frac{S}{\Sigma_t(E)E}. \tag{3.4}$$

S represents the source term in this case. When the medium contains isotopes with $A > 1$ due to the fact the neutron cannot lose all its energy in a single encounter, the slowing down equation solution gets far more complicated and discontinuities arise in the energy neutron flux distribution [44]. However, it can be observed that at energies below $\alpha^3 E_0$, where E_0 is the source energy, the discontinuities smooth out and the so called asymptotic flux distribution is reached:

$$\phi(E) = \frac{S}{\xi\Sigma_t(E)E} \tag{3.5}$$

where ξ is the average increase in lethargy per collision:

$$\xi = 1 - \frac{(A-1)^2}{2A} ln\left(\frac{A+1}{A-1}\right) \cong \frac{2}{A+2/3}. \tag{3.6}$$

If we can assume that the average energy loss of the neutron undergoing an elastic collision with both moderator or absorber is much larger than the practical width of the resonance considered, that is:

$$\Gamma_p \ll \frac{(1-\alpha_{m,f})E_r}{2}. \tag{3.7}$$

Where Γ_p is the practical width of the resonance at the energy of E_r. Furthermore, if it is assumed that the neutron flux distributions can be represented by their asymptotic forms and that the scattering of both moderator and absorber (assumed to be equal to its microscopic potential scattering σ_p) is constant over the energy range, we yield:

$$\phi(E) = \frac{\sigma_{p,r} + \sigma_0}{\sigma_{t,r}(E) + \sigma_0} \frac{1}{E}. \tag{3.8}$$

In this case, the subscript r represents the resonant isotope and σ_0 is the so-called microscopic background cross section defined as:

$$\sigma_0 = \frac{\sum\limits_{k \neq r} N_k \sigma_{p,k}}{N_r} \tag{3.9}$$

where N_k is the nuclear density of the isotope k. This very famous approximation is known under the name of "narrow resonance approximation" and it shows to be fairly good at least for resonances far from the thermal range [44]. Similar expedients can lead to different approximations, like the wide or intermediate resonance approximation [9], that appear to be more or less accurate according to the energy range and the application. However, the narrow resonance approximation is particularly important because the equivalence theory, as we will see later, is strictly valid only under its assumptions.

3.3 Resonance theory in heterogeneous media

The absorption of neutrons close to the high resonance peaks lead to a very complicated shape of the neutron flux in the proximity of a resonance. Usually the high peaks of the resonances create dips in the energy flux distribution and since the absorption rate is the product of the absorption cross section and the neutron flux, the absorption rate appears to be reduced [9]. This is a very important effect known as energetic self-shielding. From figure 3.2, it is possible to observe how the real flux is far from the asymptotic one, $\propto \frac{1}{E}$, due to the resonance perturbation in proximity of the peak.

A similar effect occurs when the fuel shows heterogeneous properties, like in the case of HTGR fuel. Neutrons in the resonance energy range that are moving from the

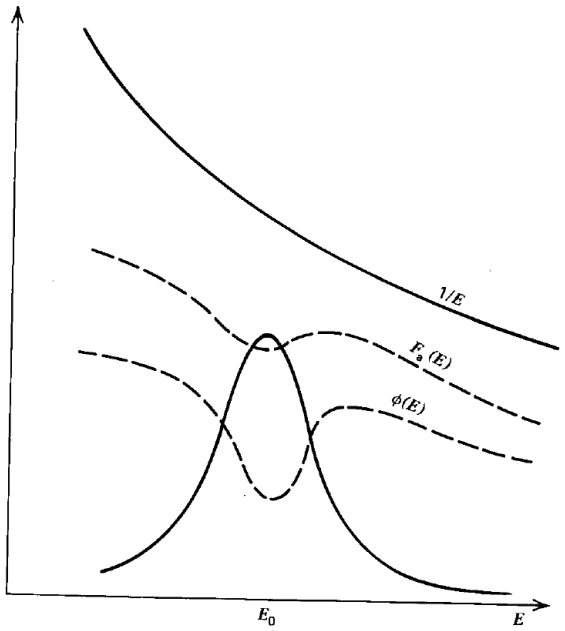

Figure 3.2: Energetic self-shielding [44]

moderator to the fuel are mostly absorbed in the outer shell of the fuel. This leads to a flux depression in the neutron spatial distribution; the neutron absorption is in this case reduced by the spatial self-shielding that takes place at the boundaries of the fuel zone.

The treatment of the heterogeneity effects requires modifications of equation 3.2, and the use of the Dancoff factor as it will be shown later. The unit cell lattice is usually divided in two zones, fuel and moderator, and a collision probability form of the transport equation is applied [8]:

$$V_0\Sigma_{t,0}(E)\phi_0(E) = (1-P_0)V_0\left[\frac{1}{1-\alpha_0}\int_E^{E/\alpha_0}\phi_0(E)\Sigma_{s,0}\phi_0(E')\frac{dE'}{E'}+\right.$$
$$\left.\frac{1}{1-\alpha_{m,0}}\int_E^{E/\alpha_{m,0}}\phi_0(E)\Sigma_{sm,0}\phi_0(E')\frac{dE'}{E'}\right] + \frac{P_1V_1}{1-\alpha_1}\int_E^{E/\alpha_1}\phi_1(E)\Sigma_{s,1}\phi_1(E')\frac{dE'}{E'} \tag{3.10}$$

Often and also in HTGR cases, the heterogeneous resonance calculations are carried out considering the fuel region consisting of an absorber and a moderator while the moderator region consists of only one scatterer. All the parameters concerning the fuel region are depicted with the subscript 0 while the ones concerning the moderator use 1. The moderator belonging to the fuel zone is represented by the symbol $m, 0$. V is the volume of the region considered and P_0 and P_1 are so-called escape probabilities defined as: the probability that a neutron born in a certain

region (0 or 1) will have its next collision outside the region. Collision probability properties and their calculation will be dealt with in section 3.4.
Using a well-known reciprocity relation in collision probability theory:

$$P_0 V_0 \Sigma_{t,0} = P_1 V_1 \Sigma_{t,1}, \tag{3.11}$$

Equation 3.10 can be brought to a simpler form

$$\Sigma_{t,0}(E)\phi_0(E) = (1-P_0)\left[\frac{1}{1-\alpha_0}\int_E^{E/\alpha_0}\phi_0(E)\Sigma_{s,0}\phi_0(E')\frac{dE'}{E'} + \frac{1}{1-\alpha_{m,0}}\int_E^{E/\alpha_{m,0}}\phi_0(E)\Sigma_{sm,0}\phi_0(E')\frac{dE'}{E'}\right] + \frac{P_0\Sigma_{t,0}}{1-\alpha_1}\int_E^{E/\alpha_1}\phi_1(E)\Sigma_{s,1}\phi_1(E')\frac{dE'}{E'}. \tag{3.12}$$

However, the starting point of many resonance calculation codes requires another assumption, that is, the neutron flux in the moderator region can be represented by its $1/E$ asymptotic form. This further assumption eliminates the unknown moderator neutron flux from the previous equation:

$$\Sigma_{t,0}(E)\phi_0(E) = (1-P_0)\left[\frac{1}{1-\alpha_0}\int_E^{E/\alpha_0}\phi_0(E)\Sigma_{s,0}\phi_0(E')\frac{dE'}{E'} + \frac{1}{1-\alpha_{m,0}}\int_E^{E/\alpha_{m,0}}\phi_0(E)\Sigma_{sm,0}\phi_0(E')\frac{dE'}{E'}\right] + \frac{P_0\Sigma_{t,0}}{E}. \tag{3.13}$$

This formulation, used in many codes like ZUT [25] or MICROX [45], is then discretized in thousands of energy groups and solved numerically, assuming that the escape probability function $P_0(E)$ is known.

3.4 Equivalence theory and neutron escape probability

The neutron escape probability can be mathematically defined as

$$P(E) = \frac{1}{4\pi V_f}\int_{\mathbf{n}\cdot\mathbf{\Omega}} d\mathbf{\Omega}\int_S(\mathbf{n}\cdot\mathbf{\Omega})dS\int_0^l e^{(-\Sigma_{t,f}(E)s)}ds, \tag{3.14}$$

where $\mathbf{\Omega}$ is the flying direction of the neutron, s is the distance between the surface in that direction and the point of birth of the neutron while V and S are respectively

the volume and the surface of the fuel lump. The previous form can be greatly simplified making use of the chord length distribution concept, yielding [46]:

$$P(E) = \frac{1}{\Sigma_{t,f}(E)\langle l\rangle}\int_0^\infty dl f(l)[1 - e^{(-\Sigma_{t,f}(E)l)}]. \tag{3.15}$$

In this case, $\langle l\rangle$ is the average chord length of the fuel lump and it is defined as $\frac{4V}{S}$. For the chord length distribution we assume an exponential decay law:

$$f(l) = \frac{1}{\langle l\rangle}e^{-\frac{l}{\langle l\rangle}}. \tag{3.16}$$

Although this approximation is far from being exact, it is important for historical reasons. Indeed, it leads to the Wigner rational approximation of the escape probability, equation 3.17, and to the equivalence theory [47]. So, applying equation 3.16 to equation 3.15 we obtain:

$$P(E) = \frac{1}{\Sigma_{t,f}(E)\langle l\rangle + 1} = \frac{\Sigma_e}{\Sigma_{t,f}(E) + \Sigma_e}. \tag{3.17}$$

The inverse average chord length takes the dimension of a macroscopic cross section when expressed as $\Sigma_e = \frac{1}{\langle l\rangle}$ and Σ_e is called escape cross section. Introducing equation 3.17 into 3.13 leads us to the formula being solved numerically in NJOY; that is going to be better described later in 4.7.3. If we further assume asymptotic neutron flux distributions, like in the homogeneous case, an analytical solution, expressed in terms of microscopic cross sections, even for the heterogeneous case can be obtained:

$$\phi(E) = \frac{\sigma_{p,r} + \sigma_0 + \sigma_e}{\sigma_{t,r}(E) + \sigma_0 + \sigma_e}\frac{1}{E}. \tag{3.18}$$

Comparing this equation with the homogeneous one, eq. 3.8, we can deduce two important consequences:

1. Heterogeneous lattices with the same escape cross section have also the same resonance integral regardless of the moderator.

2. If the background cross section for a heterogeneous lattice is modified like $\sigma_{0,het} = \sigma_{0,hom} + \sigma_e$ it can be regarded as a homogeneous lattice.

The previous statements are also known as *first and second Wigner's equivalence theorems* [44]. One very important consequence of these theorems is that the tabulated

resonance integrals or cross sections calculated for homogeneous cases can be used for heterogeneous cases as well, if the right background cross section is provided.
The two theorems still hold if a correction factor is applied to the escape cross section. It can be proven that the Wigner approximation underestimates the escape probability when $\sigma_e R \approx 1$, where R is the radius of the fuel lump. This led researchers to find correction factors in order to improve the accuracy of $P(E)$. One of the most famous factors is the Bell factor. To be applied in the following way:

$$P(E) = \frac{a\Sigma_e}{\Sigma_{t,f}(E) + a\Sigma_e}. \tag{3.19}$$

This factor is usually calculated with Monte Carlo codes making use of its inverse definition:

$$a = \frac{P(E)}{1 - P(E)}\Sigma_{t,f}\langle l \rangle. \tag{3.20}$$

Although it will be exact only at some particular energy point, it generally improves the accuracy of the formula in the whole energy range.

3.5 Dancoff factor calculation

If we consider a single kernel embedded in an infinite moderator, it is obvious that a neutron that escapes from the kernel will have its next collision in the moderator zone. On the other hand, if the distance between the kernel is comparable with the mean free path then its possible for the neutron to interact with different kernels in the resonance energy range. This is typically the case in HTGR pebbles where the average distance among the coated particles is on the millimiter scale while the mean free path for a resonance energy neutron is about 2.5 cm [48].
It should be clear at this point that such spatial heterogeneity effects, arising from the interactions among the kernels, are going to affect the escape probabilities present in the heterogeneous neutron transport theory formulas shown in 3.3.
Although many methods have been studied and developed in the past, like the ZUT approach where the energy dependent escape probability is evaluated solving numerically a series of integrals [25], our starting point is the Dancoff and Ginsburg method, developed in the 1940s. It modifies the escape probability making use of an energy independent parameter C [49]:

$$P^*(E) = P(E)\frac{1 - C}{1 - C(1 - \Sigma_{t,f}\langle l \rangle P(E))}. \tag{3.21}$$

The Dancoff-Ginsburg factor C can be defined as the probability of a neutron leaving the kernel in a random direction and entering in another kernel regardless of the fact that the other kernel belongs to the same pebble or another one.

Inserting the Wigner approximation 3.17 into 3.21, $P^*(E)$ becomes:

$$P^*(E) = \frac{1}{\Sigma_{t,f}(E)\langle l^* \rangle + 1}. \tag{3.22}$$

In this case the average chord length of the fuel lump $\langle l^* \rangle$ is equal to $\langle l \rangle/(1-C)$. Recalling the definition of the average chord length $4V/S$, considering a constant volume V, the Dancoff factor can be thought as a reduction the surface S of the fuel lump. Another equivalent definition of the Dancoff factor often used in Monte Carlo code is the following:

$$C = \frac{J_i - J}{J_i} \tag{3.23}$$

Where J_i is the number of neutrons entering the fuel lump in an isolated system and J is the number of neutrons entering in the considered fuel lump in a lattice system. It is also important to recall that the Dancoff factor depends only on the geometry of the heterogeneous lattice and mildly on the moderator cross section. Indeed, the carbon moderator cross section can be considered constant in the resonance range.

A rather simple formula for the average chord length, to be used within the Wigner rational approximation 3.17, can be derived if we consider an infinite medium and kernels randomly distributed within it [50]:

$$\langle l \rangle = \frac{4(V_m + V_f)}{S_f}. \tag{3.24}$$

The previous formula works best for low packing fractions. For most of the formulations dealing with infinite medium Dancoff factor calculations for grains, the coating layers are not taken into consideration. Although many attempts have been made to include them as in the so called dual-particle model [53].

If we turn our attention to real finite fuel element, in the past twenty years, many analytical or semi-analytical methods have been proposed in order to calculate Dancoff factors [54] [55]. However, within the present work, it has been decided to focus on just two of them.

3.5.1 Bende's approach

This method allows us to derive the Dancoff factor through an analytical formula depending on the geometry of the fuel element and the graphite total cross section. In this case, the fuel element is depicted as a two-region system and the neutron interactions are expressed through the first-flight and the transmission probabilities derived by Westfall [51].
The calculation starts evaluating the infinite medium case Dancoff factor [48]:

$$C_\infty = \frac{t_{io} t_{oi}}{1 - t_{oo}}. \tag{3.25}$$

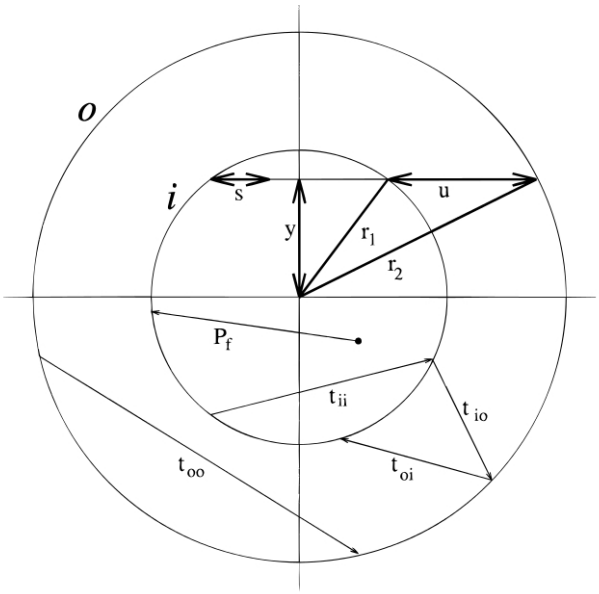

Figure 3.3: Bende's two-region unit cell [48]

Using the same notation as Bende, the probabilities used in equation 3.25 are now defined with the help of figure 3.3:

1. t_{io} is the probability that the neutron leaves the boundary of the first region and reaches without collision the outer boundary of the second region.

2. t_{oi} is the probability that the neutron leaves the boundary of the second region and reaches without collision the outer boundary of the first region.

3. t_{oo} is the probability that the neutron leaves the boundary of the second region and reaches without collision, and without intersecting the first region boundary, the outer boundary of the second region again.

4. t_{ii} is the probability that the neutron leaves the boundary of the first region and reaches without collision, and without passing through the second region, the outer boundary of the first region again.

These probabilities are mathematically expressed as follows:

$$\begin{aligned} t_{io} &= \frac{1}{2(r_1\Sigma_{t,m})^2}\Big[(a+1)e^{-a} - (b+1)e^{-b} + \frac{a^4}{b^2}E_3(b) - a^2E_3(a)\Big] \\ t_{oi} &= \left(\frac{r_1}{r_2}\right)^2 t_{io} \\ t_{oo} &= \frac{1}{2(r_2\Sigma_{t,m})^2}\Big[1 - (1+2a)e^{-2a}\Big] \end{aligned} \tag{3.26}$$

where a and b are equal to $\Sigma_{t,m}\sqrt{r_2^2 - r_1^2}$ and $\Sigma_{t,m}(r_2 - r_1)$ respectively, while r_1 and r_2 are the radii of the first and second region. E_3 is the exponential integral function of the third order and it is evaluated numerically.
For equation 3.25 Janssen derived a rational approximation

$$C_\infty^{fk} = \frac{1}{1 + \Sigma_{t,m}\langle l\rangle}, \tag{3.27}$$

where $\langle l\rangle$ is equal to $\frac{4V_m}{S_f}$ [52]. For some reason, possibly a coincidence, the rational approximation seems to more accurate than the exact formulation [48].
In order to use the Dancoff factor for a finite fuel element cases a second unit needs to be set up.
The same two-region unit cell approach as in figure 3.3 is used to account for the second level of heterogeneity of the system; the first region then represents the fuel region and the second one the outer pebble shell.
In this approach, the calculation is split in two parts: the *intra-pebble* Dancoff factor calculation, dealing with the interactions among the kernels of the same pebble and the *inter-pebble* Dancoff factor calculation dealing with the interactions among kernels of different pebbles. C_{intra} is expressed as:

$$C_{intra} = C_\infty^{fk}[1 - P_{ff}(\Sigma^* R_1)], \tag{3.28}$$

where R_1 is the radius of the first region of the *big* unit cell and Σ^* is a pseudo cross section. P_{ff} is known as first flight collision probability and its expression for spherical geometry was derived by many authors. Here is given the expression

derived by Case, de Hoffmann and Placzek [56]:

$$P_{ff}(\lambda) = \frac{3}{4\lambda}\Big[1 - \frac{1}{2\lambda^2}[1 - (1 + 2\lambda)e^{-2\lambda}]\Big]. \tag{3.29}$$

The product $\Sigma^* R_1$ can be brought in the following simpler form:

$$\Sigma^* R_1 = -\frac{3}{4} ln(t_{oo}) N_{gr}^{1/3}. \tag{3.30}$$

The dependence of the Dancoff factor on the number of grains in the pebble is here shown via the parameter N_{gr}. A similar expression can be derived for the *inter-pebble*

$$C_{inter} = C_{\infty}^{fk} C_{\infty}^{FZ} \frac{P_{ff}(\Sigma^* R_1)[1 - T_{II}]}{1 - T_{II} T_{IO} T_{OI}}. \tag{3.31}$$

The capital letters mean in this case that the probabilities refer to the *big* unit cell and T_{II} is equal to $1 - 4/3(\Sigma^* R_1) P_{ff}(\Sigma^* R_1)$. Although they are calculated with the same formulas, 3.26, the radii and the moderator cross section are expected to be different. Finally summing up the two previous equations we yield:

$$C = C_{\infty}^{fk}\Big[1 - P_{ff}(\Sigma^* R_1) + C_{\infty}^{FZ} \frac{P_{ff}(\Sigma^* R_1)[1 - T_{II}]}{1 - T_{II} T_{IO} T_{OI}}\Big]. \tag{3.32}$$

This method seems to achieve a good level of accuracy as the comparisons shown by Bende can certify and at the same time allows enough flexibility to calculate many typical reactor physics scenarios concerning HTGRs. Furthermore, it has the indisputable advantage, with respect to the more accurate Monte Carlo methods, to practically consume hardly any computational time [48].

3.5.2 Ji's approach

As for the previous case, in this approach the calculation of the Dancoff factor for finite reactor systems is split in two contributions, that are the *intra-pebble* and the *inter-pebble* factors and both are calculated making use of the infinite medium Dancoff factor formulation. Ji, starting from the idea first developed in the 1940s by Dirac [46], bases his whole approach on the chord length distribution concept.

The Dancoff factor for an infinite medium is expressed as [57]:

$$C_\infty = \int f(l) e^{-l/\lambda} dl. \tag{3.33}$$

Where $f(l)$ is the probability density function of the chord length distribution of the moderator, l is the distance between two kernels averaged in every direction and λ is the mean free path in the moderator. Furthermore, according to Ji, the probability density function can be represented as [58]:

$$f(l) = \frac{1}{\langle l \rangle} e^{-l/\langle l \rangle}. \tag{3.34}$$

In this case, the average chord length between two fuel kernels $\langle l \rangle$ is defined as follows:

$$\langle l \rangle = \frac{4r}{3} \frac{1-f}{f}, \tag{3.35}$$

where f represents the ratio of the kernel volume over the total volume.
As previously said, the Dancoff factor calculation is divided in two parts. For the *intra-pebble* Dancoff factor, a similar expression to equation 3.28 is obtained:

$$C_{intra} = C_\infty [1 - P_{ff}(\lambda^*, R_1)]. \tag{3.36}$$

However, the first-flight probability is somewhat different:

$$P_{ff}(\lambda) = \frac{3}{4}\left(\frac{\lambda^*}{R_1}\right) - \frac{3}{4}\left(\frac{\lambda^*}{R_1}\right)^2 e^{-2(R_1/\lambda^*)} + \frac{3}{8}\left(\frac{\lambda^*}{R_1}\right)^3 [1 - e^{-2(R_1/\lambda^*)}] \tag{3.37}$$

and pseudo cross mean free path is here defined as:

$$\frac{1}{\lambda^*} = \frac{1}{\lambda} + \frac{1}{\langle l \rangle}. \tag{3.38}$$

The *inter-pebble* Dancoff factor can be expressed through multiple different probabilities:

$$C_{inter} = P_1 P_2 P_3 \frac{1}{1 - P_2 P_{tr}}, \tag{3.39}$$

with the following definitions [57]:

1. P_1: average probability that a neutron escaping from a fuel lump in a pebble escapes from it without entering another fuel lump or colliding with the moderator.

2. P_2: average probability that a neutron escaping from a pebble enters another pebble without collision.

3. P_{tr}: average probability that a neutron incident on a pebble traverses it without entering any fuel lump or having a collision with the moderator.

4. P_3: average probability that a neutron incident on a pebble enters a fuel lump within the pebble.

Developing further equation 3.39 we arrive to

$$C_{inter} = \frac{P_{ff}\left(\int H(S)e^{-S/\lambda}dS\right)\cdot\left(C^{\infty}\frac{\langle L\rangle}{\lambda^*}P_{ff}\right)}{1-\left(\int H(S)e^{-S/\lambda}dS\right)\cdot\left(1-\frac{\langle L\rangle}{\lambda^*}P_{ff}\right)}. \tag{3.40}$$

Where L is the mean chord length of the pebble, P_2 is equal to $\int H(S)e^{-S/\lambda}dS$ and $H(S)$ is the chord length probability density function between two pebbles considering an infinite pebble bed. If we try to use the same probability density function as in 3.34

$$H(S) = \frac{1}{\langle S\rangle}e^{-S/\langle S\rangle}, \tag{3.41}$$

defining F as the pebble packing fraction and

$$\langle S\rangle = \frac{4R_1(1-F)}{3F} \tag{3.42}$$

we are going to obtain a very poor result. Although this kind of approximation gives excellent results for infinite medium containing micro-spheres, assuming the same exponential law for pebble leads to large errors [58]. The probability P_2 needs to be calculated with more accurate methods, a Monte Carlo code for instance.
The method developed by Ji shows to be more accurate than Bende's one and they are both very fast in comparison to Monte Carlo codes. Ji's also provides formulas for the case of block type reactors where the fuel element has a cylindrical shape.

Although, in this case the P_2 probability is easier to calculate without Monte Carlo codes because this problem for cylindrical fuel rod is widely-known in literature [49]. The need of an ad hoc Monte Carlo code for the P_2 probability calculation in the case of pebble bed reactors, makes the application of this approach more difficult. Finally, Bende's approach was chosen as default method for HCP.

3.6 Thermal disadvantage factor

In ordinary reactor physics calculations, as it will be explained in section 5, it is customary to perform the diffusion calculation in homogenized cells. A simple volume-averaging of the cell materials is often not sufficient in order to preserve the nuclear reaction rates [59]. The so-called disadvantage factors needs to be applied. The average neutron cross section in the cell is defined as:

$$\Sigma^{cell} = \frac{\Sigma^F \phi_F V_F + \Sigma^M \phi_M V_M}{\phi_F V_F + \phi_M V_M} = \frac{\Sigma^F + \Sigma^M (V_M/V_F)\xi}{1 + (V_M/V_F)\xi}. \tag{3.43}$$

Where ξ is the so-called disadvantage factor, defined as:

$$\xi = \frac{\phi_M}{\phi_F}, \tag{3.44}$$

while the ϕ_F and ϕ_M are respectively the neutron flux in the fuel and in the moderator. If the homogenised neutron flux ϕ_{cell} is expressed as:

$$\phi_{cell} = \frac{\phi_F V_F + \phi_M V_M}{V_F + V_M}, \tag{3.45}$$

it can be easily seen, from the following equation, that the reaction rate in the cell is preserved [59].

$$\Sigma^{cell} \phi_{cell} V_{cell} = \Sigma^F \phi_F V_F + \Sigma^M \phi_M V_M. \tag{3.46}$$

In the framework of neutron diffusion theory, the disadvantage factor can defined in terms of two functions E and F [59]:

$$\xi = \frac{V_F \Sigma_a^F}{\phi_M \Sigma_a^M} \left(\frac{V_M \Sigma_a^M}{\phi_F \Sigma_a^F} F + E - 1 \right). \tag{3.47}$$

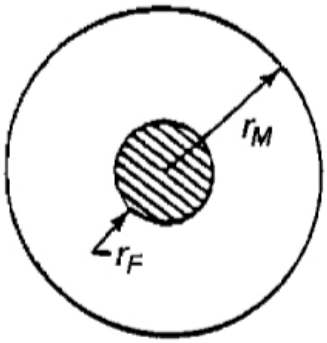

Figure 3.4: Unit cell, spherical geometry [59]

For spherical geometry, as in the case of a pebble bed unit cell, the two functions can be expressed as:

$$\begin{aligned} F &= \frac{(r_F/L_F)^2 tanh(r_F/L_F)}{3((r_F/L_F) - tanh(r_F/L_f))} \\ E &= \frac{r_M^3 - r_F^3}{3r_F L_M^2} \frac{1 - (r_M/L_M)coth((r_M - r_F)/L_M)}{1 - r_M r_F/L_M^2 - ((r_M - r_F)/L_M)coth((r_M - r_F)/L_M)} \end{aligned} \tag{3.48}$$

In this case, L represents the diffusion length and r the radius, as in figure 3.4. Although more sophisticated methods exist, this one proved to be quite successful for graphite moderated reactors [44].

4 HCP framework

The HTR Code Package (HCP) is a code package designed to simulate every relevant aspect of an HTGR core accident scenario in an integrated manner [60, 61]. The code system is able to simulate transients as well as steady-state calculations or a combination of both; allowing at the same time to perform a mesh-wise source term calculation and in the near future also dust production and transport simulations. This is probably one of the most outstanding features of this newly developed code. Furthermore, it is written in C++ in order to exploit the object-oriented capabilities and the latest programming standards. This, in turn, leads to a simplification of the data management and to a simplification of the data exchange among the different modules.

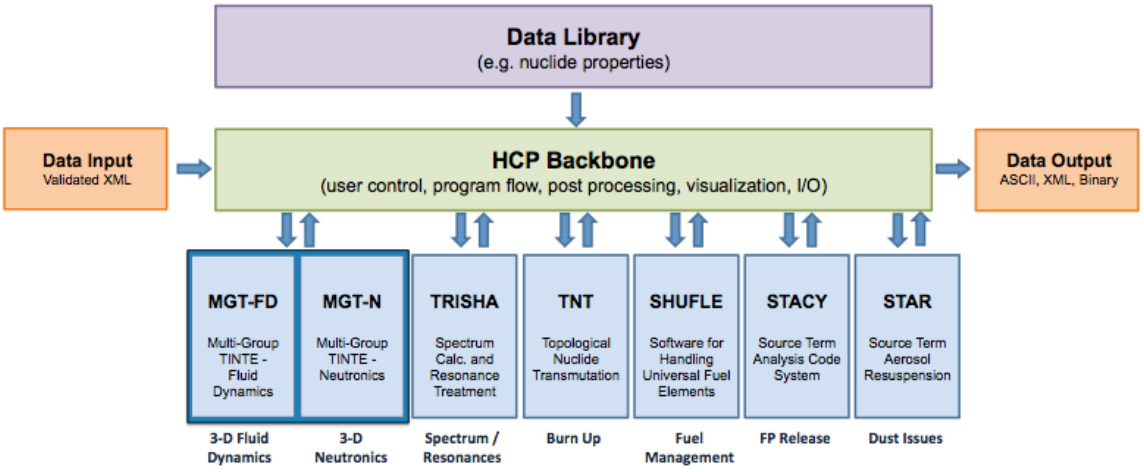

Figure 4.1: Layout of the HTR Code Package (HCP) [61]

The suite can be seen as a collection of different modules, figure 4.1. Every module is in charge of a specific task and each of them exchange data with other modules only through the backbone. For instance, MGT-FD and MGT-N take care of the fluid dynamics and the neutronics calculations. Special emphasis will be put on this code later since large parts of these two modules are derived from MGT-3D. TRISHA is responsible for the neutron spectrum calculations, TNT is the new burn up code base on graph theory [62] and SHUFLE was also developed recently and is in charge of the fuel management of pebbles and blocks [63]. Fission product release calculations are handled by the new code STACY [64] that replaces the old codes: FRESCO-I, FRESCO-II [65] and PANAMA [66] while STAR is responsible for the dust production and transport, it is still loosely coupled with the backbone at the moment.

Such level of integration could be achieved only making use of the newly developed backbone, responsible for the coordination of each module. The backbone makes

also possible an integrated and optimized management of data input and output of the system code.

Additionally, one of the most important goals of the HCP project was to have one consistent input and data library shared by every module, in order to avoid library data mismatch or input duplication.

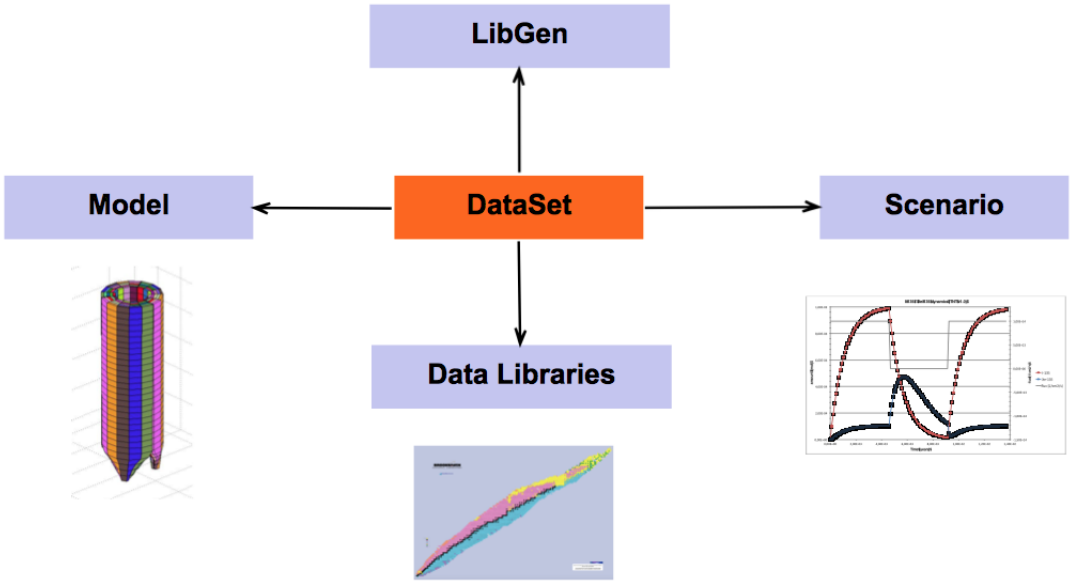

Figure 4.2: HCP input concept

Every input consists of four different files: Model.xml, DataSet.xml, Scenario.xml and LibGen.xml, see fig. 4.2. While Model.xml deals with the geometry and the material definitions of the system under consideration, the Scenario.xml file defines which events the system is going to simulate making use of *Action* statements. The LibGen.xml file, on the other hand, contains directives in order to generate through the library generator an appropriate neutron data library. The DataSet.xml finally links a particular set of Model.xml, Scenario.xml and data library to a distinct simulation case. Therefore, it is possible for instance to re-use model descriptions with different transient scenarios.

The Scenario.xml file consists of settings and a time line. The latter one contains a number of *Action* statements which invoke different HCP modules and control their time dependent behavior. Repeating statements can be defined in an *ActionSet* which acts like a loop. In general, they are used to describe shuffling schemes, accident scenarios and burn-up time steps.

4.1 MGT-FD and MGT-N

As part of the process to integrate MGT-3D in HCP, the neutronic part was decoupled to some extent from the fluid dynamic one. This process resulted in the two HCP modules MGT Fluid Dynamics (MGT-FD) and MGT Neutronics (MGT-N). The two codes were partially rewritten in C++ and refactored according to newer coding standards. Moreover, the so called MGT-3D control part, in charge of the coupling criteria and the transients evolution, was also rewritten in C++ and it is now part of the HCP backbone.

MGT-3D was developed in the early 2000s as a successor of TINTE [29]. The code is able to do 2D/3D steady-state and transient simulations coupled with thermo-fluid dynamics calculations, taking into account the mutual feedback effects.

The main goal of this code was the simulation of accidents, so that the code was well equipped for short transient scenarios but lacked the proper physics in order to simulate long term or operational scenarios. Indeed, in order to simulate an accident happening in nominal reactor condition, the code had to receive the equilibrium core material density distribution, among other things, from VSOP [20]. Although, MGT-3D can deal with the Xe-135 build-up and its neutronic feedback along with other isotopes like Sm-149, Sm-151 and Gd-157, the time span of its accident simulations is limited [29].

Due to the recent coupling in HCP, MGT-3D can now overcome these problems, as HCP is able to calculate an equilibrium core without any external code dependencies making use of the shuffling capabilities provided by SHUFLE.

From the fission power MGT-3D is capable of calculating the heat distribution within the core, dividing the production between local (inside the kernel) and non-local (outside the kernel) making use of an approximated gamma transport subroutine. The decay heat power is accounted for starting from life history information that had to be provided in the input, usually calculated by VSOP. Due to the recent upgrades, the life history can now be updated in HCP every burn-up time step.

A simplified version of the Navier-Stokes equations is applied in order to simulate the gas flow while, as for the neutron diffusion calculation, the gas velocity and temperature fields are determined making use of a leakage iteration method, described later.

Furthermore, the code provides of an external 1-D fluid dynamics network in order to have a lumped parameter representation of the primary circuit. MGT-3D makes use of the gray curtain approach in order to simulate control rods movements, but external control rod cross sections can be provided to achieve better accuracy and they are usually calculated by TOTMOS [34].

Of primary importance, during a steam or air ingress, is the possibility of performing quantitative calculations regarding the graphite corrosion or heat source calculation

related to the Boudouard reaction [67]. This can be, to some extent, accomplished by MGT-3D and was the focus of experimental benchmarks as VELUNA [68], NACOK-I and NACOK-II [69] [70].
The MGT-3D control flow is shown in figure 4.3. As it can be seen the neutronic and the fluid dynamics calculations are solved separately and the overall solution can be found only iteratively.

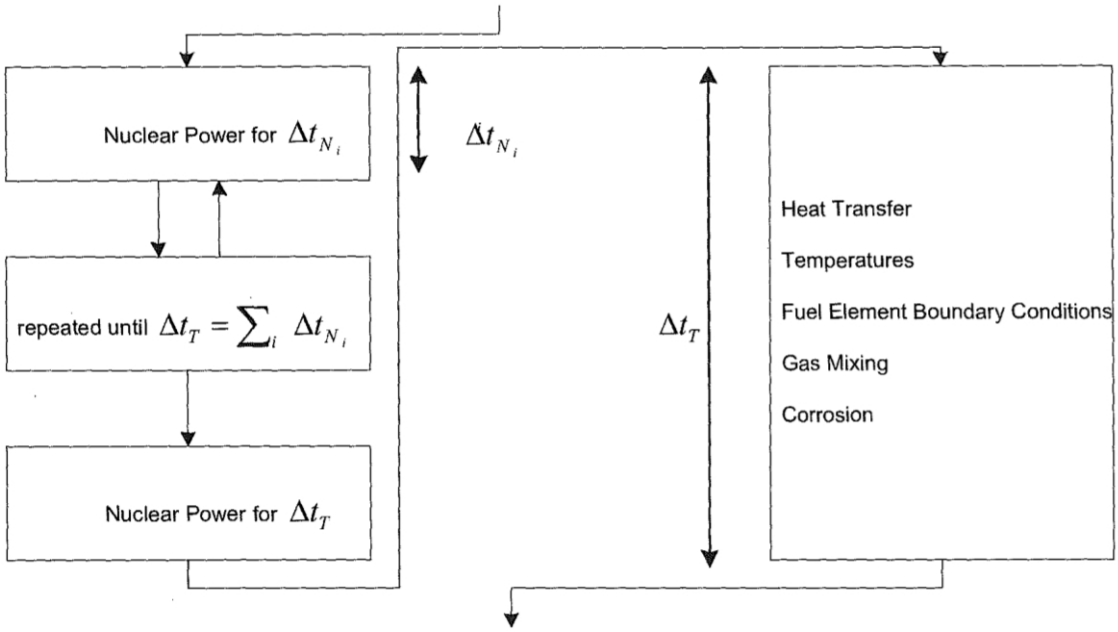

Figure 4.3: MGT control scheme [29]

4.1.1 Fluid dynamics calculation

The complete thermo-fluid dynamics calculation is a formidable task that requires the simultaneous solution of many different interdependent physics aspects. The fluid dynamics calculation is divided in five steps:

1. Determination of the coolant flow path velocities and rates under fixed boundary conditions.

2. Determination of the heat flow from the fuel elements to the gas.

3. Determination of the heat conduction for the solid materials inside the pebble bed.

4. Determination of the convective heat transport, i.e. coolant pebble bed interaction.

5. Determination of the gas mixing and corrosion effects.

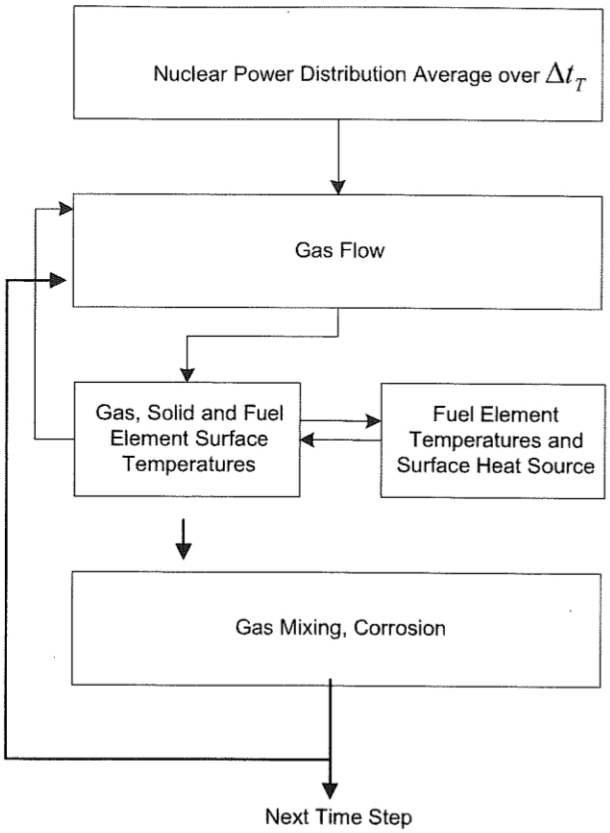

Figure 4.4: MGT-FD Fluid dynamics scheme [29]

Due to the strong coupling between the different sub-problems listed above, the overall solution is obtained iterating among the different sub-solvers. Interdependencies might arise as a result of the gravity influence on the flow path, the flow velocity distribution influence on the heat transfer or the corrosion effects on the temperature distribution [29].

4.1.2 Neutronics calculation

At the beginning of every nuclear calculation, the temperature distribution inside the fuel elements is calculated in order to evaluate the nuclear cross sections for the next steps. This calculation is followed by a neutron flux calculation, where the neutron flux distribution across the reactor is carried out, as it will be explained later, with the leakage iteration method. At the same time the Xe-135 and the other strong absorber concentrations are adjusted in order to account for their influence on the short-term dynamics of the reactor.

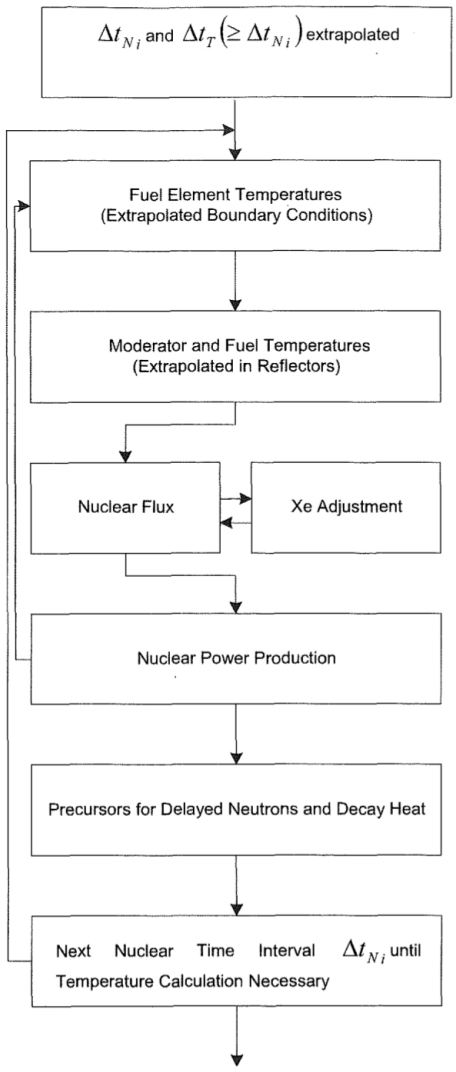

Figure 4.5: MGT-N neutronics scheme [29]

The new heat production is then calculated applying the DIN-25485 [71] and the fuel element temperature calculation together with the nuclear cross sections evaluation have to be repeated until the convergency criteria is met. Furthermore, the precursors for delayed neutrons are calculated using a 24-group structure and the heat decay is added to the fission power. Finally, the total power calculated in the current nuclear time step needs to be within the allowed limit otherwise a smaller time step is chosen and the calculation is repeated until the criteria is met [29].

4.1.3 Leakage iteration method

In a diffusion calculation, the reactor heterogeneities are replaced by homogenized meshes. In order to limit the loss of accuracy the mesh size, Δ, has to be always smaller than the shortest thermal diffusion length, L, inasmuch the error is proportional to

$\left(\frac{\Delta}{L}\right)^2$ [59]. Usually, this leads to an unbearable number of meshes needed, if we only consider the finite difference method, to correctly simulate the behaviour of a large thermal nuclear reactor.

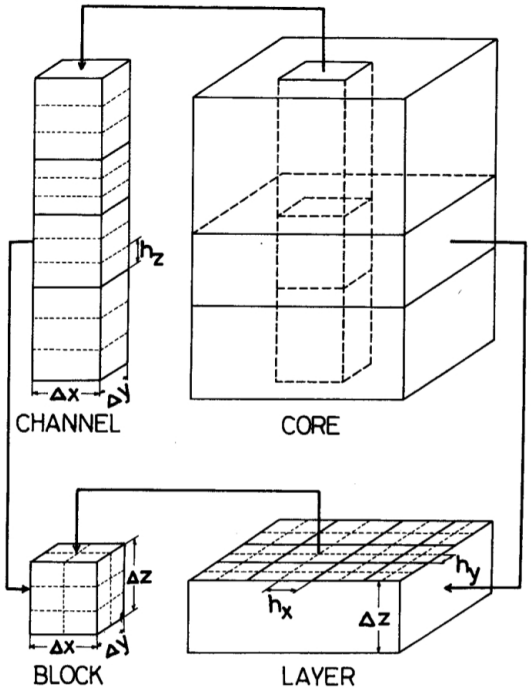

Figure 4.6: Configuration of channels, layers, blocks [72]

Many different approaches have been developed in the past fifty years in order to overcome this problem and reduce the computation burden. Among the most popular ones, there is the flux synthesis method that combines 2D planar neutron flux calculations with 1D axial calculations to obtain, with the appropriate iteration sequence, a 3D neutron flux distribution. Another popular approach is the coarse-mesh method, where the accuracy of the finite difference method is improved using higher order approximations for the neutron flux distribution among the meshes. The last popular method mentioned here is the nodal one; in this case, part of the equation is solved analytically and a general solution is found by applying coupling coefficients among the nodes. The leakage iteration method discussed here, can be seen as member of the class of the flux synthesis methods [72].
As shown in figure 4.6, the reactor is divided in several layers and channels where all the blocks are homogenized beforehand. In order to discuss this method, it is important to start from a simplified version of the diffusion equation, as described in 2.4:

$$\nabla D \nabla \phi - \Sigma_t \phi + \theta = 0. \tag{4.1}$$

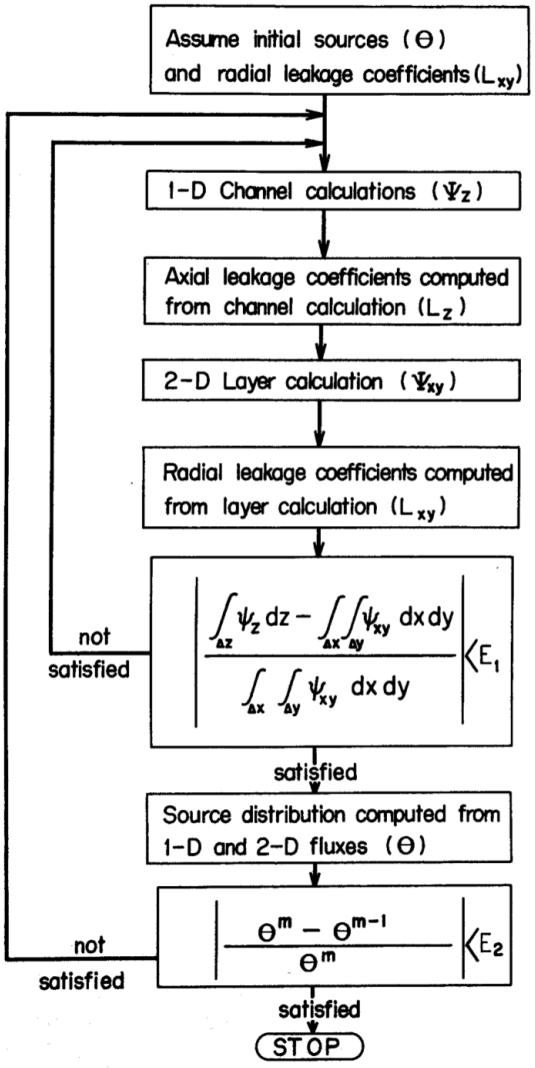

Figure 4.7: Leakage iteration method diagram [72]

Performing planar and axial integrations of the previous equation makes it possible to split the different axial and planar contributions in the following system:

$$\begin{aligned} D\frac{\partial^2\psi_z}{\partial z^2} - (\Sigma_t + L_{xy})\psi_z + \theta_z = 0. \\ D(\frac{\partial^2}{\partial x^2} + \frac{\partial^2}{\partial x^2})\psi_{xy} - (\Sigma_t + L_z)\psi_{xy} + \theta_{xy} = 0. \end{aligned} \tag{4.2}$$

Where θ is the neutron source, L_{xy} is the planar neutron leakage and L_z is the axial leakage. The other variables have the following meaning:

$$\begin{aligned} \psi_z &= \int_{\Delta_x}\int_{\Delta_y} \phi dxdy, \qquad \theta_z = \int_{\Delta_x}\int_{\Delta_y} \theta dxdy, \\ \psi_{xy} &= \int_{\Delta_z} \phi dz, \qquad\qquad \theta_{xy} = \int_{\Delta_z} \theta dz. \end{aligned} \tag{4.3}$$

The inner iteration process, as depicted in figure 4.7, consists in iterating the 2D and the 1D diffusion calculations (system 4.2) in every layer and channel until the neutron flux converges for every block, that is

$$\left| \frac{\int_{\Delta_z} \psi_z dz - \int_{\Delta_x}\int_{\Delta_y} \psi_{xy} dxdy}{\int_{\Delta_z} \psi_z dz} \right| < E_1. \tag{4.4}$$

Then the neutron source distribution and the k_{eff} are recalculated and the process is repeated with the new source distribution until the second criteria is met

$$\left| \frac{\theta^n - \theta^{n-1}}{\theta^n} \right| < E_2. \tag{4.5}$$

It is worth mentioning, and this is true especially for transient calculations, that every new iteration triggers a new mesh-wise spectrum calculation. Because the variation of the neutron leakage, in graphite core reactors, has considerable effects on the cross section generation process, the nuclear cross sections for the whole reactor need to be recalculated at every iteration step. Therefore, it is of the outmost importance to optimize the speed performance of the neutron spectrum code.

4.2 TRISHA

TRISHA (TRansport Integral Spectrum and Homogenization Applications) is a neutron transport spectrum code used in HCP in order to generate neutron energy broad cross sections for the diffusion and the burn-up calculations. It incorporates a 0D MUPO-like diffusion code and a 0D transport one based on B_1 method. The code was written specifically in order to tackle some of the issues that were affecting the old generation of HTGR spectrum codes developed in Forschungszentrum Jülich and it was implemented in order to make use of the HCP data model structures and to comply to the latest coding standards. More will be said in the next chapter as the code is the focus of this thesis.

4.3 TNT

Topological Nuclide Transmutation (TNT) is a newly object-oriented nuclide transmutation code. It makes use of an innovative solver based on graph theory, which exploits the topology of nuclide chains and therefore speeds up the calculation scheme. One of the new features of this code is the possibility to provide problem-wise neutron energy spectra and unit cell information to generate online broad group cross sections for all nuclides and for all burn up time steps. Therefore, instead of choosing between precompiled sets of cross sections for generic reactor designs, the user can provide internal information derived by a spectrum code. Furthermore, the calculation of nuclear power is assessed separately for decay, fission and capture processes. For example, the usual approach of taking average capture Q values for a specific fuel and reactor is not applied in this code. Instead, the newest nuclide vector and distinct Q values for all capture processes available in the data library are used.
Highest priority has been given in implementing a user-friendly code, making use of XML files for the user input, that can be also easily maintained by the developers team [62].

4.4 SHUFLE

With respect to the fuel management within HCP, all aspects are handled by the code SHUFLE (Software for Handling Universal Fuel Elements). The module was designed to handle all kinds of fuel elements, either spherical or block-type ones. The module is able to depict the pebble flow in such a way that both the accuracy as well as calculation time constraints given by a multi-physics code package such as the HCP are successfully met. SHUFLE offers two different fuel management models for pebble bed reactors, the “flow tube model” and the “seepage model”.
In the seepage model fuel pebble movements are depicted using the same mesh grid as being used for fluid dynamics and neutronics. In this case, the fuel shuffling can be seen as a sequence of seepage processes.
The process can be described as follows. While discharging clusters of pebbles from the lower end of the pebble bed, voids are created in the lower part of the core. The volumes of the pebble bed which are located above these previously created voids will be stable for a short period of time. But after some time, the configuration becomes unstable, and pebbles start flowing to refill the newly created voids. The voids then start to gradually move upwards and the seepage process ends as soon as the voids reach the pebble bed’s top surface.
In the so called flow tube model the continuous flowing of pebbles is approximated by displacing the content of larger volumes (nodes) at discrete time points. In order to allow for a simpler box-wise moving, the core is sub-divided in so called flow

channels, where each of these channels is sub-divided in nodes of equal geometrical volume [73].

4.5 STACY

The Source Term Analysis Code System (STACY) is the successor of FRESCO-II, PANAMA and SPATRA codes. The original codes, that already passed verification and validation, have been reversed engineered, modernized and combined to form a consistent code. Due to this process, there is actually no need to repeat the complete V&V work.
After the modernization process ended, all the different solvers have been harmonized and coupled to form one uniform code module STACY which is in line with HCP.
The code is now able to perform full core fission product release calculations under both normal as well as under accident conditions. The fission product release from the spheres due to diffusion and recoil is fully implemented. Furthermore, the transportation of fission products within the coolant, due to convection and diffusion, and the deposition of fission products on graphite surfaces such as fuel elements in colder core zones as well as reflector channels can be treated with a great degree of accuracy [64].

4.6 STAR

The STAR module (Source Term due to Aerosol Re-suspension) was developed with the task of simulating and predicting the dust behavior in the primary circuit of an HTGR reactor during normal operation or depressurization accident scenarios. It contains solvers for dust deposition, surface behavior, resuspension and transport. The deposition is calculated using semi-empirical models for thermophoresis, diffusion, impaction and turbulent deposition, which are the most relevant deposition mechanisms for the non-stagnating volumes of the primary circuit [74].
However, at the present the code is still loosely coupled to the HCP framework and not yet harmonized to the HCP coding standards. Therefore, not yet ready to be used.

4.7 LibGen

The neutron cross section data library generation might be considered as the most important and sensitive step in every reactor physics code calculation. Providing accurate neutron fine energy group cross sections is essential in order to make accurate predictions of the dynamic behavior of HTGRs during transient or accident scenarios. For instance, the neutron doppler effect, which is responsible for the stability of the

reactor, relies directly on the accuracy of the resonance treatment of heavy isotopes like ^{238}U or ^{232}Th.
In sections 3.3 and 3.5 it was shown how an appropriate resonance treatment needs an integral formula, depending only on a few geometrical and nuclear parameters, that can be solved numerically in order to provide the flux-weighted nuclear cross sections.
In this section, it is described how, starting from the ENDF/B-VII.0 raw nuclear data, we obtain, within the HCP framework and through NJOY, suitable nuclear fine-energy group cross sections for the spectral calculation.

4.7.1 NJOY

Based on the user's choices, the library generator writes the appropriate isotope-wise NJOY input files, triggers the calculations, reads the NJOY output files and stores them in the HCP data model.
NJOY can be considered as a collection of modules. Every module has a specific task and a certain order in calling the appropriate one has to be followed during the data library process. The modules exchange data through I/O interface, either binary or ASCII format, generating and reading so called *tapes*.
The process usually starts calling the RECONR module, used to reconstruct the cross section information and the resonance cross sections from the ENDF raw data. It is then followed by the BROADR module, which is task with the broadening the resonances according to user selected temperatures using the kernel broadening method. Successively, THERMR is called in order to assure an accurate treatment of the scattering cross sections in the thermal range according to the method selected; either free gas model or $S(\alpha, \beta)$. Finally, GROUPR is called; this module performs a fine energy group condensation according to the fine energy structure selected and provides the intragroup neutron energy distribution in the resonance range according to the chosen method. As it will be explained later, if the user selects the Bondarenko approach, he has to provide an external weighting spectrum or select one from a list of built-in weighting functions. Another option is to perform a detailed Nordheim integral calculation up to the higher boundary of the resolved resonance range [75]. In the last case, the Bondarenko method is still used for higher energies.
In the following parts of this section it will be described more in depth NJOY's thermal and resonance treatments [76].

4.7.2 Thermal scattering

In a system where leakage or absorption are negligible, the neutrons starting at fission energies are slowed down by collisions with the moderator until their energy reach an equilibrium state with the thermal motion of the moderator nuclei. In

such ideal cases the thermal energy neutron spectrum coincides with a Maxwellian distribution [8]. Although the graphite possesses a very low thermal absorption cross section, in real systems a certain number of neutrons are absorbed in the thermal range and the leakage plays an important role in deviating the real thermal spectrum from a Maxwellian one.
In the case of solid moderators, like graphite, it is important to consider the energy exchange between the neutron and the crystal. The energy corresponding to the vibrational quanta, called phonons, can be exchanged only in discrete amounts. Furthermore, the particular structure of the graphite gives rise to an anisotropic arrangement of the crystals with preferred orientation directions.
All the different methods to treat the thermal scattering of the moderator can be enclosed in the $S(\alpha, \beta)$ formalism. From quantum mechanical analyses we arrive to the following expression for the differential elastic scattering cross section from energy E' to E and from $\mathbf{\Omega}'$ to $\mathbf{\Omega}$:

$$\Sigma_s(E' \to E, \mu_0) = \frac{\Sigma_b}{4\pi kT}\Big(\frac{E}{E'}\Big)^{\frac{1}{2}} e^{-\frac{\beta}{2}} S(\alpha, \beta) \tag{4.6}$$

Where $\mu_0 = \mathbf{\Omega}' \cdot \mathbf{\Omega}$ and α, representing the change in momentum that occurs in the collision, and β, representing the change in energy, have the following definitions:

$$\alpha = \frac{E' + E - 2\mu_0\sqrt{E'E}}{AkT} \qquad \beta = \frac{E - E'}{kT}. \tag{4.7}$$

Σ_b is the so called bound atom cross section, A is the atomic mass, T is the temperature of the medium, k is the Boltzmann's constant and $S(\alpha, \beta)$ is the scattering function that depends in a very complicated way on the dynamics and the structure of the material [59].
The scattering function is usually present in a tabulated form in the raw data library, although they are usually calculated with a NJOY module called LEAPR providing the temperature dependent phonon spectra.
Not every isotope needs such detailed thermal treatment and many important ones, like ^{238}U, can be treated with the so called free gas model. In this case, the moderator is considered as a monoatomic gas whose energy distribution follows the Maxwellian one. The previous treatment can be applied to graphite too if the moderator temperatures are high enough; for high temperature gas reactors at a temperature of 1200 K the chemical binding effect reduces the k_{eff} only up to 0.4 %, with respect to the free gas scattering case [8].
In the case of the free gas scattering model, the scattering function can be expressed as:

$$S(\alpha,\beta) = \frac{1}{2(\pi\alpha)^{1/2}} e^{-\frac{\alpha^2+\beta^2}{4\alpha}} \tag{4.8}$$

and an analytical formula can be obtained for the scattering transfer function $\Sigma_s(E' \rightarrow E)$.

4.7.3 Resonance treatment

In NJOY, the standard method to calculate the intra-group energy spectrum is the Bondarenko one [77]. This method seems to provide rather accurate cross sections, with the exception of resonances in the epithermal range, considering how the self-shielding effect is in general a complicated function of the geometry and composition of the lattice. This method, making use of the B_n transport method and the narrow resonance approximation, describes the energy spectrum as inversely proportional to the total macroscopic cross section

$$\Psi_l^i(E) = \frac{C(E)}{(\sigma_t^i(E) + \sigma_0^i)^{l+1}}. \tag{4.9}$$

In this case $\sigma_t^i(E)$ is the total microscopic cross section, σ_0^i is the background cross section, the indexes i and l represent respectively the isotope and Legendre order and $C(E)$ is the weighting function that has to be chosen among the built-in ones or provided from an external calculation.

When the background cross section is dominant with respect to the total cross section, the resonant material approaches the case of infinite dilution and the resonance does not perturb the asymptotic energy distribution. Conversely, if the total cross section value is higher than the background cross section one, the energy spectrum will be perturbed in proximity of the resonance peak and the resonance will be shielded.

As previously outlined, the Bondarenko method fails in treating with the appropriate accuracy the resonances in the epithermal range. In this range, the resonances cannot be approximated as narrow anymore and the flux shape needs to be calculated with the Nordheim resonance integral method.

The starting point of this method is equation 3.12, shown here:

$$\Sigma_{t,0}(E)\phi_0(E) = (1-P_0)\left[\frac{1}{1-\alpha_0}\int_E^{E/\alpha_0}\phi_0(E)\Sigma_{s,0}\phi_0(E')\frac{dE'}{E'} + \frac{1}{1-\alpha_{m,0}}\int_E^{E/\alpha_{m,0}}\phi_0(E)\Sigma_{sm,0}\phi_0(E')\frac{dE'}{E'}\right] + \frac{P_0\Sigma_{t,0}}{1-\alpha_1}\int_E^{E/\alpha_1}\phi_1(E)\Sigma_{s,1}\phi_1(E')\frac{dE'}{E'}. \tag{4.10}$$

The previous formula is simplified expressing the first-flight collision probability as a function of the escape cross section and incorporating the latter one in the background cross section as in 3.4.
However, a different way is followed in NJOY in order to approximate the moderator flux in equation 4.10. Instead of expressing it as proportional to $1/E$, it is expressed as a function of the fuel flux and a new parameter, β, called heterogeneity parameter:

$$\phi_1(E) = (1-\beta)C(E) + \beta\phi_0(E). \tag{4.11}$$

Where β is defined as

$$\beta = \frac{V_0\sigma_e}{V_1\Sigma_{t,1}} \tag{4.12}$$

These approximations result in simpler expression of the Nordheim resonance integral equation:

$$[\sigma_{t,0}(E)+\sigma_0]\phi_0(E) = (1-\beta)C(E)\sigma_0 + \int_E^{E/\alpha_0}\frac{\beta\sigma_0}{(1-\alpha_0)E'}\phi_0(E')dE' + \int_E^{E/\alpha_1}\frac{\sigma_{sm,0}}{(1-\alpha_1)E'}\phi_0(E')dE'. \tag{4.13}$$

The previous expression depends only on two parameters: the background cross section and β. Although the latter one depends on the particular design of the system under consideration, it is not difficult to calculate it in advance. The expression 4.13 is then discretized in a desired number of energy bins and solved numerically. Finally, the spectrum energy distribution will be used for the condensation of the fine energy group cross sections.

5 Implementation of the new spectrum code

As previously stated, TRISHA is the new HCP neutron transport spectrum code and it includes two solvers. It makes use of a 0D MUPO-like diffusion code and a 0D transport solver. The latter one, in some case, offers a more accurate way to account for the the neutron leakage effect on the fine energy neutron spectrum.
In this section, it will be shown how the two solvers work in more details, underlining how the mathematical models, described in the previous chapter 4, were designed and implemented.

5.1 Coupling to MGT-N

The first step towards the integration of the new spectrum code in HCP was the coupling to MGT-N. This step actually follows the decoupling of MGT-FD and MGT-N from MGT-3D whose details can be in found in [78]. The spectrum code calls present in the diffusion code had to be changed in order to allow the use of the new spectrum code. Initially two calls were implemented in two different loops. As part of the refactoring work done on MGT-3D, the number of calls was reduced to one; now the only one is actually located inside the main neutronic calculation loop, specifically in the subroutine **tinukl**, figure 5.1.
Inside this loop, the spectrum is called as many times as needed in order to achieve the convergency of the leakage method either in steady-state or transient mode. In order to couple the new spectrum code, part of the neutronics of MGT-N had to be rewritten in C++. This was done, mainly to be able to call the new spectrum code from the backbone where the MGT-N control methods are now located. Additionally, it was done in order to comply to the HCP coding guidelines [79] [80].
The subroutines **tinkns** and **tinukl** were revisited for the sake of clarity and to eliminate deprecated FORTRAN features such as gotos and block declarations. Additional effort was put in order to make important features such as the MGT-N Xe-135 dynamics available in HCP.
The coupling was attained replacing TISPEC calls with TRISHA ones and making sure the spectrum code input and output parameter lists still perfectly matched.
The MGT-N spectrum code, whatever it is, take as parameters, from the input files or the MGT-N interface, the moderator and fuel temperature, the homogenized material densities and the buckling values accounting for the neutron leakage.
Of course, now all these data are going through the backbone and it is up to the user whether to store them for further analysis or not. As output, we have the so-called *groups constants*, that are: the broad spectrum weighted cross sections, the broad spectrum weighted inverse velocities and the broad spectrum weighted energy distribution of the fission neutrons.

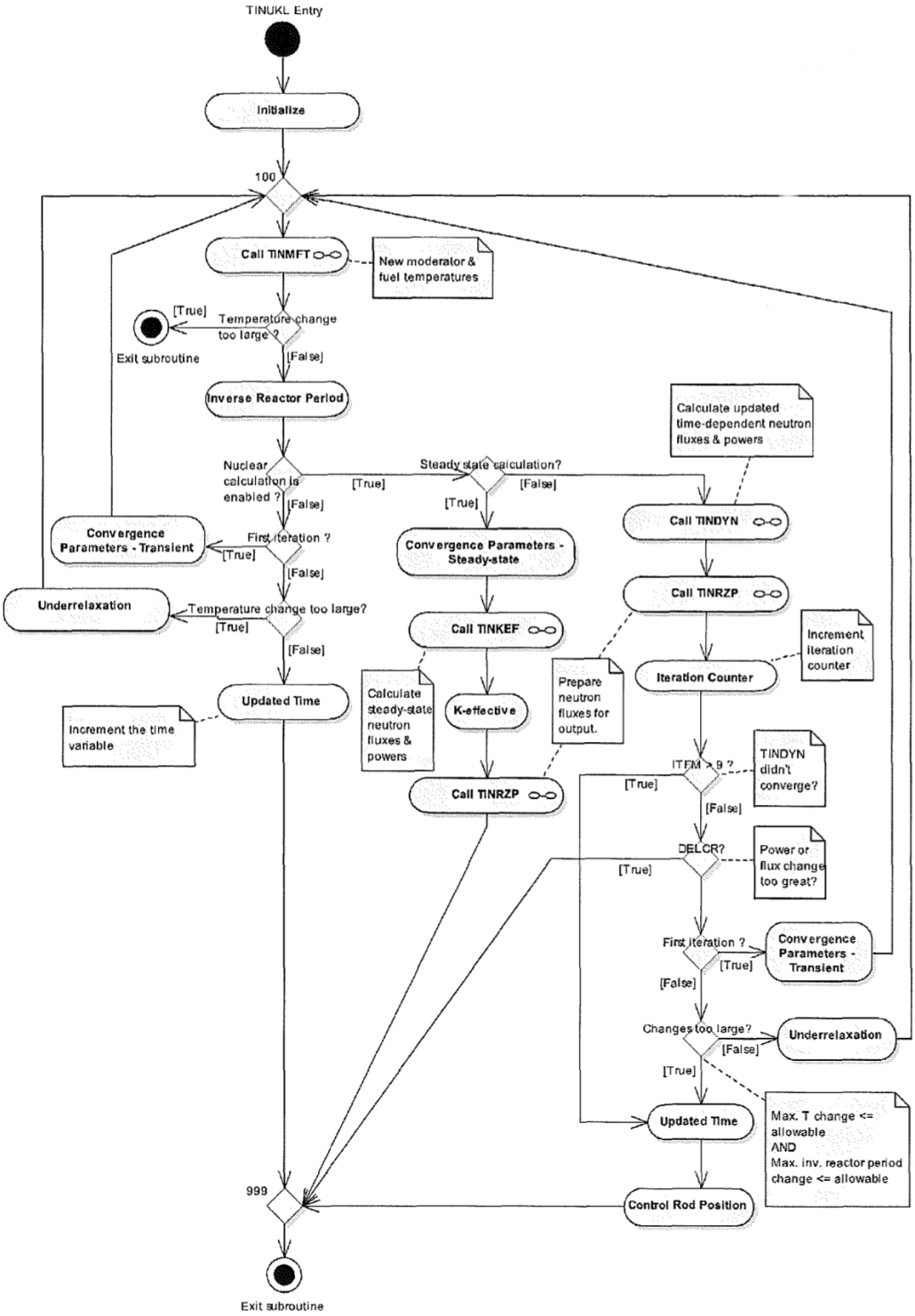

Figure 5.1: MGT-N **tinukl** subroutine diagram

5.2 Software implementation

A general flow diagram is presented in this section in order to understand the fundamental scheme of a generic spectrum code calculation, see fig. 5.2.

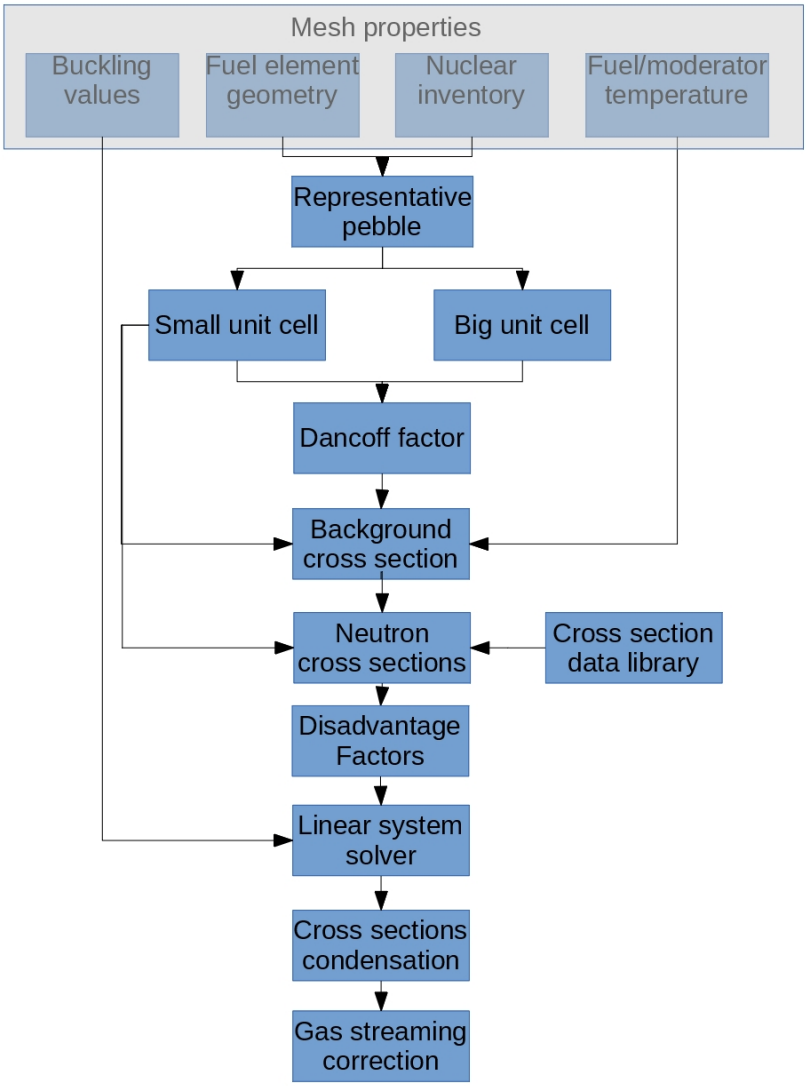

Figure 5.2: General flow chart of the spectrum code calculation scheme

Before starting with the description of such scheme, it is useful to say something about the connections among the different grids needed from the different modules of HCP. The "meshgrid" is used by the diffusion code MGT-N and incidentally by the fluid dynamics code MGT-FD; it is usually a 2D/3D cylindrical regular grid. The spectrum code performs all its calculation mesh-wise, since TRISHA has to provide cross sections based on the output parameters coming from the diffusion calculation. The node-grid is instead used by the SHUFLE flow tube model, where the movement

of the pebbles is approximated by time discrete movements of the batches contained in the nodes. The core is subdivided in flow channels and each of these channels is further subdivided in nodes of equal volumes as in figure 5.3. However, each node is composed of different batches to account for the different number of core passes and burn-up levels [73].

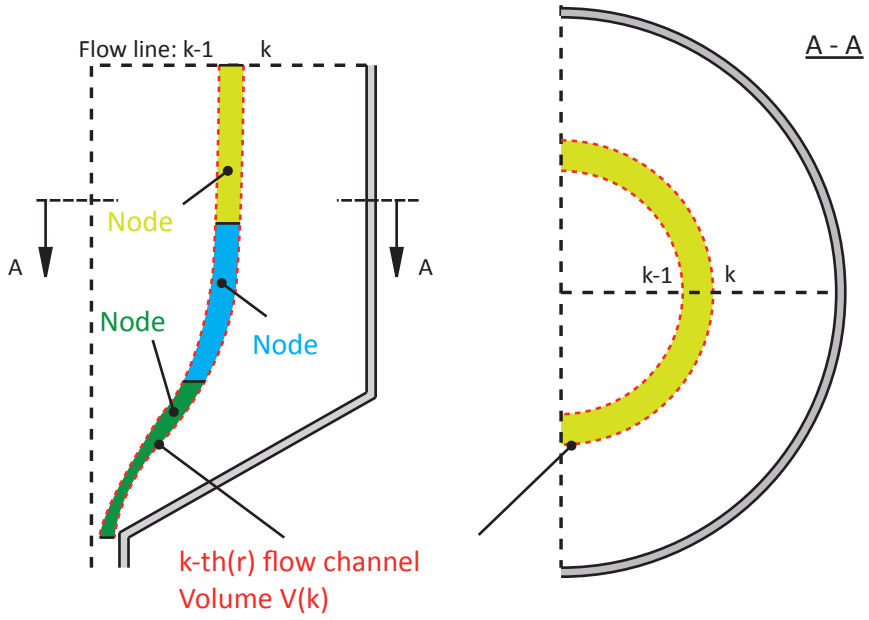

Figure 5.3: Node discretization of a pebble bed reactor [73]

The calculation starts with the definition of a representative pebble for the current mesh. This is carried out averaging the nuclide densities of the pebbles belonging to all the batches that overlap partially or totally with the considered mesh, as shown in figure 5.4.
In the case of a mesh that partially belongs to the pebble bed and to the reflector, as in the cone area, the graphite from the reflector will be treated as it were belonging to some fictitious dummy pebbles and therefore considered as moderator media within the pebble bed.
In the **UnitCell** class a *small* unit cell and a *big* one are set up. The *small* one is defined as the representative coated particle of the pebble surrounded by a layer of matrix graphite, as it can be seen from figure 5.5. The radius of the last layer is calculated by dividing the matrix graphite volume by the number of coated particles in the representative pebble.
The *big* unit cell consists of the homogenized fuel zone, the outer pebble shell and the gas shell. These unit cell definitions allow the spectrum code to be efficient and flexible, since all kind of parameters and nuclear inventories, needed for either 0D or

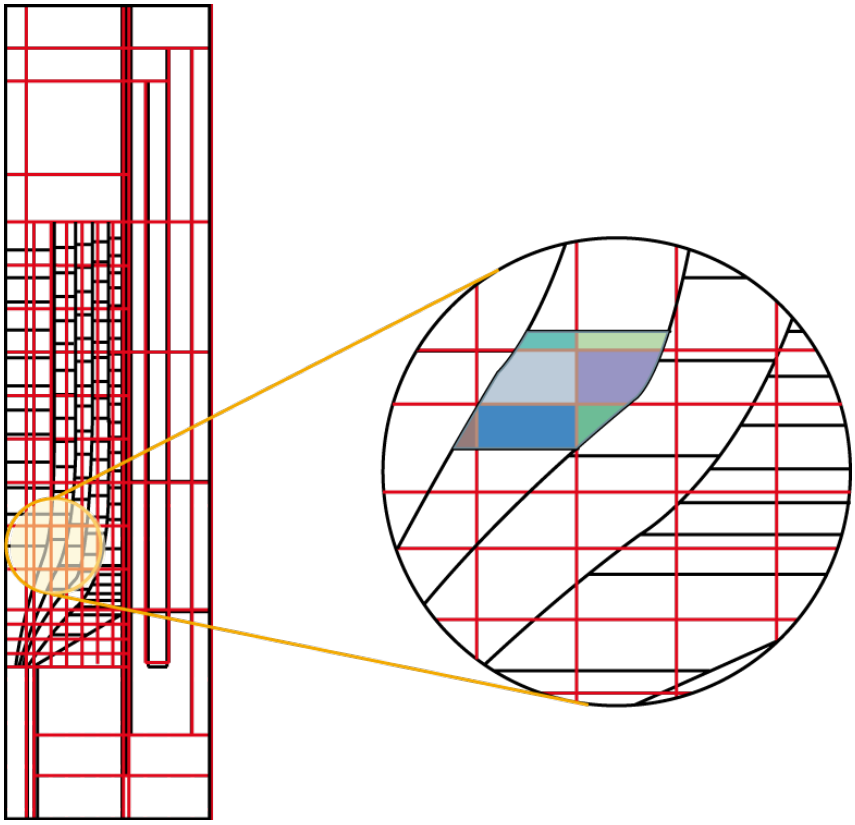

Figure 5.4: grids used in HCP [73]. The meshgrid is in red while the node-grid is in black

1D calculations, can be derived from them.

In addition, while in codes like VSOP, the unit cells for the spectrum calculations had to be set up in the input, this is not necessary in HCP, where the process is fully automatized. The unit cells are set up at every spectrum calculation based on the information stored in the mesh object. This, in turn, leads to a great simplification of the input for the user and to a high level of accuracy.

These benefits become evident in case of shuffling of a fresh core or during a water ingress accident scenario, when the unit cell can change dramatically over time.

The next important step is the background cross section calculation; that is necessary in order to select, together with the fuel temperature, the right nuclear cross sections from the 2-D tables generated by NJOY.

As it was shown in 3.4, the background cross section σ_0 can be calculated with the following equation:

$$\sigma_{0,i} = \frac{\sum\limits_{k \neq i} N_k \sigma_{p,k}}{N_i} + \sigma_{e,i}. \tag{5.1}$$

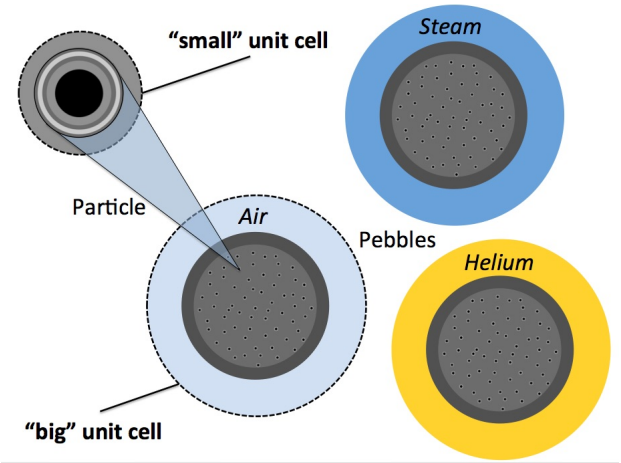

Figure 5.5: Unit cell definitions

With respect to the escape probability σ_e, the Wigner rational approximation is considered nowadays rather inaccurate [9] and a different formulation is currently used in TRISHA

$$\sigma_{e,i} = \frac{1}{N_i \langle l \rangle (b + \frac{C}{1-C})}. \tag{5.2}$$

Where b is the inverse Lavine factor and C is the Dancoff factor. As described in [41], the inverse Levine factor is derived empirically based on more accurate Nordheim and Monte Carlo calculations (see figure 5.6).

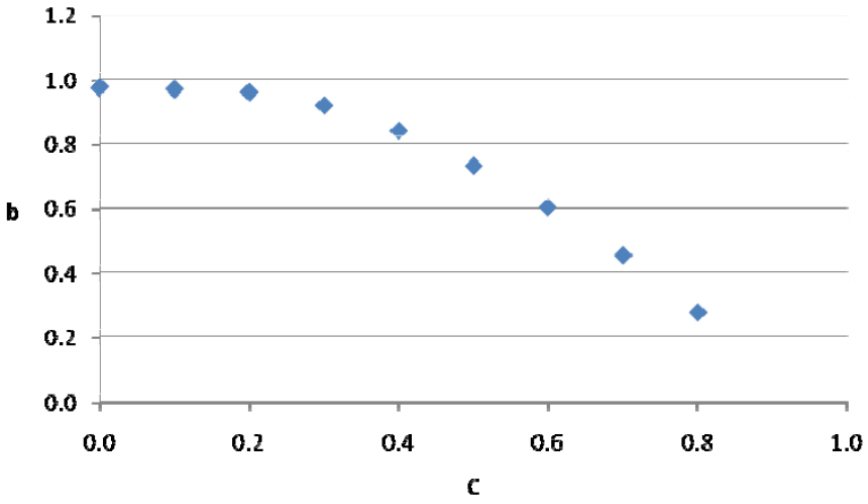

Figure 5.6: Inverse Levine factor curve [41]

Two different formulations for the Dancoff calculations are implemented in TRISHA as discussed in 3.5.

The next step is then the calculation of the thermal disadvantage factors, that are applied for every fine-energy group in the thermal range, as described in 3.6.
Once the nuclear reactor cross sections are obtained, the energy flux distribution can be calculated by solving numerically a linear system. Different schemes are used to obtain the neutron energy spectrum according to the selected method. In the next pages they are both depicted starting from the 0D diffusion method.

5.2.1 0D diffusion solver

In order to solve the linear system, an iterative scheme, that makes use of the power iteration approach, is applied [33]. The generalized eigenvalue problem can be written as follows:

$$\boldsymbol{M}\phi = \frac{1}{k}\boldsymbol{S}\phi. \tag{5.3}$$

Where $\boldsymbol{M}$ is the so called multiplying matrix, whose coefficients are defined as:

$$M_{gg'} = \Sigma_t^g + \delta_{gg'}\Sigma_s^g - \Sigma_s^{gg'}, \tag{5.4}$$

where $\Sigma_s^{gg'}$ represents the scattering cross section from group g to group g', $\delta_{gg'}$ is the kronecker delta and $\boldsymbol{S}$ is the fission-source matrix:

$$S_{gg'} = \chi^g \nu^g \Sigma_f^{g'}. \tag{5.5}$$

All these group constant parameters and scattering matrix coefficients are averaged within the group energy range g and from g to g' respectively.
The iteration, see figure 5.7, starts guessing the source term $S^{(0)}$ and the first $k^{(0)}$. The right-hand side of the linear system 5.3 is now known and the system can be solved using the Gauss-Seidel method [33]. Using the updated fluxes, a new source term and k-effective are evaluated and the loop continues until the exit conditions are met.
The linear system calculation can be decomposed in two parts: the matrix triangularization and the triangular system solution whose computational complexities are respectively $\Theta(\frac{n^3}{3})$ and $\Theta(n^2)$. Noting that during outer iterations the matrix $\boldsymbol{M}$ never changes, the computational complexity of the overall process can be decreased from $\Theta(p\frac{n^3}{3})$ to $\Theta(\frac{n^3}{3} + pn^2)$ performing the triangularization of the matrix $\boldsymbol{M}$ only once before the iteration process starts. In this case p is the number of iteration

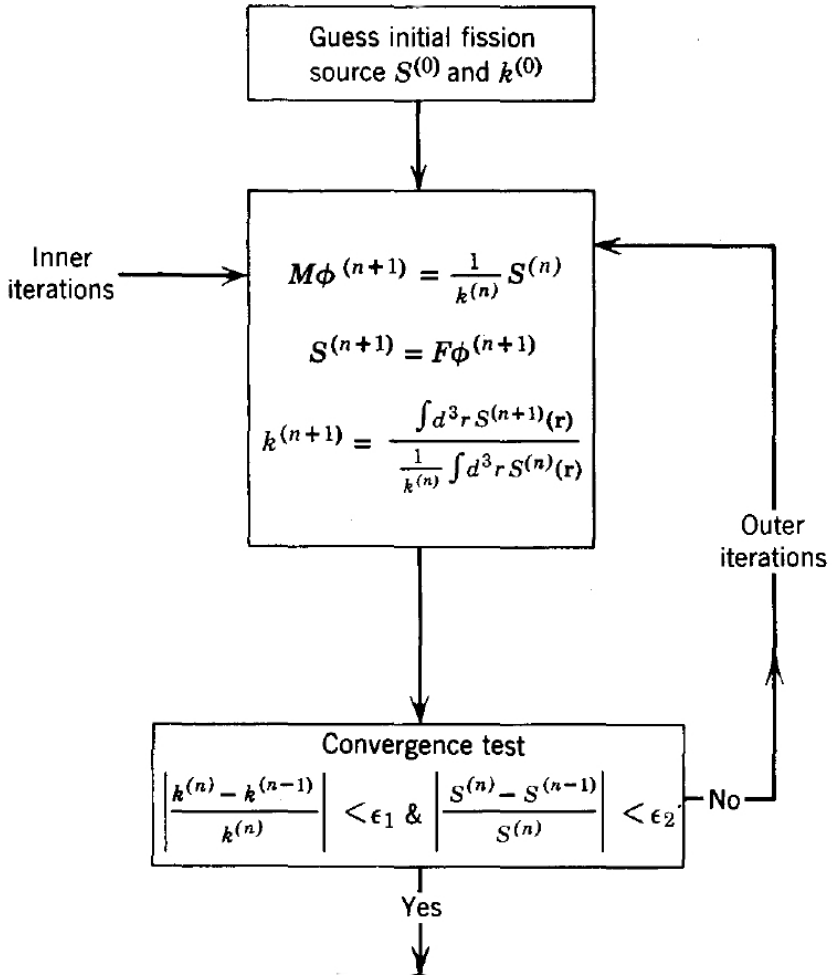

Figure 5.7: Power method scheme [14]

needed to achieve convergency [33].

5.2.2 0D B_1 transport solver

The 0D transport method implementation starts with the evaluation of the α parameter, as described in 2.5. The system is then brought to the following form:

$$\begin{aligned} \pm iBJ(E) &= B^2 \boldsymbol{D}\psi \\ \boldsymbol{A}\psi &= \chi \end{aligned} \tag{5.6}$$

where

$$A_{gg'} = \Sigma_t^g \delta_{gg'} - \Sigma_{s0}^{gg'} + B^2 D_{gg'} \tag{5.7}$$

and the $\boldsymbol{D}$ elements are evaluated inverting the following matrix

$$D_{gg'}^{-1} = 3\alpha_g \Sigma_t^g \delta_{gg'} - 3\Sigma_{s1}^{gg'}. \tag{5.8}$$

Once the $\boldsymbol{D}$ elements are calculated, they are inserted in 5.7 and the system 5.6 is solved making use of the Gauss-Seidel method. As last step, the k-eff is calculated applying the following formula:

$$k = \sum_g \nu^g \Sigma_f^g \psi^g. \tag{5.9}$$

No outer iterations on the fission source or the k-eff are needed within this method since it is a fixed source calculation [39].
These calculations are then followed by the neutron cross sections condensation according to the broad energy group structure chosen by the user, and finally the neutron streaming correction factors are applied to the diffusion constants.
More details with respect to the software implementation can be found in TRISHA developer guide [82].

5.3 Neutron streaming correction

Due to the low neutron absorption of the helium nuclei and due to its low density as a coolant in high temperature gas reactors, the effect of the coolant gas surrounding the pebbles in the core has a negligible effect on k_∞. But its effect on the k_{eff} cannot be discarded if we consider that the increase of the mean free path of the neutrons in the system, due to the void regions, can have a great influence on the neutron leakage, especially in diffusive reactors such as graphite moderated reactors. This effect is taken into account applying a correction factor to the diffusion constants.
Currently, three different methods are implemented in TRISHA in order to cope with this issue. For back compatibility purpose, the MGT-3D way is part of the user options [81]:

$$\bar{D} = D_H + \frac{2}{3}\frac{\gamma^2}{1+\gamma}\left(1 + \frac{1}{8}\left(\frac{1}{2+\gamma}\right)^2\right). \tag{5.10}$$

Furthermore, Behrens and Lieberoth approaches are implemented too [83] [84]; the only difference between the two of them, lies on how they express the geometrical factor. Both methods start from the same formula:

$$\frac{\bar{D}}{D_H} = 1 + \frac{\gamma^2}{(1+\gamma)^2}\left[\frac{2}{3}Q\Sigma_t R + \frac{\frac{4}{3}R\Sigma_t}{e^{\frac{4}{3}R\Sigma_t} - 1} - 1\right]. \tag{5.11}$$

Where $\bar{D}$ is the modified diffusion constant, D_H is the homogenized diffusion constants, γ is the ratio between the void and the material volumes of the mesh, Q is a geometrical factor, Σ_t is the macroscopic total cross section and R is the radius of the pebble. The different formulas regarding the geometrical factors are expressed as follows:

$$\begin{aligned} Q &= 1 + \frac{1}{8\gamma^2} \\ Q &= 1.956 + \frac{1}{260\gamma^2}. \end{aligned} \tag{5.12}$$

The first formula was developed by Behrens and comes from an analytical analysis while the second one was found by Lieberoth as a result of an experimental campaign.

6 Results and discussion

In order to assess the accuracy of the new spectrum code, a series of benchmarks were performed. The code was actually developed in parallel with the results of those benchmarks. Following this approach, the benchmarks shown here, resemble the increase in difficulty either from the physics or from the technical point of view that marked TRISHA code development, see figure 6.4.
However, as described in 5.1, MGT-3D was partially rewritten and refactored in C++ and became MGT-N. It was therefore important to verify that the two code still provide the same results and level of accuracy, this is shown in 6.1. The Monte Carlo code Serpent was chosen as a reference code for the benchmarks, due to its unique modelling capabilities in treating reactor physics HTGR problems [85].

6.1 MGT-N / MGT-3D comparison

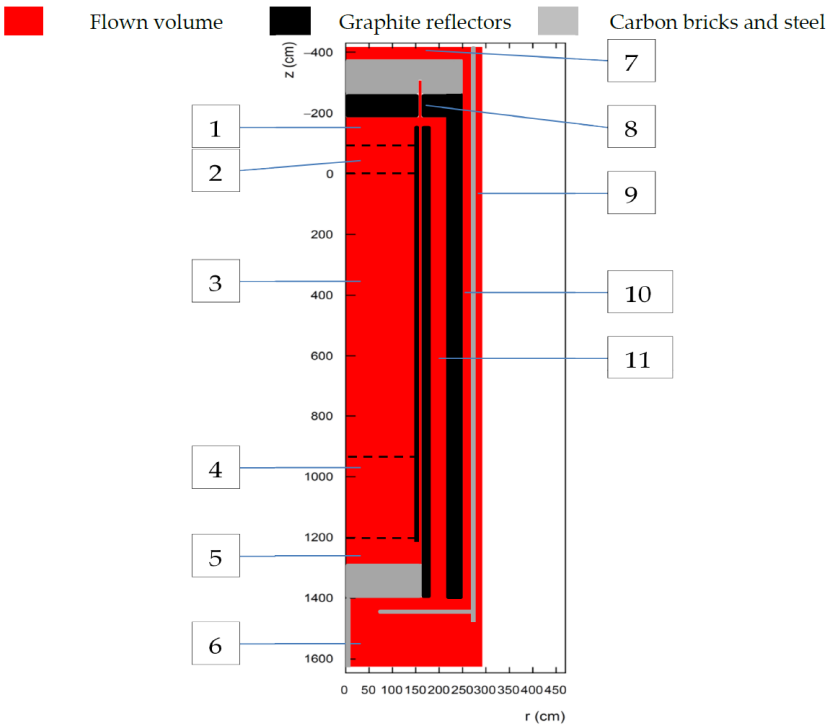

Figure 6.1: Simplified HTR-Modul-200 model. 1: top reflector, 2: core cavity, 3: pebble bed, 4: bottom reflector, 5: hot gas plenum, 6: bottom gas plenum, 7: upper gas plenum, 8: control rods, 9: outer cold gas pipes, 10: depressurization pipe, 11: side reflector. [78]

The aim of this comparison is to prove that the C++ re-implementation of some of the MGT-3D subroutines in the HCP backbone and the refactoring of a large part of the MGT-3D Fortran subroutines, that is MGT-N, did not alter the underlying

physics of the code. The overall intent was to have the two codes to agree within the pre-defined precision.
The model chosen for the benchmark is a simplified version of the HTR-Modul-200; a full description of the physical system can be found in 6.8. In this model, the pebble bed is depicted as a cylinder of 150 cm, without a cone area in the radial direction and 943.14 cm in the axial direction. As it is usually done, the pebble bed is modelled as a homogeneous medium with a filling factor of 0.61. The pebble bed is surrounded by graphite reflectors along with carbon bricks and steel structures as shown in Figure 6.1.

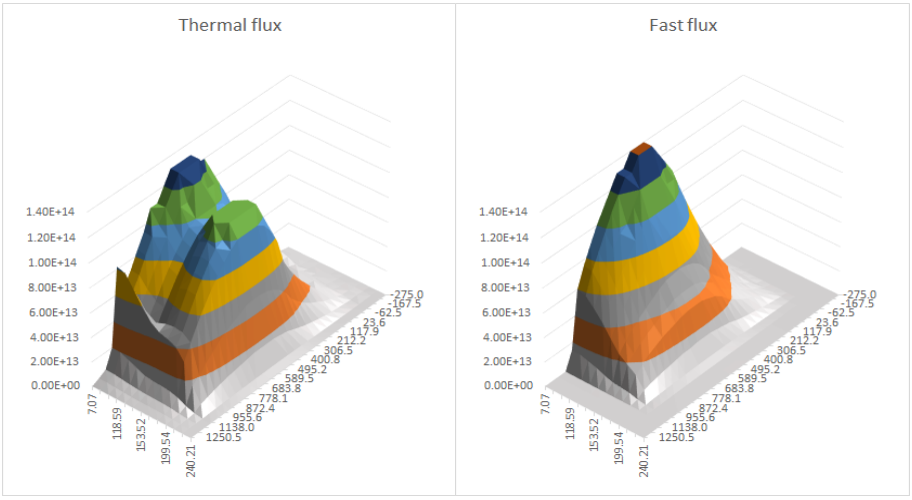

(a) *Neutron thermal flux* $[n/(cm^2 \cdot s)]$ (b) *Neutron fast flux* $[n/(cm^2 \cdot s)]$

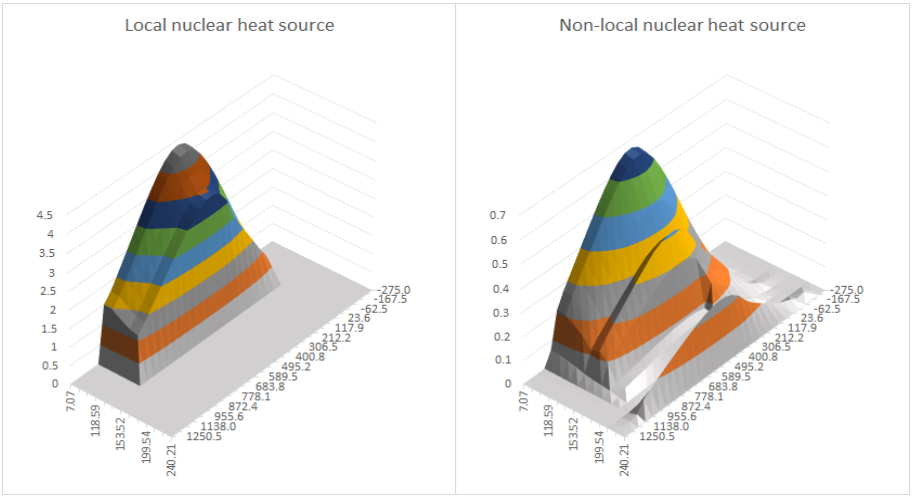

(c) *Local nuclear heat source 2D field* $[W/cm^3]$ (d) *Non-local nuclear heat source 2D field* $[W/cm^3]$

Figure 6.2: HTR-Modul-200 2D fields, with radial and axial axes $[cm]$

Control rods are taken into account using specific nuclide concentrations, according to the equivalent boron concentration method; however, this specific model does not

allow for control rod movements. Although, this model was initially derived to allow fully coupled accident simulations, due to the nature of this specific benchmark, we will focus on a (neutronics only) criticality calculation.

Furthermore, it is worth noting that this model was built following the chain of tools described in 1.5. Additionally, in order to have a fair comparison, the old spectrum code TISPEC was used in HCP as well.

In figure 6.2 typical 2D fields from the HCP criticality calculation are shown. In MGT-3D, and consequently in MGT-N, the fission power is distinguished between local and non-local power. While the local power contains the fission fragments, the alpha and beta contributions, the non-local part is essentially made of the gamma contribution. Furthermore, in all the plots presented here, the "MGT-3D" convention is followed, that is the z axis points at the bottom of the reactor and its origin starts at the boundary between the pebble bed and the upper reactor cavity.

For practical purposes, the comparisons between MGT-3D and MGT-N presented in figure 6.3, are depicted as axial cuts of the 2D fields. All cuts are taken in proximity of the centre of the reactor.

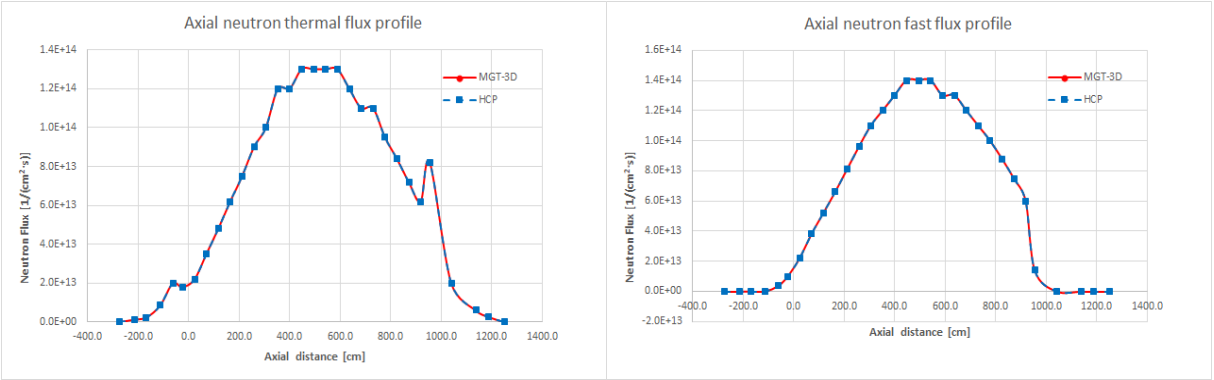

(a) *Axial neutron thermal flux profile* (b) *Axial neutron fast flux profile*

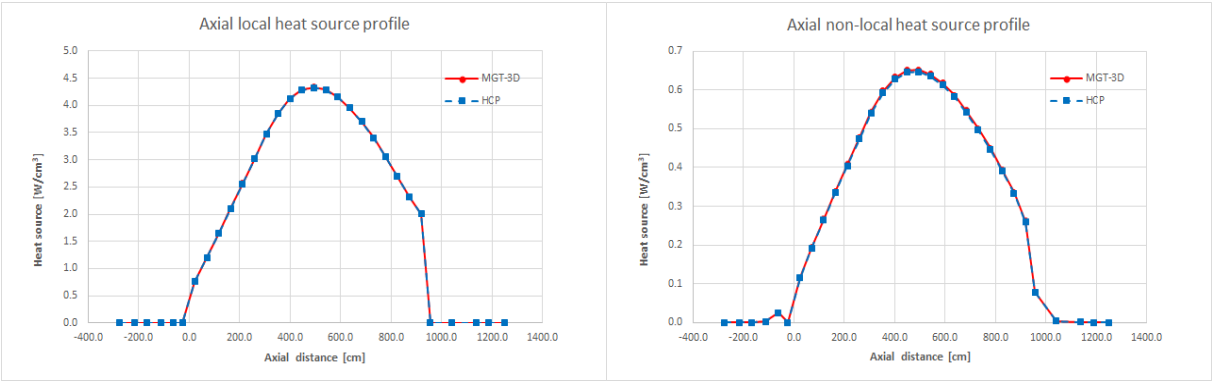

(c) *Axial local nuclear heat source profile* (d) *Axial non-local nuclear heat source profile*

Figure 6.3: MGT-3D / MGT-N comparisons

As it can be seen, the comparisons show a perfect match among the codes, the curves exactly lie on top of each other. This, in turn, proves the reliability of the integration of MGT-3D within the HCP framework as far as neutronics goes. Further benchmarks, with respect to this topic, concerning the fluid dynamics side, can be found in [78].

6.2 V&V approach

As mentioned, the code was built and tested step by step, in order to assess its accuracy and correct potential bugs or errors in the physics models. Extensive effort was put in the generation and the benchmarking of the neutron cross section data libraries; so that the good results achieved in the following benchmarks reflect the level of accuracy reached in the cross-section library generation process.

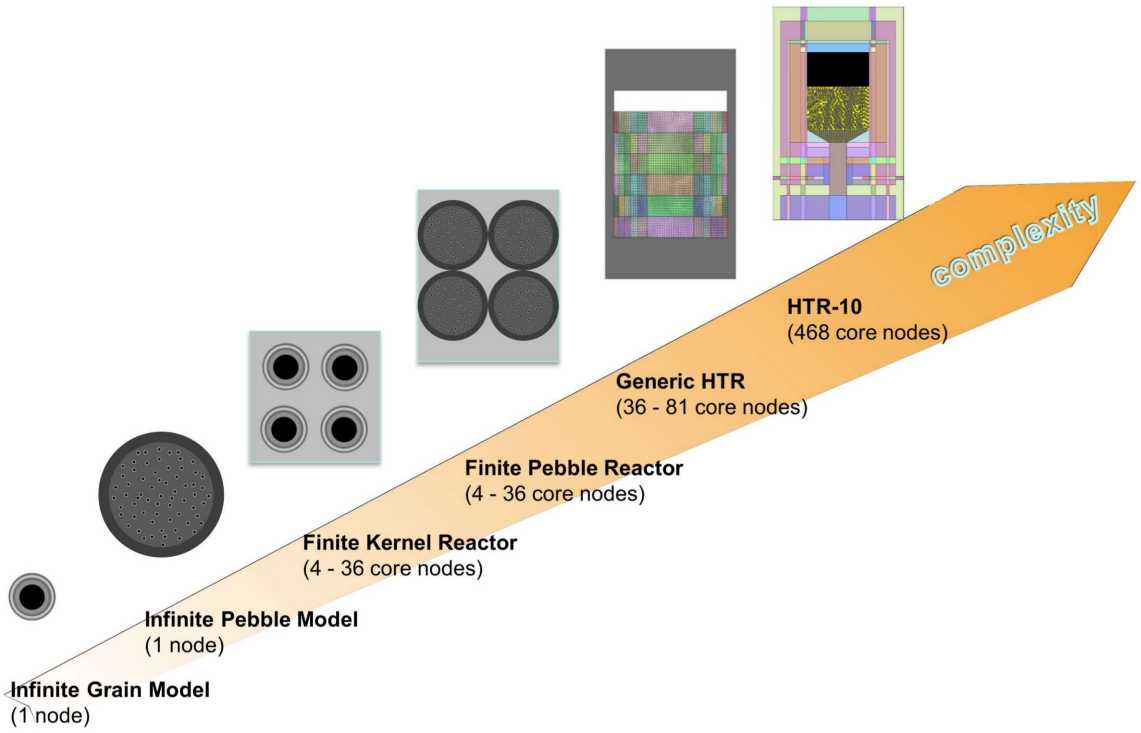

Figure 6.4: V & V milestones

All the libraries are generated starting from ENDF-B/VII.0 raw data, five temperatures and twenty one background cross sections. The later ones are usually interpolated, with appropriate laws, for intermediate values. While the weighting spectra used for NJOY [75] run, as specified earlier, are often generated with an ad hoc Serpent calculation, taking into account the specific characteristics of fuel, temperatures and burnup level.
Many of these benchmarks were carried out, taking into consideration different kind

of fuels: specifically, PBMR, HTR-Modul-200 and HTR-10. This was done to test the code with different level of enrichments, different number of coated particles and different heavy metal contents. The data concerning the fuel characteristics can be found in appendix A.1.
In order to test the influence of the neutron leakage on the energy spectrum delivered by TRISHA, the code was also tested with finite reactor systems like HTR-Modul-200 and HTR-10.
In addition, several benchmarks were performed in order to evaluate the precision of the Dancoff factor calculation, especially in presence of dummy pebbles, since this calculation is notably difficult. Two of them are reported on later in this section.
Moreover, a simplified HTGR design is used to compare an Once Through Then Out (OTTO) shuffling scheme with Serpent. This reactor was designed to be able to work with the simplest design possible, containing all important features a HTGR has to have in order to represent all of its relevant safety aspects.
Additionally, a benchmark concerning the use of a different kind of fissile material than ^{235}U was carried out. For this case, a mixture of ThO_2 and UO_2 is used in the same TRISO particle.
Finally, for a selected number of cases, a series of benchmarks is presented where the two Dancoff factor methods, the two different TRISHA spectrum code solvers and the old TISPEC spectrum code are compared; bearing in mind that when it is not explicitly mentioned, the 0D diffusion code and the Bende's Dancoff factor method have been used.
The fine and broad neutron energy group structures used are shown in appendix A.2 and A.3.

6.3 Serpent

As previously mentioned, Serpent was chosen as reference code for this thesis work. Serpent is a three-dimensional continuous-energy Monte Carlo reactor physics burn-up calculation code, developed at VTT Technical Research Centre of Finland since 2004 [86].
In contrast to deterministic codes, Monte Carlo codes model the exact geometry and physics since the transport equation is solved without simplifications even in complex geometries. Serpent is successfully used for:

1. Full-core modelling of commercial and research reactors
2. Fuel cycle studies involving detailed assembly-level burnup calculation
3. Validation of deterministic transport code
4. Neutronics-thermofluid dynamics multiphysics calculations

The burn-up capabilities are entirely based on built-in calculation routines, without external couplings. It has two fundamentally different options for solving the Bateman burn-up equation. The first approach is the Transmutation Trajectory Analysis (TTA) based on the analytical solution of linearized depletion chains [87]. The second method is the Chebyshev Rational Approximation Method (CRAM) based on an advanced matrix exponential solution developed for Serpent at VTT [88]. The two methods, during all the benchmarks and verifications, have shown to yield consistent results.

The explicit HTGR geometry model in Serpent reads the coordinates of fuel particles or pebbles from a separate input file, and generates the geometry as it is defined, without any approximations. The model works on several levels (particles inside a pebble and pebbles inside the core) and it has been tested in realistic double-heterogeneous reactor configurations [89].

To simplify the construction of HTGR geometries, Serpent is able to generate random particle distribution files for the explicit geometry model.

Serpent is systematically validated by comparing it to MCNP while running a standard set of assembly calculation problems. Effective multiplication factors and homogenized few-group reaction cross sections are within the statistical accuracy from the reference results, when the same neutron data libraries are used [90].

Systematic validation for criticality safety analyses using experimental configurations and data from the International Handbook of Evaluated Criticality Safety Benchmark Experiments have being successfully carried out. Serpent-generated group constants have also being used for fuel cycle and transient simulator calculations by several nodal diffusion codes such as: ARES, HEXBU-3D, TRAB-3D and HEXTRAN [86] [90].

6.4 Homogeneous infinite reactor

In this first case, a homogeneous infinite reactor is modelled applying reflective boundary conditions to a cubic lattice whose length side is 1 cm and whose temperature is fixed to 900 K. The reactor is burnt with a constant power of 1 W for 10 days with time steps of one day each. The material composition is shown in table 6.1.

A comparison between Serpent and TRISHA is shown in figure 6.5. The plot reveals a very good agreement among the codes, the relative error calculated as shown in eq. 6.1 is lower than 0.5 %.

$$rel.err.\% = \frac{result_{Serpent} - result_{TRISHA}}{result_{Serpent}}. \tag{6.1}$$

Table 6.1: Homogeneous infinite reactor isotopic densities

isotope	$1/barn/cm$
^{238}U	1.11E-4
^{235}U	1.18E-5
C_{12}	5.14E-2
C_{13}	5.74E-4

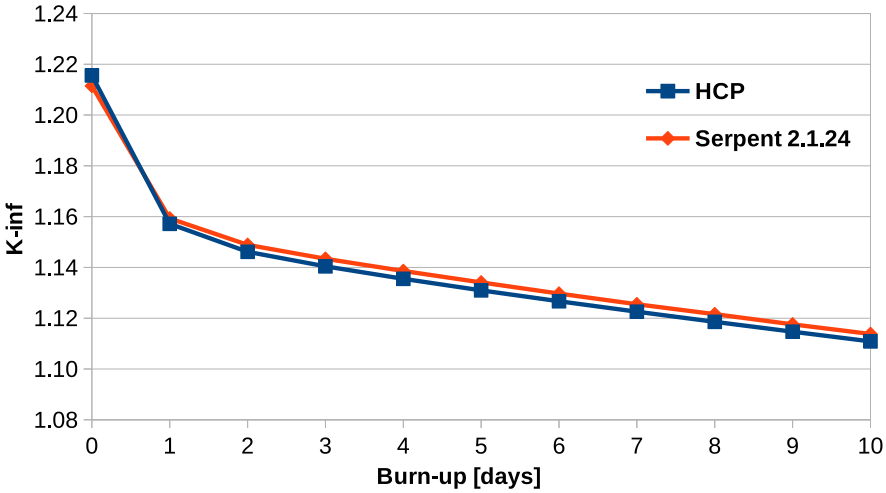

Figure 6.5: Homogeneous infinite reactor k-inf comparison

6.5 Infinite grain models

In order to benchmark the spatial self-shielding effects and part of the Dancoff factor calculation, the obvious step from the homogeneous reactor was to simulate an infinite cubic lattice containing a coated particle, see figure 6.6.

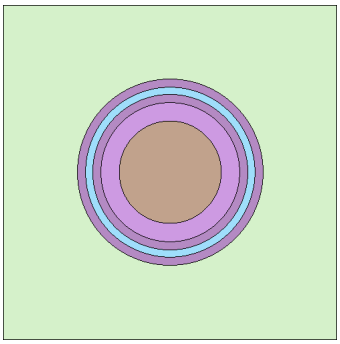

Figure 6.6: Infinite grain cubic lattice

As in the previous case, the coated particles are burnt for 10 days with time steps of one day each, with a power of 1 W, and a fixed temperature of 900 K. The

calculation was repeated considering three different kind of coated particles: PMBR, HTR-10 and HTR-Modul-200. The burn-up curves are shown in the the following figures 6.7, 6.8 and 6.9.

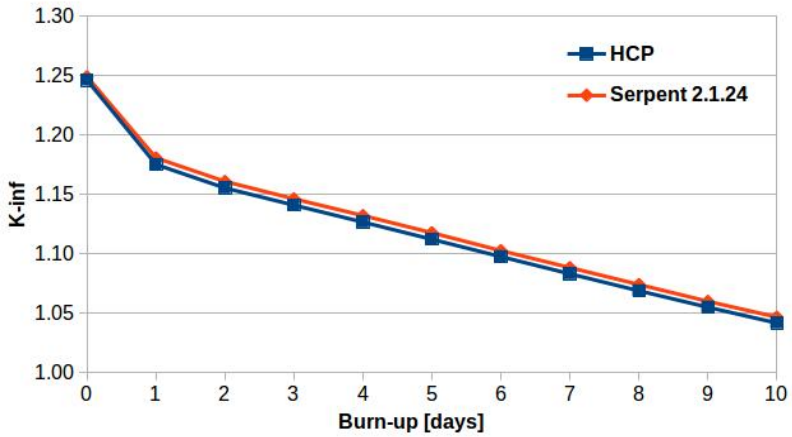

Figure 6.7: PBMR infinite cubic grain lattice k-eff comparison

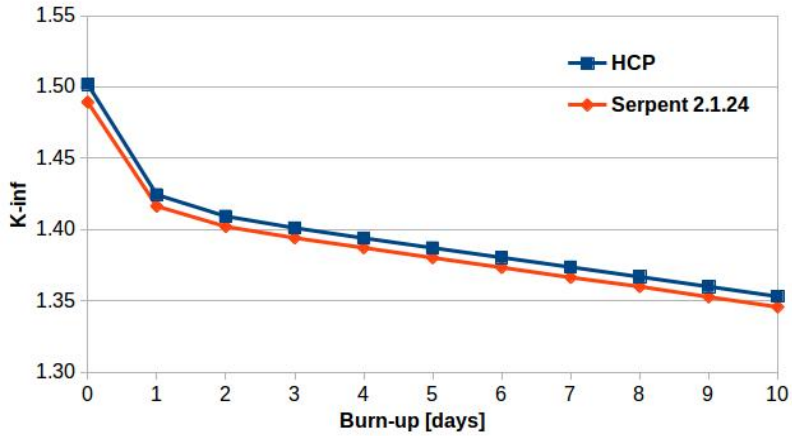

Figure 6.8: HTR-10 infinite cubic grain lattice k-inf comparison

The three graphs show a really good match between the codes. While for the PMBR and HTR-10 cases the errors are about 0.5 %, it is consistently lower for the HTRM-200 one.

From these graphs, it can be seen how usually the error concerning the first HCP criticality calculation is different from all the other ones. This very small change is probably due to the fact the HCP neutron data libraries were condensed using a weighting spectrum calculated taking into consideration fresh fuel pebbles. Therefore, the resonances of the actinides appearing after the first burn-up are not shielded in

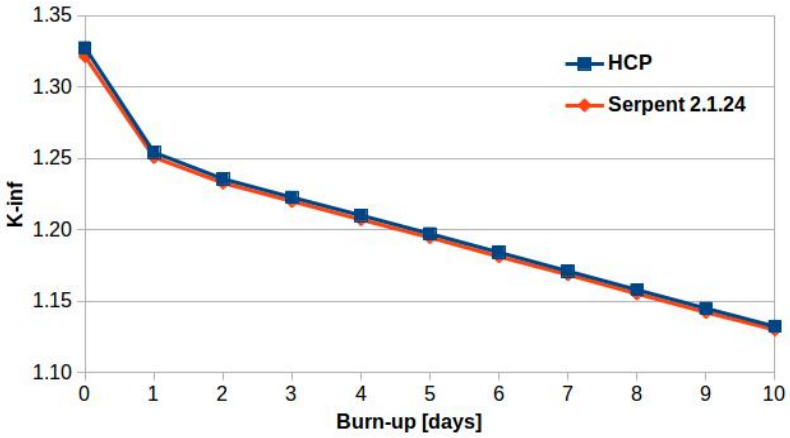

Figure 6.9: HTR-Modul-200 infinite cubic grain lattice k-inf comparison

an optimal way; this, in turn, might be the reason for the change in trend of the error between the first k-eff and all the other ones.

Additionally, the curves perfectly resemble the characteristic shape coming from the xenon dynamics, this is especially visible in the first burn-up time steps.

6.6 Infinite pebble models

Three different kind of fuel pebbles are modelled in TRISHA in these series of benchmarks, in order to test the full Dancoff factor calculation together with the double heterogeneity resonance treatment occurring in the neutron data library generation process. As for the previous benchmarks, the fuel elements are burnt for 10 days with time steps of one day each, a fixed temperature of 900 K but with a power of 10 kW. In these cases, the infinite pebble bed is obtained applying reflective boundary conditions to a cubic lattice, as in figure 6.10.

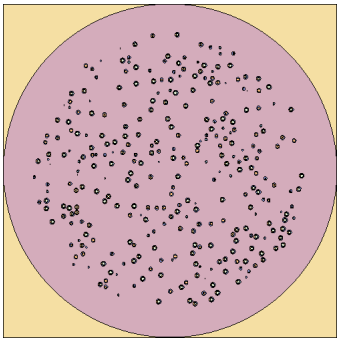

Figure 6.10: infinite cubic pebble lattice

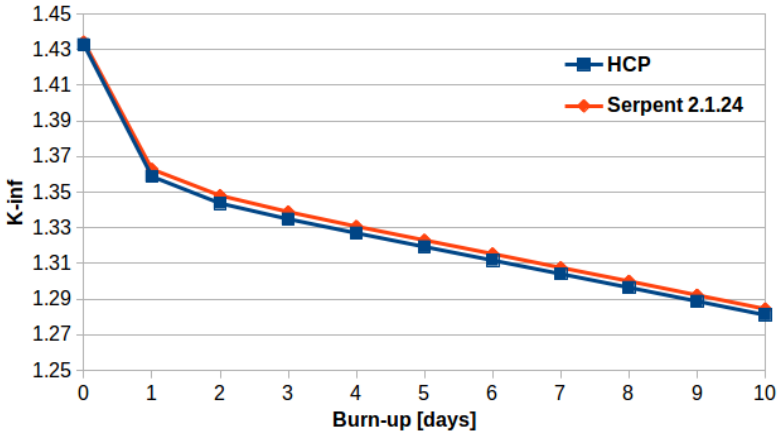

Figure 6.11: PBMR infinite cubic pebble lattice k-inf comparison

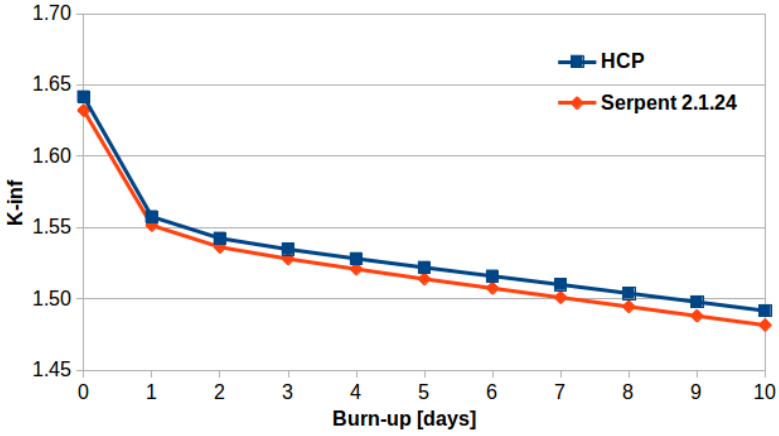

Figure 6.12: HTR-10 infinite cubic pebble lattice k-inf comparison

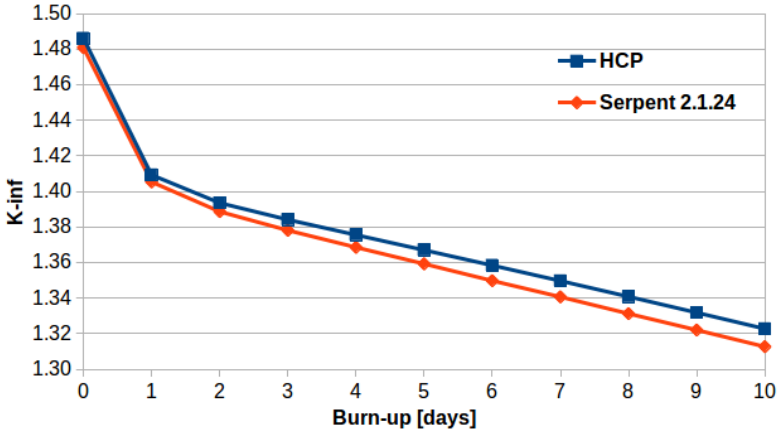

Figure 6.13: HTR-Modul-200 infinite cubic pebble lattice k-inf comparison

The plots shown in 6.11, 6.12 and 6.13 represent k-inf over burn-up comparisons between TRISHA and Serpent. The errors seem to be generally small especially in the case of PMBR pebble where the maximum error during the 10 time steps is lower than 0.30 %.
As in the previous set of benchmarks, also in these cases the first criticality error is somehow different from the other ones; again this is probably due to the assumptions made in the library generation process.

6.7 HTR-10

The HTR-10 is a pebble bed HTGR that makes use of spherical fuel elements with ceramic coated fuel particles. The reactor core has a diameter of 1.8 m, a height of 1.97 m, a core of volume of 5.0 m^3 and it is surrounded by graphite reflectors. The core is filled with 27000 LEU fuel elements whose mean target burn-up is 80,000 MWd/t.

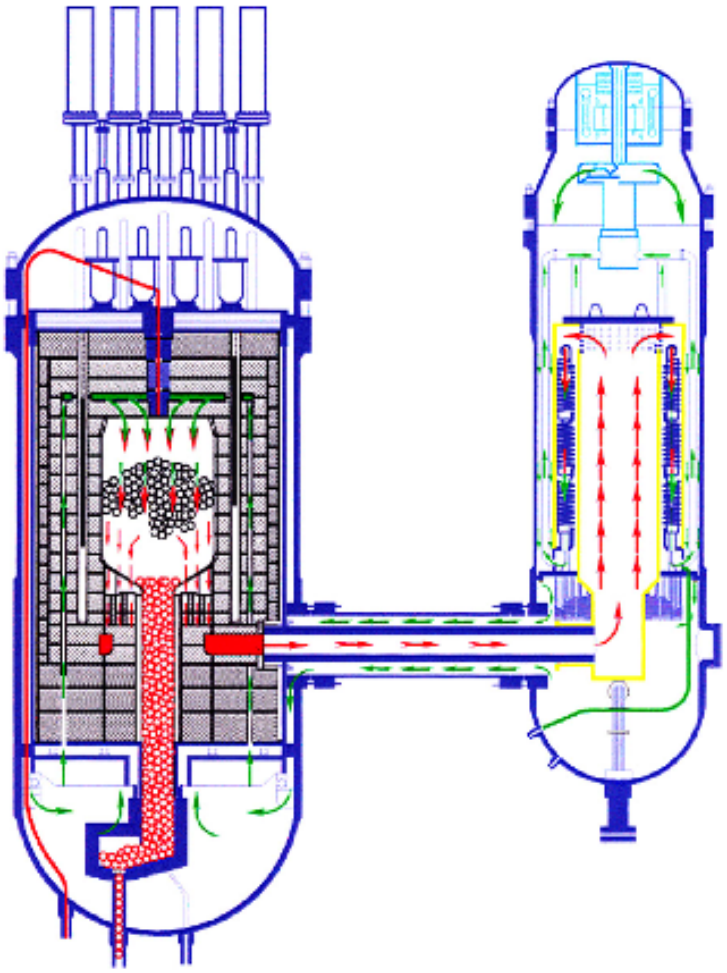

Figure 6.14: HTR-10 nuclear system cross section [91]

As in most HTGR reactors, graphite serves as primary core structural material and the ceramic core structures are housed in a metallic core vessel. Cold helium channels are present within the side reflector for the primary coolant to flow upward after entering the reactor pressure vessel from the annular space between the connecting vessel and the hot gas duct.
Helium flow changes direction at the top of the reactor core to enter the pebble bed, so that a downward flow pattern takes place. After being heated up in the pebble bed, the coolant enters into a hot gas chamber in the bottom reflector and from there it goes through the hot gas duct and then onto the heat exchanger.
The fuel elements pass through the reactor core following a so called MEDUL "multi-pass" pattern. A cross sectional view of the reactor is shown in figure 6.14.
During the initial core loading, dummy balls are firstly positioned at the bottom conus region of the reactor core. Subsequently, a mixture of fuel and dummy pebbles, with a $57 : 43$ ratio, are loaded to approach gradually first criticality [92].
The benchmarks presented afterwards, refer to the criticality experiments conducted at the Institute of Nuclear and New Energy Technology (INET, China). They are based on data made available from the IAEA tecdoc: 'Evaluation of High Temperature Gas Cooled Reactor Performance: Benchmark Analysis Related to the PBMR-400, PBMR, GT-MHR, HTR-10 and the ASTRA Critical Facility' [92].
In order to model the core, it is recommended to include the core structures until the carbon bricks [92]. The 2D reactor calculation model, that was used for this work, is provided in figure 6.15.
The identification zone numbers are shown in figure 6.16. In this case, the control rods holes and the helium flow channels are homogenized with the side reflector materials.

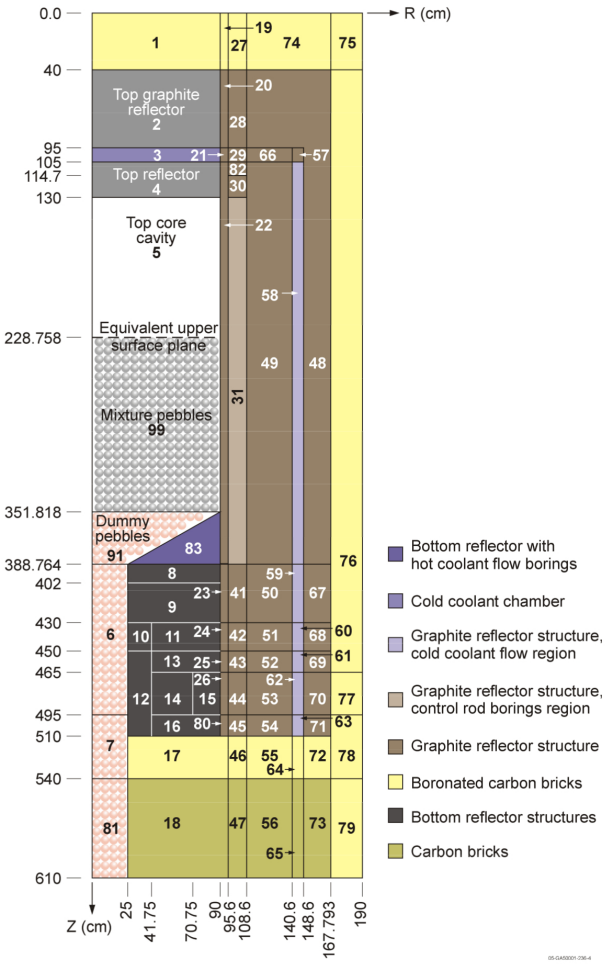

(a) *Vertical cross section.*

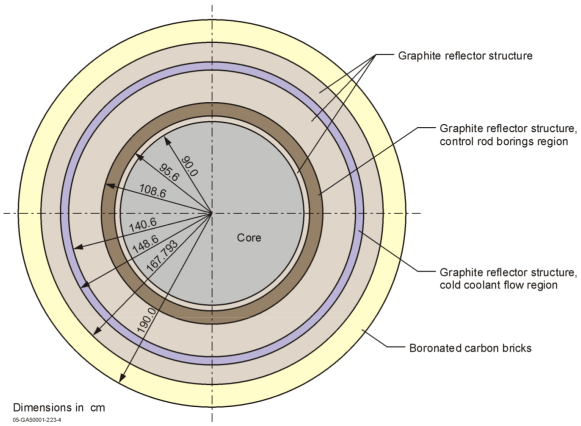

(b) *Horizontal cross section.*

Figure 6.15: HTR-10 2D calculation model [95]

No. of zone	Carbon	Natural boron	Remarks
0	0.851047E-01	0.456926E-06	Bottom reflector with hot helium flow borings
1	0.729410E-01	0.329811E-02	Boronated carbon bricks
2	0.851462E-01	0.457148E-06	Top graphite reflector
3	0.145350E-01	0.780384E-07	Cold helium chamber
4	0.802916E-01	0.431084E-06	Top reflector
5			Top core cavity
6, 7	0.538275E-01	0.288999E-06	Dummy balls, simplified as graphite of lower density
8	0.781408E-01	0.419537E-06	Bottom reflector structures
9	0.823751E-01	0.442271E-06	Bottom reflector structures
10	0.843647E-01	0.298504E-03	Bottom reflector structures
11	0.817101E-01	0.156416E-03	Bottom reflector structures
12	0.850790E-01	0.209092E-03	Bottom reflector structures
13	0.819167E-01	0.358529E-04	Bottom reflector structures
14	0.541118E-01	0.577456E-04	Bottom reflector structures
15	0.332110E-01	0.178309E-06	Bottom reflector structures
16	0.881811E-01	0.358866E-04	Bottom reflector structures
17,55,72,74, 75,76,78, 79	0.765984E-01	0.346349E-02	Boronated carbon bricks
18,56,73	0.797184E-01	0.000000E+00	Carbon bricks
19	0.761157E-01	0.344166E-02	Boronated carbon bricks
20	0.878374E-01	0.471597E-06	Graphite reflector structure
21	0.579696E-01	0.311238E-06	Graphite reflector structure
22,23,25,49, 50,52,54,66, 67,69,71, 80	0.882418E-01	0.473769E-06	Graphite reflector structure
24,51,68	0.879541E-01	0.168369E-03	Graphite reflector structure
26	0.846754E-01	0.454621E-06	Graphite reflector structure
27	0.589319E-01	0.266468E-02	Boronated carbon bricks
28,82	0.678899E-01	1.400000E-05	Graphite reflector structure
29	0.403794E-01	1.400000E-05	Graphite reflector structure
30,41	0.678899E-01	0.364500E-06	Graphite reflector structure
31-40	0.634459E-01	0.340640E-06	Graphite reflector, control rod borings region
42	0.676758E-01	0.125331E-03	Graphite reflector structure
43,45	0.861476E-01	0.462525E-06	Graphite reflector structure
44	0.829066E-01	0.445124E-06	Graphite reflector structure
46	0.747805E-01	0.338129E-02	Boronated carbon bricks
47	0.778265E-01	0.000000E+00	Carbon bricks
48	0.582699E-01	0.312850E-06	Graphite reflector structure
53	0.855860E-01	0.459510E-06	Graphite reflector structure
57	0.728262E-01	0.391003E-06	Graphite reflector structure
58,59,61,63	0.760368E-01	0.408240E-06	Graphite reflector, cold helium flow region
60	0.757889E-01	0.145082E-03	Graphite reflector, cold helium flow region
62	0.737484E-01	0.395954E-06	Graphite reflector, cold helium flow region
64	0.660039E-01	0.298444E-02	Boronated carbon bricks
65	0.686924E-01	0.000000E+00	Carbon bricks
70	0.861500E-01	0.462538E-06	Graphite reflector structure
77	0.749927E-01	0.339088E-02	Boronated carbon bricks
81	0.797184E-01	0.000000E+00	Dummy balls, but artificially taken as carbon bricks

Figure 6.16: HTR-10 2D model material description [92]

6.7.1 First criticality experiment

The first criticality experiment on HTR-10 took place in December 2000 making use of the extrapolation approach. Three neutron counters, positioned in the side reflector, were employed to monitor the process and predict the number of pebbles that would make the reactor critical.

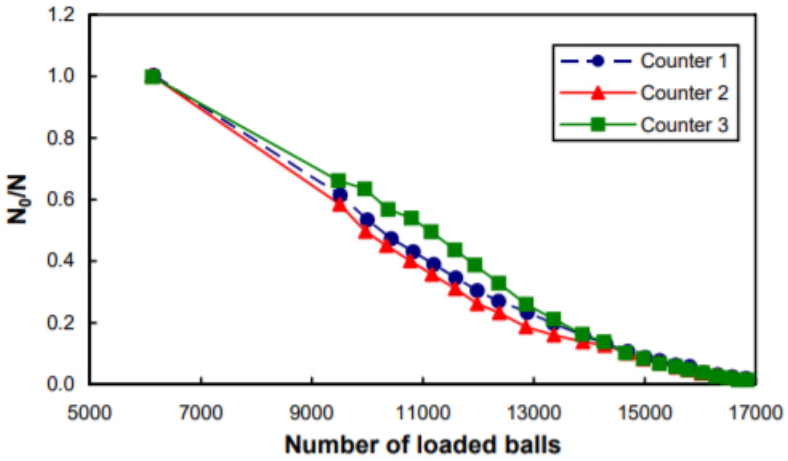

Figure 6.17: HTR-10 first criticality extrapolation curves [93]

An Americium-Berillium start-up neutron source, with an intensity of about 20 Curies ($4.4 \cdot 10^7$ n/s), was placed in the side reflector.
Figure 6.17 shows the extrapolation curves from each of the neutron counters. During the experiment, criticality was reached when a total number of 16890 pebbles were loaded into the reactor core. The corresponding critical height was estimated to be 123.06 cm from the top of the cone area.

6.7.2 First criticality B1 benchmark

The original B1 benchmark deals with the calculation of the critical height of pebbles under a helium atmosphere and a core temperature of 27° C, without the insertion of any control rods. As said before, the experimental critical height measured was 123.06 cm from the top of the conus area. In order to obtain a rigorous comparison among different codes, the critical height is fixed for every code model and the k-effectives are then compared. The results, concerning the comparison between HCP and Serpent, are shown in table 6.2.

Table 6.2: Original B1 experiment k-eff comparison

HCP	Serpent	rel. err. (%)
1.01438	1.01358	-0.079

Following the publication of the first data, the INET institute released a revised version of those data, known as deviated or revised benchmark. With respect to the original B1 benchmark, the changes can be synthesized as follows:

1. The density of the dummy pebbles is increased from 1.73 to 1.86 g/cm^3.
2. The impurities boron equivalent concentration in the dummy pebbles is decreased from 1.3 to 0.125 ppm.
3. The experiment took place under air atmosphere.
4. The recommended temperature for the simulation is 15° C.

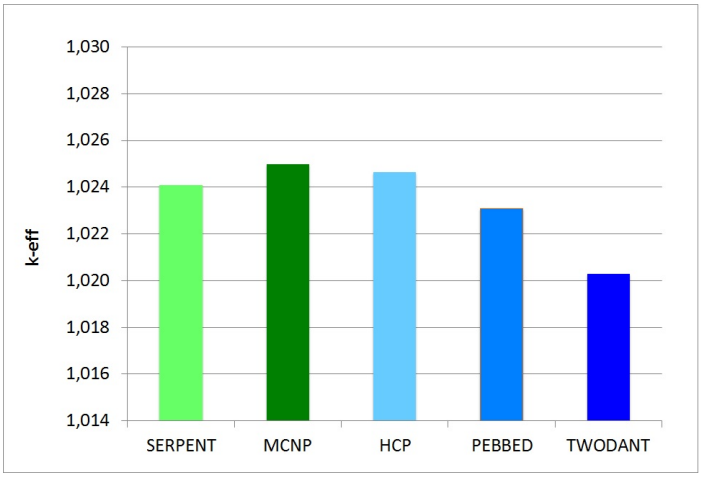

Figure 6.18: Deviated B1 experiment k-eff comparison

The comparison, regarding the deviated benchmark shown in figure 6.18 includes the Monte Carlo code MCNP [30], the INL's neutron diffusion pebble bed reactor physics code PEBBED, the neutron transport discrete ordinates code TWODANT [94], HCP and the Monte Carlo code Serpent. Every of these codes follow the specifications of the 2D model presented above.
While the results coming from the first three codes were obtained at INL and are the topic of a specific publication [95], the Serpent and HCP models were built in parallel, within the scope of this work, in order to verify every step of the construction of this model. In figure 6.19 we can see the cross-sectional views of the Serpent model.
In this case, due to the Serpent limitations in the built-in pebble random distribution generator, it was possible to obtain a random pebble bed with a filling factor of 0.61 only in the upper part of the pebble bed, while for the conus area a hexagonal regular lattice pebble distribution with a filling factor of 0.6046 had to be used. The difference is obvious in figure 6.19 a.

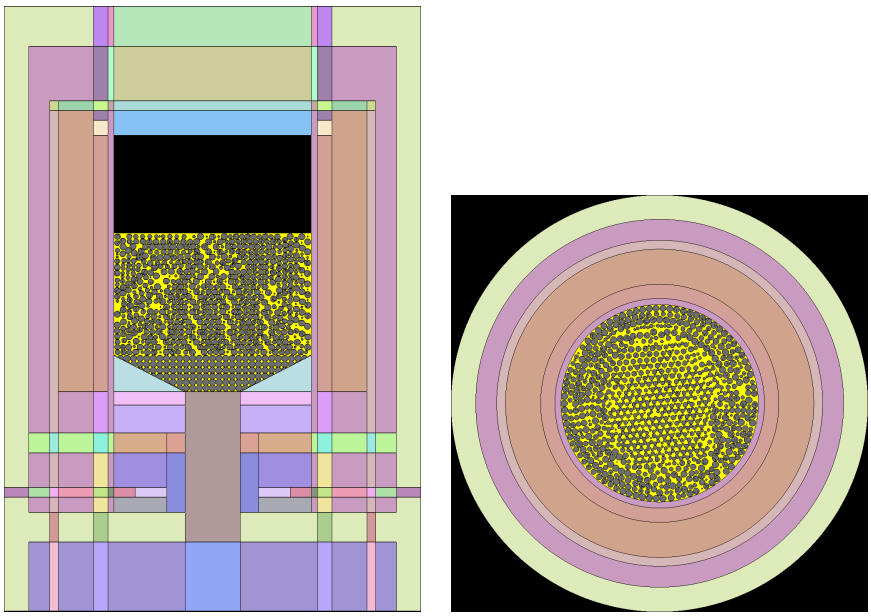

(a) *Vertical cross section.* (b) *Horizontal cross section.*

Figure 6.19: HTR-10 2D Serpent model [95]

From the histogram 6.18, regarding the deviated dataset, it can be observed how the HCP model is in line with the other deterministic codes (in blue). The same thing could be said for our Serpent model whose k-eff lays very close to the MCNP one. The relative error of HCP with respect to Serpent is about -0.05 %. The same order of magnitude can be also found comparing the HCP result to the Serpent one in the original dataset.

This validation benchmark experiment, considering the deviated parameters, is supposed to reproduce the reactor configuration that brought the HTR-10 into its first criticality. Although the comparison with the other codes shows a relatively small spread of k-eff values, they are collectively higher than the experimental k-eff value of 1.0. The analysis that followed this international criticality experiment, that can be found in [92], pointed out as plausible causes of these discrepancies the following issues: uncertainties in the water content of the graphite pores (assumed to be zero), uncertainties in the modelling of the neutron streaming (directional diffusion calculations seem to be required) and choice of the selected cross section library.

It is therefore believed that the discrepancy between the calculated and the experimental k-eff is for a good part attributable to uncertainties coming from the experiment itself.

6.7.3 B2 benchmark

The B2 benchmark is focused on the temperature dependency of k-eff. The same 2D model, as for the B1 benchmark, is used but this time with a pebble bed height of 180.12 cm. The calculation is repeated at three different temperatures: 27° C, 120° C and 250° C. The results are split in two different histograms, the first one concerning the original data and the second one concerning the deviated ones, figure 6.20.

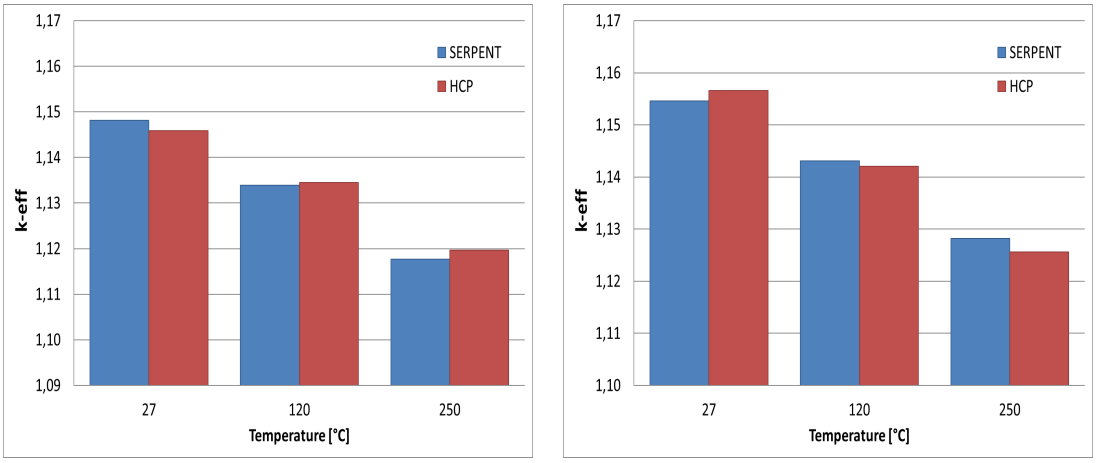

(a) *Original B2 experiment.* (b) *Deviated B2 experiment.*

Figure 6.20: B2 experiments k-eff comparison

The results display a strong agreement at 120°C where the relative error is about 0.06 %, while in the other cases is anyway lower than 0.2 %. A similar trend is repeated for the deviated cases.

6.8 HTR-Modul-200

The HTR-Modul-200 was initially developed as a modular heat source for cogeneration of electricity and steam production. The basic design scheme of such a modular unit, which is combined with a steam generator, is shown in figure 6.21.
The reactor core as well as the steam generator are located in separate steel vessels which are connected through a coaxial pipe. The helium circulator is located inside the steam generator vessel arranged at the top of it. The reactor core consists of 360,000 fuel elements, which contain the fuel UO_2 in form of TRISO coated particles. The core has a diameter of 3 m and a height of 9.43 m. This choice of H/D ratio deviates from the typical LWR reactor design, which use a H/D ratio of nearly 1, because of the optimisation of the neutron balance. The reason is that the decay heat in a loss of coolant accident shall be transported out of the core in a passive

way just by heat conduction, heat radiation and natural convection with limitation of the maximal fuel temperature to values less than 1600 $°C$.

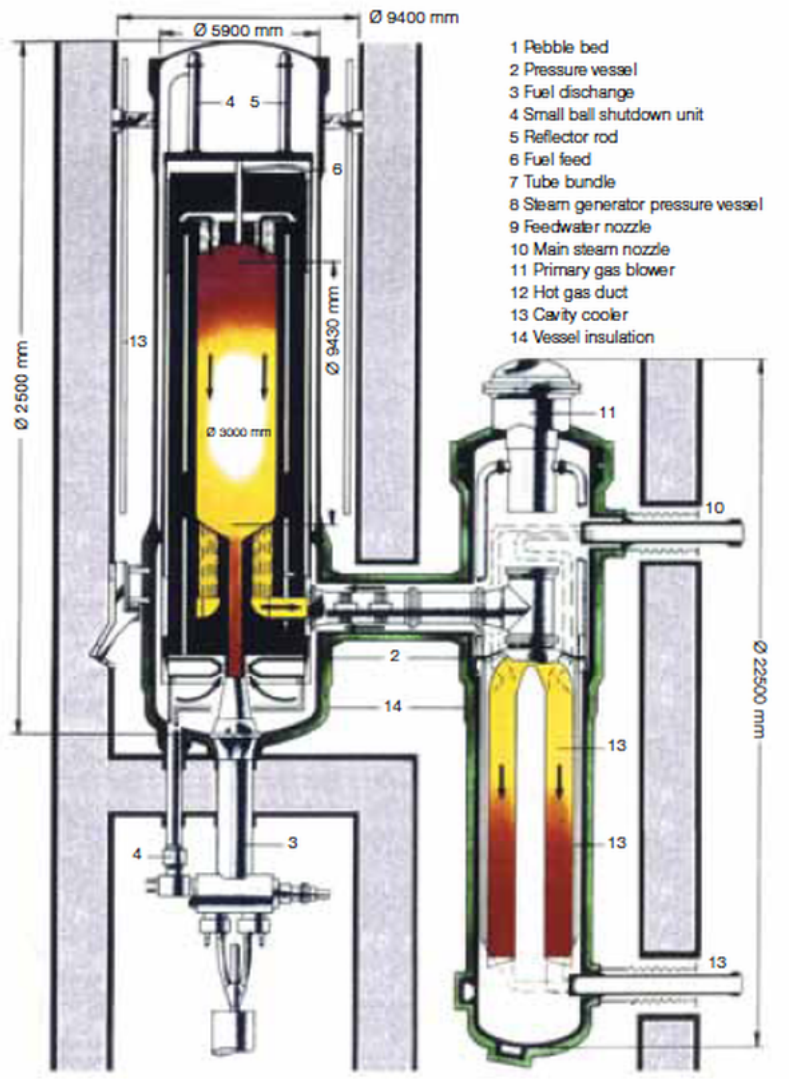

Figure 6.21: HTR-Modul-200 general scheme. Image Credit: AREVA

Since it was required that all shutdown elements are located inside the side reflector, the core diameter is limited to 3 m. The average power density in the core is chosen by these boundary conditions as 3 MW/m^3.
The helium coolant gas flow is from top to bottom and in case of steam generation the gas is heated up from 250 $°C$ to 700 $°C$. The hot gas is sampled in a hot gas chamber below the core and transported from here to the steam generator. This component contains helical type tube bundles. The feedwater enters at the bottom of the component while the steam leaves the component via samplers at the top. All

the walls of the primary circuit are cooled by a flow of cold helium at a temperature of 250 $°C$.
The reactor is filled with 7 g of heavy metal fuel elements containing TRISO particles using low enriched uranium oxide (8.6 %) in the MEDUL cycle. The MEDUL cycle consists of 15 passages of the fuel elements through the core before they get their final burn-up, before they are removed and transported to the intermediate storage. Control and hot shutdown are carried out with six reflector rods which form the first shutdown system. For the long-term cold shutdown 18 reflector borings are filled with small absorber spheres; this is the so-called small sphere absorber system KLAK (Kleine AbsorberKugeln).

6.8.1 Fresh core

For this calculation, a simplified model of the HTR-Modul-200 is used. The core and the cone area are filled only with fuel pebbles, following an hexagonal regular lattice distribution, with a filling factor of 0.6046. This is due to the limitation of Serpent in simulating random pebble distributions in reactors containing a cone area. The reflector is composed of only one material and no borings or control rod holes are taken into consideration. The reactor model, as it was used for the Serpent calculation, is shown in figure 6.22.

Table 6.3: HTR-Modul-200 fresh core k-eff comparison

HCP	Serpent	rel. err. (%)
1.33047	1.32687	-0.27

From table 6.3 is evident how close is the match between the two codes, the relative error is about -0.27 %.

6.8.2 Fresh core with dummy pebbles

The benchmarks presented here were conceived in order to assess the accuracy of the dummy pebbles treatment in the unit cell and the Dancoff factor calculations. In the first case, a reactor with the same geometry and material compositions, as in the previous benchmark, is filled with fuel and dummy pebbles randomly distributed with a ratio 1 : 1. While in the second case, the lower half of the core is filled with dummy pebbles and the upper half one with fuel pebbles. In the latter case, a hexagonal regular lattice distribution has been used. The two cases modelled in Serpent are shown in figure 6.23.
The relative errors shown in table 6.4 indicate a remarkable match between the codes, indeed the errors are lower than 0.086%.

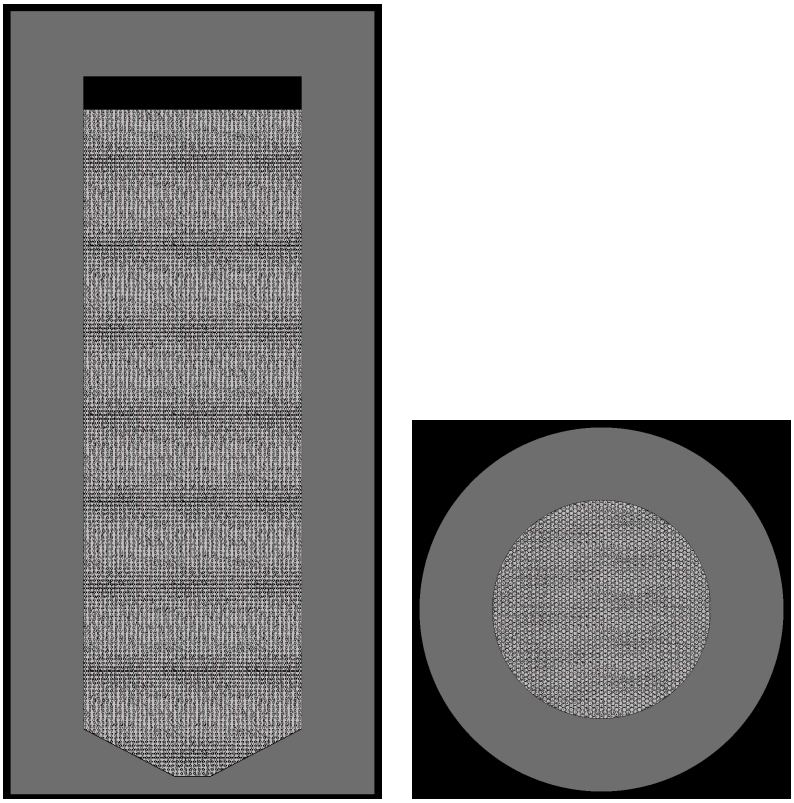

(a) *Vertical cross section.* (b) *Horizontal cross section.*

Figure 6.22: HTR-Modul-200 fresh core, Serpent input model

Table 6.4: HTR-Modul-200 fresh core with dummy pebbles k-eff comparison

case	HCP	Serpent	rel. err. (%)
random	1.32880	1.32774	-0.079
separated	1.29576	1.29688	0.086

6.8.3 Air ingress scenario

In this air ingress scenario, the helium coolant, present in the fresh core benchmark previously showed, is replaced by dry air at 27 $°C$ while everything else stays the same. The k-effective values between HCP and Serpent are compared in table 6.5, where the relative error is just -0.33 %. It is also interesting to see how the $\Delta k = k_{eff}^{hel} - k_{eff}^{air}$, for the two codes are in really good agreement. Indeed, for Serpent we have a value of -0.62 $niles$ while for HCP we have -0.69 $niles$.

6.8.4 Burn-up calculation

A series of ten burn-up time steps of one day each, with a constant power of 200 MW was performed with the simplified HTR-Modul-200. The pebble bed is divided in

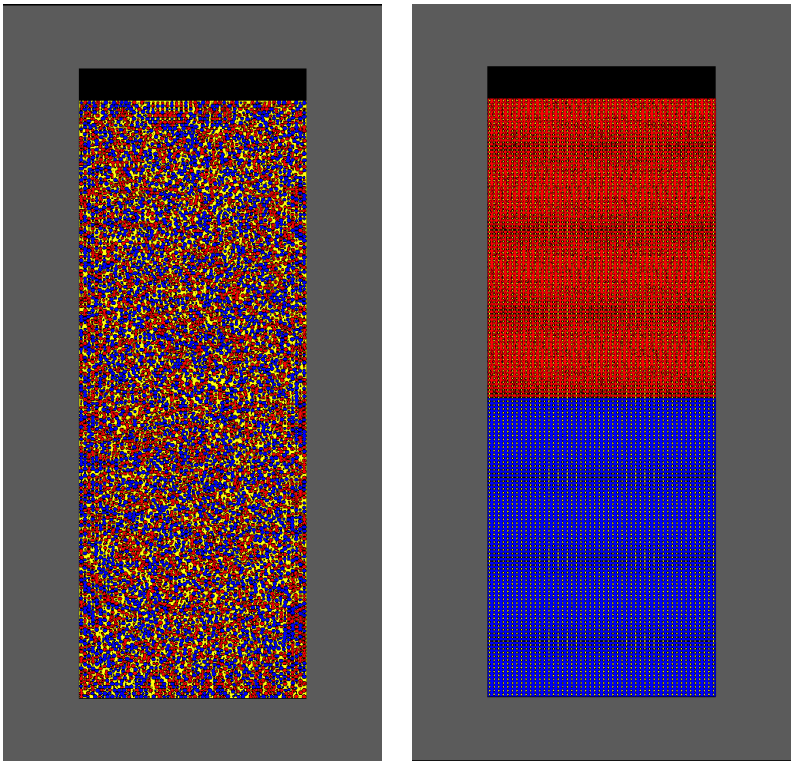

(a) *Random pebble distribution.* (b) *Half core dummy pebbles, half core fuel pebbles.*

Figure 6.23: HTR-Modul-200 fresh core with dummy pebbles, Serpent input model

Table 6.5: HTR-Modul-200 air ingress k-eff comparison

HCP	Serpent	rel. err. (%)
1.32431	1.31997	-0.33

80 burn-up meshes of equal volume, as it can be seen from figure 6.24 where the Serpent model is depicted.
Even the latest version of Serpent does not allow the set up of arbitrary burn-up mesh grids. To overcome this issue, a C++ code was written in order to automatically write Serpent's inputs where the core is divided in several burn-up meshes of equal volume. This script was then used for all the benchmark cases involving burn-up calculations in finite HTGR reactors.
The comparison of results is shown in figure 6.25. The two plots are remarkably close and the maximum relative error is lower than 0.13%.

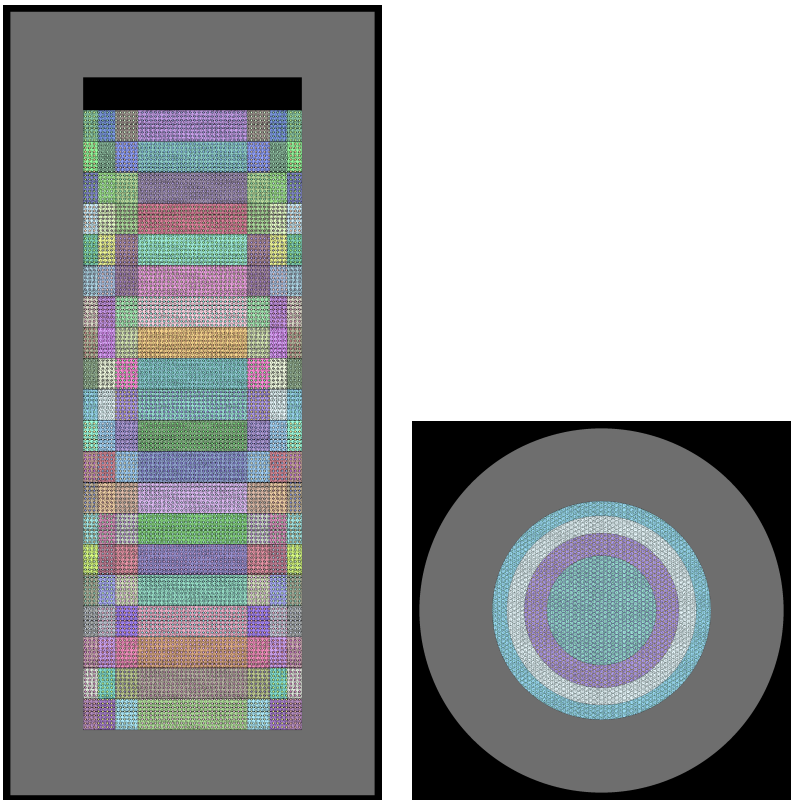

(a) *Vertical cross section.* (b) *Horizontal cross section.*

Figure 6.24: HTR-Modul-200 fresh core with dummy pebble, Serpent input model

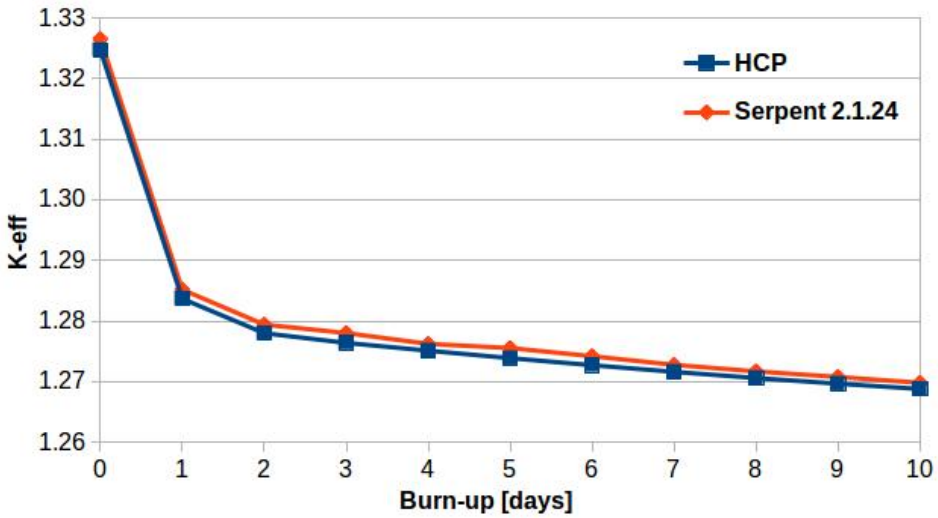

Figure 6.25: HTR-Modul-200 k-eff comparison

6.9 Generic HTR design

The reactor was represented with a 2D model, featuring a core filled with 113,363 pebble fuel elements (9 g of heavy metal content and an enrichment of 8.2 %) containing TRISO coated particles, figure 6.26.
A filling factor of 0.6046 was used to make a comparison with Serpent possible. A graphite reflector surrounds the core, while a void region between the pebble bed surface and the top reflector measures 0.5 m in height. It is a cylindrical core (3 x 3 m) with no cone region and a volume of about 21.2 m^3.
To match a realistic HTGR, a power density of 2.4 MW/m^3 and a total thermal power of 50 MW are fixed. As no fluid dynamics is being performed, the fuel and moderator temperatures are fixed to 900 K [**?**].
This reactor design was conceived as the simplest realistic reactor containing all the important features that are needed for HTGR safety simulations. This design has then been used, along with other ones, in our automated test environment.

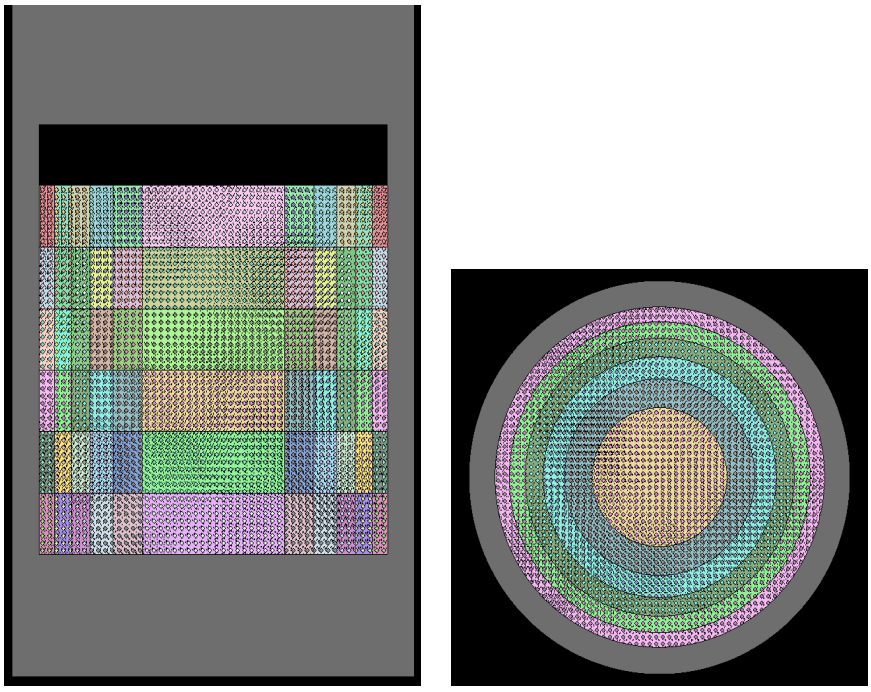

(a) *Vertical cross section.* (b) *Horizontal cross section.*

Figure 6.26: Generic HTR design, Serpent input model

6.9.1 OTTO shuffling

In this benchmark, involving burn-up as well as shuffling calculations, the k-factors calculated from HCP are compared with the ones from Serpent. The calculation is divided in seven steps; at each step, with the exception of the first point, the core is burnt and shuffled following an OTTO shuffling scheme.

Fresh fuel is entering at the top of the core, passing through six axial nodes in six parallel fuel channels until extracted from the core at the bottom.
Each of the 113,097 pebbles have an average power of 442 W. By conducting a parameter study, it was found that each burn up step must be around 90 days to maintain the equilibrium core in a critical state. Due to the radially constant velocity profile the in-core time for all pebbles is 540 days. This leads to an average discharge burn up of approximately 26,520 MWd/t [**?**].
In order to automatize the fuel shuffling in Serpent, another C++ code was written, with the purpose of inserting the new nuclide densities at the end of every burn-up/shuffling time step in the subsequent calculations.

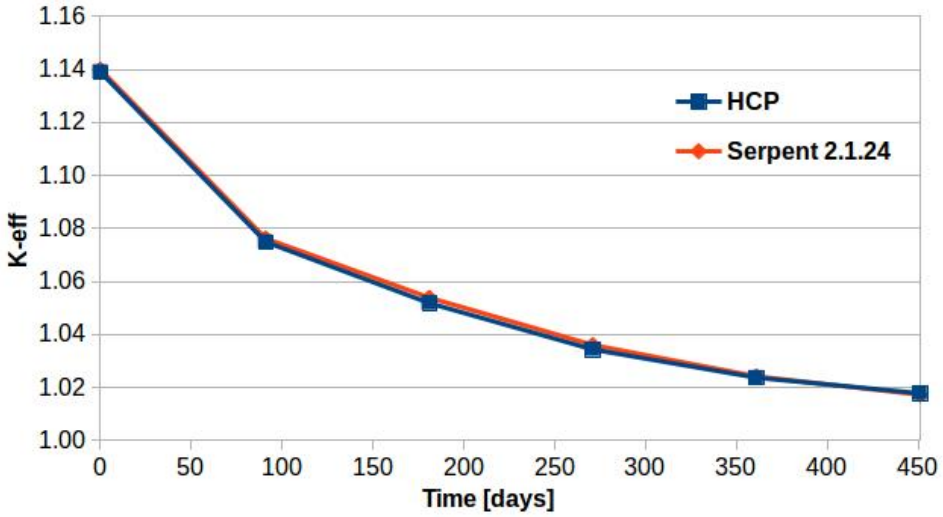

Figure 6.27: Simplified HTR reactor OTTO shuffling scheme comparison

The comparison shown in figure 6.27 suggests a excellent good agreement between the two codes. The maximum relative error is reached at the third time step with a value of 0.197 %.

6.10 Thorium infinite pebble bed benchmark

As previously stated, a different kind of fissile material is modelled in this TRISHA benchmark in order to test, among other parameters, the resonance treatment occurring in the neutron data library generation process for the thorium isotope.
As for the previous infinite pebble bed benchmarks, the fuel elements are burnt for 10 days with time steps of one day each, a homogeneous fixed temperature of 900 K while the power is fixed to a value of 5 kW.
In this case, the infinite pebble bed is obtained applying reflective boundary conditions to a cubic lattice. All the data concerning the fuel geometry and the materials are

shown in appendix A.1.

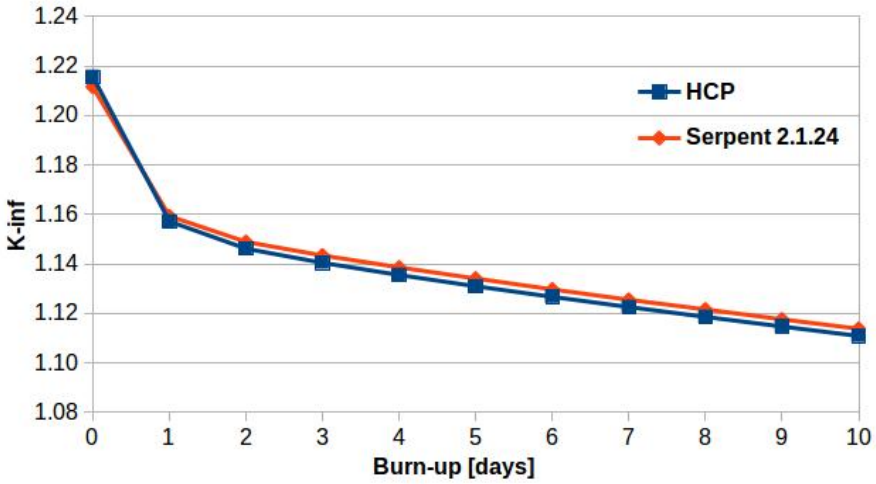

Figure 6.28: Thorium fuel infinite cubic pebble lattice k-inf comparison

The plot shown in 6.28 represents a k-inf over burn-up comparison between HCP and Serpent. The error seems to be generally small, reaching the highest value at the first criticality calculation with a value of 0.30 %.
As in the previous set of benchmarks, also in this case the first k-inf error is somehow different from the other ones. As explained earlier, this is probably due to the fresh fuel weighting spectrum used in NJOY to condense the fine-energy neutron cross sections in the library generation process.

6.11 Additional benchmarks

In this subsection, a series of additional benchmarks concerning different spectrum calculation options are presented.

6.11.1 TRISHA solvers

In order to show the effect of using a different TRISHA solver on a criticality calculation, two cases of the overall set of benchmarks previously presented, were selected as representatives: HTR-10 infinite pebble bed model calculation and HTR-Modul-200 initial criticality. It is important to point out that this is the first attempt to use a neutron transport spectrum code within the MGT-N leakage iteration method.
As it can be seen from table 6.6, the diffusion spectrum code seems to be slightly closer to the Serpent results. This trend has been seen in many other cases. One possible explanation could be the different way the solvers treat the neutron leakage

Table 6.6: Different solvers k-eff comparison

	Diffusion	Transport	Serpent
HTR-10 pebble	1.63762	1.63819	1.63209
rel. err. (%)	-0.339	-0.374	0.0
HTR-Modul-200	1.32703	1.32746	1.32654
rel. err. (%)	-0.037	-0.069	0.0

and the way the leakage data are provided from the full-core code (MGT-N) to the spectrum one. Although the results are not very far from each other, the solvers behave slightly different in presence of negative buckling values coming from the diffusion code calculation. Negative buckling values are often found in core meshes close to the reflector.
This is due to the fast neutrons coming from the core that slowdown into the reflector and come back in the core as thermal neutron in-flux. The neutron transport solver seems to be very sensitive to the "negative leakage" in the thermal range of the energy spectrum. The neutron diffusion code, probably, does not offer the necessary accuracy needed by the transport solver when the leakage becomes negative.

6.11.2 Dancoff factor methods

The same cases, as for the previous benchmark, were selected for this comparison, where the dependency of the Dancoff factor method on the final k-eff is analysed.

Table 6.7: Different Dancoff factor methods k-eff comparison

	Bende	Ji	Serpent
HTR-10 pebble	1.63762	1.64282	1.63209
rel. err. (%)	-0.339	-0.657	0.0
HTR-Modul-200	1.32703	1.33176	1.32654
rel. err. (%)	-0.037	-0.394	0.0

In these cases, it is evident, from table 6.7, how the Ji's method is performing comparatively worse than Bende's approach. It is although possible that performing an ad hoc Monte Carlo calculation, as explained in 3.5.2, Ji's results can be improved.

6.11.3 TRISHA versus TISPEC

The last benchmark, a comparison between TRISHA and TISPEC (the old MGT-3D spectrum code) is presented. The homogeneous infinite reactor benchmark, described in 6.4, is the only one that allow us to perform a full comparison. As it was explained before, one of the most serious limitation of MGT-3D is the fact that it has to

rely on VSOP and MCNP in order to be able to calculate any model that contains heterogeneous fuel.
As a matter of fact, it is customary to model the running-in phase of the reactor in VSOP, until the equilibrium core is reached, then an interface program is tipically used to generate the MGT-3D input from the VSOP output. However, the process is far from being straightforward. Along with the equilibrium core nuclear densities, VSOP provides the mesh-wise thermal disadvantage factors needed for the MGT-3D spectrum calculations.
On the other side, the MGT-3D spectrum code TISPEC is not able to calculate proper background cross sections in order to select the right absorption cross sections from the 2D resonance tables. The problem arises from the fact that TISPEC makes use of a semi-empirical treatment of the double heterogeneity where the homogeneous medium background cross section is modified by a constant parameter, the kappa factor, to make it work for heterogeneous cases too.
In principle, this kappa factor could be calculated by a Monte Carlo code, however a value of 0.4 is always used for ^{238}U regardless of the fuel geometry, the heavy metal content or the coolant. Even using a Monte Carlo code to calculate this parameter would not solve the problem entirely, since the content of the unit cell might change during a running-in phase, where the number of dummy pebbles change in time, or during a water ingress scenario.
As it was said before, this issue does not arise using TRISHA where the unit cell content is updated constantly, and the process is fully automatized.
At this point it is clear how a comparison between the two spectrum codes, for a heterogeneous fuel geometry, would involve the use of TRISHA and HCP on one side and VSOP (which is a modular code), the interface code, a Monte Carlo code and MGT-3D on the other side. Whatever the outcome of the comparison was, it would depend on the physics approximations of the several codes involved in the chain of tools, the different models used in each of them and the libraries involved. This, in turn, would seriously question the validity of the comparison, therefore a homogeneous case was chosen.

Table 6.8: Homogeneous reactor k-inf comparison

	HCP	TISPEC	Serpent
k_{inf}	1.30610	1.30820	1.29940
rel. err. (%)	-0.515	-0.677	0.0

The result of the comparison can be seen in table 6.8, the two codes show to be remarkably close to the Serpent's result although TRISHA performs slightly better.

6.12 Code performance analysis

Finally, in the last part of this section, a series of data concerning time performance and memory requirements are presented and analysed. Four of the previous cases, already described in this section, were selected as representatives for the following comparisons. The four cases include: the 10-step infinite PBMR grain model burn-up calculation, the 10-step infinite HTR-10 infinite pebble bed model burn-up calculation, the 10-step HTR-Modul-200 burn-up calculation and the HTR-10 B1 deviated criticality calculation.
It must be emphasized that these comparisons are meant to only to give a qualitative indication of the time and memory requirements of the calculations performed within this thesis. Indeed, it is not totally fair to compare a Monte Carlo code to a deterministic one, especially when no uncertainty analyses are performed for the determinist code, like in this case. Since the computational time is linked to the statistical error associated to the result of a Monte Carlo code. For the first three cases involved, Serpent statistical error is about 20 pcm while for the last one is about 10 pcm.
Furthermore, it is important to say that all Serpent calculations where performed in parallel using 12 cores while HCP is a serial code. However, both codes used the same machine.

Table 6.9: Memory requirements

	HCP [GB]	Serpent [GB]	Factor
PBMR inf. grain	1.5	28.1	18.7
HTR-10 inf. pebble bed	1.6	63.9	39.9
HTR-Modul-200	3.1	76.2	24.2
HTR-10 B1 deviated case	1.6	3.7	2.3

Additionally, the time performance and memory requirements of Serpent depends on the kind of parallelization and the number of cores used. Two kinds of parallelization are available: OpenMP and an MPI-OpenMP hybrid one [96]. Furthermore, Serpent has a couple of options to decrease the memory requirements at the cost of increasing the computational time, however those were not used for our comparisons.
From tables 6.9 and 6.10, we can certainly draw the following conclusions. As expected, HCP is much faster and requires less memory than the Monte Carlo code Serpent. The difference is very evident in the first three cases where there is a speed-up factor ranging from 60 to 200, while the memory requirement factor ranges from 24 to 40. Although many improvements have been done with respect to burn-up calculations in Monte Carlo codes, the difference between a deterministic code and a

Table 6.10: Speed comparison

	HCP [min]	Serpent [min]	Factor
PBMR inf. grain	2.17	433.73	200.18
HTR-10 inf. pebble bed	2.22	444.18	200.38
HTR-Modul-200	184.12	457.50	2.48
HTR-10 B1 deviated case	2.98	180.05	60.35

Monte Carlo one is remarkable [97]. The speed-up and the memory usage factors are close to two in the case of the HTR-10 criticality calculation.
In addition, it can be seen that while for the Monte Carlo code is more important the number of isotopes and materials involved in the calculation, for HCP the number of meshes involved in a burn-up or diffusion calculation is the key factor with respect to speed and memory performances. This is even more evident considering the cases 1, 2 and 4 where the memory usage is only associated to the size of the HCP neutron data library.

7 Conclusions and outlook

In this thesis, the design, the implementation and the validation of a new spectrum code for high temperature gas reactor was carried out. Two different solvers were implemented, a 0D diffusion code and a 0D transport one, along with two different Dancoff factor calculation methods.
This work was started in order to overcome some of the limitations of the former MGT-3D spectrum code TISPEC. Namely, to make use of a more complete and efficient neutron data library, to have a better treatment of the neutron resonances in connection with the double heterogeneity issue, to avoid spectrum code dependencies and to make use of the latest capabilities of modern program languages like C++.
Within the present work, it was shown how the new spectrum code was implemented inside the HCP framework and how it was linked to the diffusion and the burn-up code modules.
An extensive benchmark campaign was carried out in order to understand and delineate the accuracy of these solvers and at the same time to correct possible technical bugs.
Many different models of increasing complexity were tested in order to assess the accuracy of TRISHA's calculations against a well-established Monte Carlo code such as Serpent.
Furthermore, different kinds of TRISO particles and fuels were tested along with various sets of temperatures in order to guarantee consistency of results with different sets of parameters.
All the benchmarks show a excellent agreement with the Monte Carlo Serpent code. In particular, the HTR-10 criticality benchmarks B1 and B2, show impressive matches considering the level of complexity of such models.
Additionally, a code was written in order to allow Serpent to perform a generic OTTO shuffling scheme on the generic HTR design, attaining an strong agreement.
Achieving a good level of automatization of the neutron spectrum calculations, was also an important goal. The user is not asked to provide any unit cell parameters; it is a task of the code, to calculate the appropriate unit cell values needed for the spectrum calculation, according to the current reactor core conditions.
Considerable time was also spent on the design and implementation of an accurate and user-friendly neutron cross section data library generator, which benchmarking comparisons demonstrated the success and validity of.
Finally, it was proven the accuracy and the correctness of the re-implementation of the neutronic part of MGT-3D, that is MGT-N, within the HCP framework. HCP was able to reproduce, within the prescribed precision, the results of the MGT-3D, with respect to neutronics simulations.
More work will be needed in order to progress towards a multi-dimensional spectrum

transport code, in order to generate control rod neutron cross sections with a greater level of accuracy. Moreover, a parallelization of the spectrum code calculations could be of great benefit for the overall speed performance of HCP.

A Appendix

A.1 Fuel element characteristics

Table A.1: PBMR fuel element characteristics [98]

Fuel pebble	
Diameter of the pebble	6 cm
Diameter of the fuel zone	5 cm
Density of the graphite in matrix and outer shell	1.75 g/cm^3
Heavy metal loading per pebble	9.0 g
Enrichment of ^{235}U (weight)	8.2 %
Equivalent natural boron content of impurities in uranium	25.0 ppm
Equivalent natural boron content of impurities in graphite	0.5 ppm
Volumetric filling fractions of pebble in the core	0.61
Fuel kernel	
Radius of the kernel	0.25 cm
UO_2 density	10.4 g/cm^3
Coatings	
Coatings layer materials (starting from kernel)	C/PyC/SiC/PyC
Coatings layer thickness	0.09/0.04/0.035/0.04 mm
Coatings layer density	1.05/1.9/3.18/1.9 g/cm^3

Table A.2: HTR-10 fuel element characteristics [98]

Fuel pebble	
Diameter of the pebble	6 cm
Diameter of the fuel zone	5 cm
Density of the graphite in matrix and outer shell	1.73 g/cm^3
Heavy metal loading per pebble	5.0 g
Enrichment of ^{235}U (weight)	17 %
Equivalent natural boron content of impurities in uranium	4 ppm
Equivalent natural boron content of impurities in graphite	1.3 ppm
Volumetric filling fractions of pebble in the core	0.61
Fuel kernel	
Radius of the kernel	0.25 cm
UO_2 density	10.4 g/cm^3
Coatings	
Coatings layer materials (starting from kernel)	C/PyC/SiC/PyC
Coatings layer thickness	0.09/0.04/0.035/0.04 mm
Coatings layer density	1.1/1.9/3.18/1.9 g/cm^3
Dummy element (Original data)	
Diameter of the pebble	6 cm
Density of the graphite	1.73 g/cm^3
Equivalent natural boron content of impurities in graphite	1.3 ppm
Dummy element (Deviated data)	
Diameter of the pebble	6 cm
Density of the graphite	1.84 g/cm^3
Equivalent natural boron content of impurities in graphite	0.125 ppm

Table A.3: HTR-Modul-200 fuel element characteristics [99]

Fuel pebble	
Diameter of the pebble	6 cm
Diameter of the fuel zone	5 cm
Density of the graphite in matrix and outer shell	1.75 g/cm^3
Heavy metal loading per pebble	7.0 g
Enrichment of ^{235}U (weight)	8.0 %
Equivalent natural boron content of impurities in uranium	0.0 ppm
Equivalent natural boron content of impurities in graphite	1.3 ppm
Volumetric filling fractions of pebble in the core	0.61
Fuel kernel	
Radius of the kernel	0.25 cm
UO_2 density	10.4 g/cm^3
Coatings	
Coatings layer materials (starting from kernel)	C/PyC/SiC/PyC
Coatings layer thickness	0.095/0.04/0.035/0.04 mm
Coatings layer density	1.05/1.9/3.18/1.9 g/cm^3
Dummy element	
Diameter of the pebble	6 cm
Density of the graphite	1.75 g/cm^3
Equivalent natural boron content of impurities in graphite	1.3 ppm

Table A.4: $(U, Th)O_2$ fuel element characteristics

Fuel pebble	
Diameter of the pebble	6 cm
Diameter of the fuel zone	5 cm
Density of the graphite in matrix and outer shell	1.74 g/cm^3
Thorium loading per pebble	5.0 g
Uranium loading per pebble	5.0 g
Enrichment of ^{235}U (weight)	20.0 %
Equivalent natural boron content of impurities in uranium	0.0 ppm
Equivalent natural boron content of impurities in graphite	1.3 ppm
Volumetric filling fractions of pebble in the core	0.61
Fuel kernel	
Radius of the kernel	0.25 cm
$(U, Th)O_2$ density	10.4 g/cm^3
Coatings	
Coatings layer materials (starting from kernel)	C/PyC/SiC/PyC
Coatings layer thickness	0.095/0.04/0.035/0.04 mm
Coatings layer density	1.05/1.9/3.18/1.9 g/cm^3

A.2 Fine energy neutron group structure

Table A.5: MUPO fine energy neutron group structure [31]

group number	energy $[eV]$
1	2.50000E-03
2	1.00000E-02
3	2.00000E-02
4	3.00000E-02
5	4.00000E-02
6	5.00000E-02
7	6.00000E-02
8	7.50000E-02
9	9.50000E-02
10	1.20000E-01
11	1.50000E-01
12	1.90000E-01
13	2.30000E-01
14	2.70000E-01
15	3.10000E-01
16	3.70000E-01
17	4.50000E-01
18	5.50000E-01
19	6.25000E-01
20	8.25000E-01
21	1.00000E+00
22	1.10000E+00
23	1.30000E+00
24	1.60000E+00
25	1.90000E+00
26	3.05902E+00
27	5.04348E+00
28	8.31529E+00
29	1.76035E+01
30	2.90232E+01
31	6.14421E+01
32	1.30073E+02
33	2.75365E+02
34	7.48518E+02
35	3.35463E+03
36	1.50344E+04
37	6.73795E+04
38	2.35177E+05
39	6.39279E+05
40	1.35335E+06
41	2.23130E+06
42	3.67879E+06
43	6.06531E+06
44	1.00000E+07

A.3 Broad energy neutron group structures

The 6-group neutron broad energy group structure is used for the HTR-10 and the HTR-Modul-200 calculations while the 2-group one is used for all the other cases.

Table A.6: 6-group neutron broad energy group structure

group number	energy $[eV]$
1	2.50000E-03
2	1.20000E-01
3	4.50000E-01
4	3.05902E+00
5	1.30073E+02
6	6.73795E+04
7	1.00000E+07

Table A.7: 2-group neutron broad energy group structure

group number	energy $[eV]$
1	2.50000E-03
2	3.05902E+00
3	1.00000E+07

List of Figures

List of Tables

B References

[1] World Energy Needs and Nuclear Power. World Nuclear Association. 2016.

[2] IEA World energy outlook. 2016.

[3] IEA STATISTICS: Electricity information. 2016.

[4] GIF R&D Outlook for generation IV nuclear energy systems. 2009.

[5] Retrieved from https://www.iaea.org/pris/.

[6] Retrieved from http://www.ngnpalliance.org/.

[7] High Temperature Gas Cooled Reactor Fuels and Materials. IAEA-TECDOC-1645. 2010.

[8] L. Massimo. Physics of high-temperature gas reactors. Pergamon press. 1976.

[9] D. G. Cacuci. Handbook of nuclear engineering. Springer. 2010.

[10] E. Wigner. Theoretical Physics in the Metallurgical Laboratory of Chicago. Journal of Applied Physics. 1946.

[11] Evaluation of high temperature gas cooled reactor performance: Benchmark analysis related to initial testing of the HTTR and HTR-10. IAEA-TECDOC-1382. 2003.

[12] J. D. Bess, N. Fujimoto, J. W. Sterbentz, L. Snoj, A. Zukeran. Evaluation of the Start-Up Core Physics Tests at Japan's High Temperature Engineering Test Reactor (Annular Core Loadings). INL/EXT-09-15794. 2010.

[13] Z. Wu, S. Yu. Zukeran. HTGR Projects in China. INL/EXT-09-15794. Korean nuclear society. 2007.

[14] J. J. Duderstadt, L. J. Hamilton. Nuclear reactor analysis. John Wiley & Sons, 1976.

[15] H. Bohl, E. Gelbard, G. Ryan. MUFT-4, fast neutron spectrum code for the IBM-704. U.S. AEC Report WAPD-TM-72. 1957.

[16] H. Amster, R. Suarez. The calculation of thermal constants averaged over a Wigner-Wilkins flux spectrum: description of the SOFOCATE code. U.S. AEC Report WAPD-TM-39. 1957.

[17] H. Honeck. THERMOS, a thermalization transport code for reactor lattice calculations. U.S. AEC Report BNL-5826. 1961.

[18] F. Barry. LEOPARD - a spectrum dependent non-spatial depletion code for the IBM-7409. U.S. AEC Report WCAP-3741. 1963.

[19] J. Askew, F. Fayers, P Kemshell. A general description of the lattice code WIMS. J Brit Nucl Ener Soc 5:564. 1966.

[20] H.-J. Rütten, K. A. Haas, H. Brockmann, W. Scherer. V.S.O.P.(99/05) Computer Code System. Jül-4189. 2005.

[21] L. Massimo. MAFIA-II, a one-dimensional burn-up code. ANL-7050. 1966.

[22] J. Darvas. DATA-2, Head Programm zum VSOP Zyklus fuer Hochtemperaturreaktoren. KFA Internal Report, KFA-IRE-70-4. 1970.

[23] G. Joanous, J. Dudek. GAM-I: A Consistent P1 Multigroup Code for the Calculation of Fast Neutron Spectra and Multigroup Constants. USAEC Report GA-1850, General Atomic Division. 1961.

[24] G. Joanou. GATHER-II, an IBM-7090 Fortran II Program for the Computation of Thermal Spectra and Associated Multigroup Cross Sections. General Atomic GA-4132. 1963.

[25] G. F. Kuncir. A program for the calculation of resonance integrals. GA-2525. 1961.

[26] T. Fowler, D. Vondy, G. Cunningham. Nuclear Reactor Core Analysis Code CITATION. ORNL-TM-2496 .1971.

[27] K. Petersen, A. Verfondern. THERMIX, ein Computerprogramm zur Berechnung des instationaeren Temperaturverhaltens gasdurchstroemter Kugelschuettungen. To be published.

[28] F. Todt. FEVER - A One-Dimensional Few Group Depletion Program for Reactor Analysis. General Dynamics - General Atomic, GA-2749. 1962.

[29] H.Gerwin, W. Scherer, A. Lauer, G. Strydom. TINTE - A two-dimensional code for reactor dynamics. Jül-4294. 2009.

[30] J. F. Briersmeister. MCNP - A general Monte Carlo N-particle transport code - version 4B. LA-12625. 1997.

[31] J.Schlösser. MUPO An IBM-7090 programme to calculate neutron spectra and multi-group constants. O.E.C.D. High temperature reactor project dragon. 1963.

[32] U. Nyffenegger, J.Schlösser. The new cross section library of the dragon project. O.E.C.D. High temperature reactor project dragon. 1964.

[33] G. Golub, C. Van Loan. Matrix Computations (3rd ed.). 1996.

[34] H. Brockmann. TOTMOS: an integral transport code for calculating spectra and multigroup cross section. Jül-4325, 2002.

[35] M. B. Chadwick et al. ENDF/B-VII.0: Next Generation Evaluated Nuclear Data Library for Nuclear Science and Technology. UCRL-JRNL-225066. 1999.

[36] K. Nönighoff, J. Li, C. Druska, H.-J. Allelein. STATUS OF UPDATING THE CROSS SECTION LIBRARY OF THE JUELICH REACTOR DYNAMIC CODES TINTE/MGT TO ENDF-B-VII. PHYSOR 2010. 2010.

[37] E. E. Lewis, W. F. Miller. Computational methods of neutron transport. John Wiley & Sons, 1984.

[38] K. M. Case, P. F. Zweifel. Linear transport theory. Addison-Wesley publishing company, 1967.

[39] R. J. J. Stamm'ler, M. J. Abbate. Methods of steady-state reactor physics in nuclear design. Accademic press inc. 1983.

[40] D. Selengut. Critical mass calculations for bare hydrogen moderated reactors by means of transport theory. APEX-121. 1952.

[41] W. Y. Yoon, R. A. Grimesey, D. W. Nigg, R. L. Curtis, H. D. Gougar. COMBINE7.1-A portable ENDF/B-VII.0 based neutron spectrum and cross section generation program. Report INL/EXT-08-14729, 2011.

[42] B. Montagnini. Lezioni sul trasporto dei neutroni. 1999.

[43] A.J. Koning, et al. The JEFF evaluated nuclear data project. Proceedings of the International Conference on Nuclear Data for Science and Technology. 2007.

[44] J. R. Lamarsh. Introduction to nuclear reactor physics. Addison-Wesley Pub. Co., Inc. 1966.

[45] P. Wälti, P. Koch. MICROX-a two-region spectrum code for the efficient calculation of group-cross section. Gulf-GA-A10827. 1972.

[46] P. A. M. Dirac. Approximate rate of neutron multiplication for a solid of arbitrary shape and uniform density. Declassified British Report MS-D-5, Part 1. 1943.

[47] G. I. Bell, S. Glasstone. Nuclear reactor theory. Van Nostrand reinhold company, Part 1. 1970.

[48] E. E. Bende, A. H. Hogenbrik, J. L. Kloostermann, H. van Dam. Analytical calculation of average dancoff factor for a fuel kernel in a pebble bed high temperature reactor. Nuclear science and engineering. 1999.

[49] S. M. Dancoff, M. Ginsburg. Surface resonance absorption in closely-packed lattice. USAEC-report CP-2157. 1944.

[50] R. K. Lane, L. W. Nordheim, J. B. Sampson. Resonance absorption in materials with grain structure. Nuclear science and engineering. 1962.

[51] R. M. Westfall. Cosine current transmission probabilities for spherical shells. Transactions of the american nuclear society. 1974.

[52] A. J. Janssen. Enkele opmerkingen over de Dancoff-factor. FYS-LWR-89-11. 1990.

[53] J. L. Kloostermann, A. M. Ougouag. Computation of Dancoff factors for fuel elements incorporating randomly packed TRISO particles. INEEL/EXT-05-02593. 2005.

[54] A. Talamo. Analytical Calculation of the Average Dancoff Factor for Prismatic High-Temperature Reactors. Nuclear Science and Engineering. 2007.

[55] J. L. Kloostermann, A. M. Ougouag. Comparison and Extension of Dancoff Factors for Pebble-Bed Reactors. Nuclear Science and Engineering. 2007.

[56] K. M. Case, F. De Hoffmann, G. Placzek. Introduction to the theory of neutron diffusion.Los Alamos scientific laboratory. 1953.

[57] W. Ji, W. R. Martin. Application of the chord method to obtain analytical expressions for Dancoff factor in stochastic media. Nuclear science and engineering. 2011.

[58] W. Ji, W. R. Martin. Monte Carlo simulation of VHTR particle fuel with chord length sampling. Proc. Joint int. top. mgt. on mathematics & computational and supercomputing in nuclear applications. 2007.

[59] W. M. Stacey. Nuclear reactor physics. wiley-vch. 2007.

[60] H.-J. Allelein, S. Kasselmann, A. Xhonneux, S.-C. Herber. Progress on the development of a fully integrated HTR code package. Nuclear engineering and design. 2012.

[61] S. Kasselmann, A. Xhonneux, F. Tantillo, A. Trabadela, D. Lambertz, H.-J. Allelein. Verification of the HTR code package (HCP) as a comprehensive HTR steady state and transient safety analysis framework. Nuclear engineering and design. 2018.

[62] S. Kasselmann, O. Schitthelm, F. Tantillo, S. Scholthaus, C. Rössel, H.-J. Allelein. Development of a new nuclide generation and depletion code using a topological solver based on graph theory. Nuclear Engineering and Design. 2016.

[63] A. Xhonneux, S. Kasselmann, H.-J. Rütten, K. Becker, H.-J. Allelein. Progress on the development of a new fuel management code to simulate the movement of pebble and block type fuel elements

in a very high temperature reactor core. Nuclear engineering and design. 2014.

[64] A. Xhonneux, H.-J. Allelein. Development of an integrated fission product release and transport code for spatially resolved full-core calculations of V/HTRs. Nuclear Engineering and Design. 2014.

[65] H. Krohn, R. Finken. FRESCO-II - Ein Rechenprogramm zur Berechnung der Spaltproduktfreisetzung aus kugelförmigen HTR-Brennelementen in Bestrahlung und Ausheizexperimenten. Forschungszentrum Jülich internal report. 1983.

[66] K. Verfondern, H. Nabielek. PANAMA - Ein Rechenprogramm zur Vorhersage des Partikelbruchanteils von TRISO Partikeln unter Störfallbedingungen. Forschungszentrum Jülich, internal report. 1985.

[67] J. M. Calo, M. T. Perkins. A heterogeneous surface model for the steady-state kinetics of the boudouard reaction. Carbon, 1987.

[68] H. Gerwin, W. Scherer. Zur validierung der reactordynamik-programmasystems TINTE: graphit-korrosion mit luft, vergleichreschnungen zum experiment VELUNA KFA research center Juelich. Internal report KFA-ISR-1B -8/92. 1992.

[69] H. Gerwin, W. Scherer. Voruntersuchungen zum experiment NACOK mit dem reaktordynamik-programm TINTE KFA research center Juelich. Internal report KFA-ISR-1B -14/93. 1993.

[70] F. Montalbano, M. Ciofalo, A. Trabadela. The graphite-CO_2 reaction in high temperature gas reactors. Tesi di laurea magistrale, Universita' degli studi di Palermo. 2015.

[71] Berechnung der nachzerfallsleistung der kernbrennstoffe von hochtemperaturereaktoren mit kugelförmigen brennelementen, Beiblatt 1 zu DIN 25485 dokumentation und erläuterungen. 1990.

[72] Y. Naito, M. Maeakawa, K. Shibuya. A leakage iterative method for solving the three-dimentional neutron diffusion equation. Nuclear Science and Engineering. 1975.

[73] A. Xhonneux, D. Lambertz, H.-J. Allelein. The enhanced fuel management models of the HTR Code Package (HCP) module SHUFLE. Nuclear Science and Engineering. under review.

[74] S. Jühe. Kohlenstoffstaubfreisetzung bei Druckentlastungsereignissen von Hochtemperaturreaktoren, Ph.D. thesis, RWTH Aachen. 2012.

[75] R. E. MacFarlane, A. C. Kahler. Methods for Processing ENDF/B-VII with NJOY. Los Alamos National Laboratory unclassified report LA-UR-10-04652. 2010.

[76] The NJOY nuclear data processing version 2012 System. LA-UR-12-27079. 2012.

[77] I. I. Bondarenko. Group Constants for Nuclear Reactor Calculations. Consultants Bureau, New York. 1964.

[78] A. Trabadela. High Temperature Reactor Code Package Thermo-Fluid Dynamics Development. RWTH Aachen University PhD Thesis. To be published.

[79] S. Kasselmann. Coding Guidelines for the HTR Code Package, Part I: C++. 2013.

[80] S. Kasselmann. Coding Guidelines for the HTR Code Package, Part II: Fortran. 2013.

[81] W. Scherer, H. Gerwin, R. D. Neef. Theoretische analyse der kritischen HTR-experimentes KAHTER. Jül-1136-RG. 1974.

[82] F. Tantillo, S. Kasselmann, D. Lambert. TRISHA - TRansport Integral Spectrum and Homogenization Application Developers Guide. 2017.

[83] D. J. Beherens. The effect of holes in a reacting material on the passage of neutrons. Proceedings of the Physical Society. 1949.

[84] J. Lieberoth, A. Stojadinovic. Neutron streaming in pebble beds. Nuclear science and engineering. 1980.

[85] J. Leppänen. A new assembly-level Monte Carlo neutron transport code for reactor physics calculations. In proc. M&C. 2005.

[86] Retrieved from http://montecarlo.vtt.fi/.

[87] J. Cetnar. General solution of Bateman equations for nuclear transmutations. Ann. Nucl. Energy. 2006.

[88] M. Pusa, J. Leppänen. Computing the matrix exponential in burnup calculations. 2006. Nuclear science and engineering. 2010.

[89] H. Suikkanen, V. Rintala, R. Kyrki-Rajamäki. An approach for detailed reactor physics modelling of randomly packed pebble beds. In proc. HTR 2010. 2010.

[90] J. Leppänen, J. Mattila, M. Pusa. Validation of the Serpent-ARES code sequence using the MIT BEAVRS benchmark - Initial core at HZP conditions. Ann. Nucl. Energy. 2014.

[91] Retrieved from https://atomicinsights.com/pbmr-project-winding-down-entering-intellectual-property-protection-mode/.

[92] Evaluation of High Temperature Gas Cooled Reactor Performance: Benchmark Analysis Related to the PBMR-400, PBMR, GT-MHR, HTR-10 and the ASTRA Critical Facility. IAEA-TECDOC-1694. 2013.

[93] EVALUATION OF THE INITIAL CRITICAL CONFIGURATION OF THE HTR-10 PEBBLE-BED REACTOR. Idaho National Laboratory. NEA/NSC/-DOC(2006)1. 2006.

[94] R. E. Alcouffe, F. W. Brinkley, D. R. Marr, R. D. O'Dell. A code package for two-dimensional diffusion accelerated neutral-particle transport. Los Alamos National Laboratory report LA-10049-M. 1984.

[95] W. K. Terry, S. S. Kim, L. M. Montierth, J. J. Cogliati, A. M. Ougouag. Evaluation of the HTR-10 reactor as a benchmark for physics code QA. PHISOR-2006. 2006.

[96] J. Leppänen. Serpent - a Continuous-energy Monte Carlo Reactor Physics Burnup Calculation Code. 2015.

[97] W. Haeck, B. Verboomen. An Optimum Approach to Monte Carlo Burn-up. Nuclear Science and Engineering. 2007.

[98] Evaluation of High Temperature Gas Cooled Reactor Performance Benchmark Analysis Related to the PBMR-400, PBMM, GT-MHR, HTR-10 and the ASTRA Critical Facility. IAEA-TECDOC-1694. 2013.

[99] H. Reutler, G. H. Lohnert. The Modular High Temperature Reactor. Nuclear Technology. 1983.